

**Study on the jet energy scale uncertainty in the all-hadronic top  
quark decay channel at the ATLAS experiment**

**Studie der Jet-Energie-Skalen-Unsicherheit im vollhadronischen  
top-Quark Zerfallskanal am ATLAS Experiment**



Masterarbeit an der Fakultät für Physik  
der  
Ludwig-Maximilians-Universität München

vorgelegt von  
Michael Bender  
geboren am 28.01.1986 in Rosenheim

München, den 30.08.2013

Gutachter: Prof. Dr. Otmar Biebel

## Abstract

At the ATLAS experiment, the top quark mass in the all-hadronic decay channel has been measured to be  $174.9 \pm 2.1(\text{stat.}) \pm 3.8(\text{syst.})$  GeV. The systematic uncertainties in this measurement is dominated by the light and  $b$ -jet energy scale with a contribution of 2.1 GeV and 1.4 GeV, respectively<sup>[1]</sup>.

This thesis presents an approach to reduce the impact of these uncertainties. In particular, the main focus of the analysis, which is solely based on MC simulations, is to decrease the influence of the  $b$ -jet energy scale. For that purpose two different top mass estimators are investigated. To determine the  $b$ -jet scale factor an additional observable is introduced. The top quark is reconstructed with a kinematic likelihood fit, while a template method is used to determine  $m_{\text{top}}$  as well as bJSF. With this approach the uncertainty on  $m_{\text{top}}$ , due to the  $b$ -jet energy scale, could be reduced to 80 MeV.

„Das Klare und Offenbare erklärt  
sich selbst, Geheimnis aber wirkt  
schöpferisch.“

*Stefan Zweig*

Maria Stuart, 1. Kapitel

# Contents

<b>1. Introduction</b>	<b>1</b>
<b>2. Theory</b>	<b>2</b>
2.1. The Standard Model of Particle Physics . . . . .	2
2.1.1. Gauge invariance and renormalisation . . . . .	3
2.1.2. Quantum chromodynamics . . . . .	6
2.1.3. The electroweak theory . . . . .	8
2.2. The top-quark . . . . .	10
2.2.1. CKM matrix . . . . .	10
2.2.2. Top-quark production . . . . .	11
2.2.3. Top-quark decay . . . . .	14
<b>3. Experimental setup</b>	<b>17</b>
3.1. The Large Hadron Collider . . . . .	17
3.2. The ATLAS experiment . . . . .	18
3.2.1. The ATLAS coordinate system . . . . .	19
3.2.2. The magnet system . . . . .	19
3.2.3. The inner detector . . . . .	20
3.2.4. The calorimeter . . . . .	21
3.2.5. The muon spectrometer . . . . .	23
3.2.6. The trigger and data acquisition system . . . . .	23
3.3. Top-quark physics at the Large Hadron Collider . . . . .	24
<b>4. Analysis</b>	<b>26</b>
4.1. Monte Carlo datasets . . . . .	27
4.2. Physics object definitions . . . . .	28
4.2.1. Electrons . . . . .	28
4.2.2. Muons . . . . .	29
4.2.3. Jets . . . . .	30
4.2.4. Missing transverse energy . . . . .	34
4.3. Event selection . . . . .	34
4.4. Event reconstruction . . . . .	36
4.5. The top-quark mass . . . . .	38
4.6. The $R_{23}$ and $R_{32}$ estimators . . . . .	40
4.7. The $R_{bl}$ estimator . . . . .	42
4.8. Parametrisation of $R_{23}$ and $R_{bl}$ . . . . .	43
4.9. The template method . . . . .	45
4.9.1. Construction of templates . . . . .	45
4.9.2. Check method for bias . . . . .	47
<b>5. Conclusion</b>	<b>53</b>

<b>A. The <math>R_{32}</math> estimator</b>	<b>54</b>
A.1. Parametrisation . . . . .	55
A.2. Templates for $R_{32}$ . . . . .	55
<b>B. Mathematical functions</b>	<b>58</b>
B.1. Landau . . . . .	58
B.2. Breit-Wigner . . . . .	58
B.3. Novosibirsk . . . . .	59
B.4. Gauss . . . . .	60
<b>C. Template method: parameter values and plots</b>	<b>61</b>
C.1. Plots for varied $m_{\text{top}}$ and constant bJSF values . . . . .	63
C.2. Plots for varied bJSF and constant $m_{\text{top}}$ values . . . . .	67
<b>D. Momenta of light and b-tagged jets</b>	<b>73</b>

# 1. Introduction

One great success of modern physics is the Standard Model of Particle Physics. This theory is capable of describing the fundamental particles and their interactions. In contrast to other theories like e.g. General Relativity, the Standard Model has not been devised by a single mind, but is the result of a joint effort of physicists all over the world. In present-day, the cooperation of numerous scientists is more important than ever, due to the sheer size of modern particle physics experiments.

After being formulated in the 60's and 70's to a consistent theory, the Standard Model has predicted various hitherto unknown features of nature. A recent example is the discovery of the Higgs boson by the ATLAS and CMS experiments in 2012.<sup>[2;3]</sup> Also in case of the top-quark it took years of extensive search till its existence finally had been revealed. After the discovery of the  $\tau$ -lepton at SLAC in 1975<sup>[4]</sup> and the identification of the  $b$ -quark two years later at Fermilab<sup>[5]</sup>, it was obvious that there is a third fermion generation in nature. Therefore, the Standard Model predicted the existence of a sixth quark, serving as the weak isospin partner of the  $b$ -quark. Only in 1995, the top-quark had finally been discovered with the Tevatron experiments CDF and D0.<sup>[6;7]</sup> Since then its properties have been investigated intensively. Besides many physics reasons, the top-quark mass is worth studying for its own sake. Since Yukawa couplings of fermions to the Higgs field are free parameters in the Standard Model, the mass of the top-quark can not be obtained from theory. The most precise measurements yield a value of  $m_{\text{top}} = 173.07 \pm 0.52 \pm 0.72 \text{ GeV}$ .<sup>[8]</sup> Since the uncertainty on  $m_{\text{top}}$  has reached an accurateness of about 1 GeV, more and more elaborated techniques have to be applied to further increase the precision of top-quark mass measurements.

One particular approach for such a measurement in the all-hadronic decay channel is presented in this thesis. The text is divided into three main parts. The first introduces the theoretical background, the second describes the ATLAS experiment, while the third is dedicated to the actual analysis.

## 2. Theory

In this chapter the Standard Model of Particle Physics is briefly described, while in the second part the field of top-quark physics is summarised.

### 2.1. The Standard Model of Particle Physics

The Standard Model of Particle Physics, mainly developed in the 1960s and 1970s, is extremely successful in describing the fundamental particles and their interactions. Except for the drawback, that the Standard Model doesn't account for the force of gravity, it has up to now met every experimental test to highest precision, all of its predictions are experimentally verified. Even the last missing piece, the Higgs Boson, was discovered in 2012, nearly half a century after its postulation.

All known particles can be subdivided into two groups. Particles with half-integral spin, named fermions, and particles with integer spin, the so called bosons. In the framework of the Standard Model matter consists of fermions where the fundamental forces are mediated by bosons.

One remarkable feature of the fundamental fermions is, that they can be grouped into three generations, each containing a so called up and down-type quark, one lepton and one corresponding lepton-neutrino. The interactions covered by the Standard Model, are the electromagnetic force, the origin of electricity and magnetism, the weak force, responsible for nuclear  $\beta$ -decay, and the strong force, accountable for the binding of protons and neutrons in the nucleus. All of these forces are mediated by so called gauge bosons. The particles of the Standard Model are listed in table 2.1.

The Standard Model is described within the framework of Quantum Field Theory. As known from classical mechanics, the dynamics of a system can be described in terms of a Lagrangian function  $L$  by solving the Euler-Lagrange equation.

In Quantum Field Theory however, particles can no longer be described by discrete coordinates and velocities. They have to be replaced by continuous probability densities, represented by fields  $\Phi(\mathbf{x}, t)$ . To account for that, the Lagrangian function is replaced by a Lagrangian density  $\mathcal{L}$ , which is now a function of fields  $\Phi$ , their derivatives  $\partial_\mu \Phi$  and space-time coordinates  $x^\mu$ , with

$$L = \int \mathcal{L}(\Phi, \partial_\mu \Phi, x^\mu) \cdot d^3x \quad (2.1)$$

Hence the Euler-Lagrange equation becomes

$$\partial_\mu \left( \frac{\partial \mathcal{L}}{\partial (\partial_\mu \Phi)} \right) - \frac{\partial \mathcal{L}}{\partial \Phi} = 0 \quad (2.2)$$



The complete Standard Model Lagrangian reads

$$\mathcal{L}_{\text{SM}} = \mathcal{L}_{\text{QCD}} + \mathcal{L}_{\text{EW}} + \mathcal{L}_{\text{Higgs}} \quad (2.3)$$

and splits up in three terms. The first two terms represent quantum chromodynamics, the theory describing the strong force, and the electroweak theory, which explains the electromagnetic and weak forces. The last term is connected to the Higgs-mechanism, which is responsible for the breaking of electroweak symmetry.<sup>[9;10]</sup>

<b>fermions</b>								
first generation			second generation			third generation		
flavor	charge [e]	mass [MeV]	flavor	charge [e]	mass [MeV]	flavor	charge [e]	mass [GeV]
u	2/3	2.3 $^{+0.7}_{-0.5}$	c	2/3	1275±25	t	2/3	173.1 ±0.9
d	-1/3	4.8 $^{+2.2}_{-1.7}$	s	-1/3	95±5	b	-1/3	4.18 ±0.3
e	-1	0.511	$\mu$	-1	105.7	$\tau$	-1	1.777
$\nu_e$	0	<0.002	$\nu_\mu$	0	< 0.19	$\nu_\tau$	0	< 0.018

<b>bosons</b>		
name	force mediated	mass [GeV]
gluon g	strong	0 (theory)
photon $\gamma$	electromagnetic	0 (theory)
$W^\pm$ -boson	weak	80.385 ± 0.015
Z-boson	weak	91.188 ± 0.003
H-boson	Higgs field	126.0 ± 0.6

Table 2.1.: The fundamental particles of the Standard Model, for all fermions there also exist antiparticles with opposite charge-like quantum numbers<sup>[2;8]</sup>

### 2.1.1. Gauge invariance and renormalisation

The two basic principles of quantum field theories are gauge invariance and renormalisability. Gauge invariance means that physics processes, thus the underlying basic equations, don't change under a certain transformation. This property can be shown in the case of quantum electrodynamics, the field theory describing the electromagnetic interaction.

For illustrating the principle of gauge invariance one can start with the Dirac Lagrangian which is

$$\mathcal{L}_{\text{Dirac}} = i\bar{\psi}\not{\partial}\psi - m\bar{\psi}\psi(x) \quad (2.4)$$

where the Feynman slash notation<sup>(1)</sup> is applied. Inserting equation 2.4 into 2.2 yields the Dirac equation

$$(i\cancel{\partial} - m) \psi(x) = 0 \quad (2.5)$$

which is the equation of motion of a spin  $\frac{1}{2}$  particle, like the electron, with mass  $m$ . This equation is invariant under a global gauge transformation  $U(1)_q$ <sup>(2)</sup> which looks like

$$\psi(x) \rightarrow \psi'(x) = e^{i\alpha} \psi(x) \quad (2.6)$$

Because of the global symmetry of the system, Noether's theorem implies that there has to be a conserved quantity, which, in this case, is the lepton number. However, (2.5) is not invariant under a local gauge transformation, in which  $\alpha$  becomes a function of space-time

$$\psi(x) \rightarrow \psi'(x) = e^{i\alpha(x)} \psi(x) \quad (2.7)$$

which one can see by inserting  $\psi'$  into the Dirac equation (2.5)

$$\begin{aligned} (i\cancel{\partial} - m) \psi'(x) &= (i\cancel{\partial} - m) e^{i\alpha(x)} \psi(x) \\ &= e^{i\alpha(x)} ((i\cancel{\partial} - m) \psi(x) - q\partial^\mu \alpha(x) \gamma_\mu \psi(x)) \end{aligned} \quad (2.8)$$

In this equation the second term  $q\partial^\mu \alpha(x) \gamma_\mu \psi(x) \neq 0$  spoils the invariance of the Dirac equation.

In order to restore the invariance under a local transformation, the derivative  $\partial_\mu$  has to be replaced by the covariant derivative  $D^\mu$

$$\partial^\mu \rightarrow D^\mu = \partial^\mu + ieA^\mu(x) \quad (2.9)$$

The covariant derivative introduces a new vector gauge field  $A_\mu$  representing a four vector potential for electromagnetism, which transforms as

$$A^\mu(x) \rightarrow A'^\mu(x) = A^\mu(x) + \frac{1}{e} \partial_\mu \alpha(x) \quad (2.10)$$

The crucial point is that by exchanging the derivative  $\partial^\mu$  with  $D^\mu$ , under the condition of (2.10), the Dirac equation is now invariant under a local gauge transformation of the form (2.7). According to Noether's theorem, this implies charge conservation.

This has been achieved by the introduction of a new vector field  $A_\mu$  which turns out to correspond to the photon. By replacing the derivative in the Dirac Lagrangian (2.4) and adding an invariant kinetic term for the photon field, one gets the gauge invariant Lagrangian of quantum electrodynamics

$$\mathcal{L}_{\text{QED}} = \bar{\psi} (i\cancel{\partial} - m) \psi + e\bar{\psi} A_\mu \psi - \frac{1}{4} F_{\mu\nu} F^{\mu\nu} \quad (2.11)$$

The first term describes a freely propagating electron, the second term represents the interaction between electrons and photons and the last term is the kinetic term for the photon field with

$$F_{\mu\nu} = \partial_\mu A_\nu - \partial_\nu A_\mu \quad (2.12)$$

<sup>(1)</sup>with  $\cancel{\partial} = \gamma^\mu \partial_\mu$  where  $\gamma^\mu$  denote the Dirac matrices and the Einstein summation convention is applied

<sup>(2)</sup>The  $U(1)_q$  is part of the unitarity group  $U(n)$ , where  $U(n)$  describes the set of  $n \times n$  dimensional matrices which satisfy  $U^\dagger U = 1$ . The subscript  $q$  denotes the conserved quantity in this gauge symmetry. One possible representation is  $U(\alpha) = e^{-i\alpha G}$ , where  $G$  is called the generator of the group.

Thereby, one is not allowed to write an additional mass term for the photon field, which would be of the form  $\frac{1}{2}m^2 A_\mu A^\mu$ , since this would spoil again gauge invariance. This means that the photon has to be massless, which agrees with the experimental upper limit for the photon mass of  $m_\gamma < 1 \cdot 10^{-18}$  eV<sup>[8]</sup>.

The need for a massless force carrier is crucial for gauge invariance, this will also be demanded in quantum chromodynamics and in the electroweak theory. In the end the requirement of massless gauge bosons gives rise to the Brout–Englert–Higgs mechanism, which will be discussed shortly. One could rise the question, whether it is necessary to care about gauge invariance in the Standard Model, but in fact gauge invariance is an essential feature for renormalisability. Renormalisability means that divergent terms which occur in the calculation of physical observables can be cured. Again, quantum electrodynamics serves as an example, namely the electron electron scattering.

Calculating the leading order Feynman diagram for this process (fig. 2.1a) works fine, but the answer is only approximate. In order to receive an exact solution, one also has to include higher order corrections, such as the so called vacuum polarisation (fig. 2.1b). In this process, something completely undesired happens: When calculating the corresponding matrix element, one picks up a term which essentially looks like

$$\int_{m^2}^{\infty} \frac{1}{z} dz \quad (2.13)$$

which clearly diverges for  $z \rightarrow \infty$ . Consequently the corresponding matrix element would equal infinity, which obviously contradicts the experiment. To prevent the integral from divergence, an upper cutoff value  $M^2$  is introduced, which in a later step, can be send to infinity, (2.13) becoming

$$\int_{m^2}^{M^2} \frac{1}{z} dz = \ln \left( \frac{M^2}{m^2} \right) \quad (2.14)$$

The essential point in renormalisation now is, that this term can be absorbed in physical quantities, as for this example, the charge. The idea is, that the quantity of charge measured in experiment, like in Thompson scattering, is not the same as the quantity of charge used in the theory calculations. One rather has to distinguish between a bare charge  $e_0$ , which enters the calculation and a renormalised charge  $e$  measured in experiment with

$$e \equiv e_0 \left( 1 - \frac{e_0^2}{12\pi^2} \ln \left( \frac{M^2}{m^2} \right) \right)^{\frac{1}{2}} \quad (2.15)$$

This way, the infinity introduced to the calculation of the matrix element is now absorbed in  $e$ . Since the measured charge in experiment is finite, the absorbed infinity has to be cancelled by a corresponding infinity in the bare charge  $e_0$ .

A direct result of this, is the energy dependence of the coupling constants. In quantum electrodynamics, the coupling constant  $\alpha$  is given by

$$\alpha(Q^2) = \frac{e^2(Q^2)}{4\pi} = \frac{\alpha(\mu^2)}{1 - \frac{\alpha(\mu^2)}{3\pi} \ln \left( \frac{Q^2}{\mu^2} \right)} \quad (2.16)$$

where  $Q$  denotes a transferred four-momentum and  $\mu$  is a reference renormalisation scale related to the cut-off value  $M^2$ . As it can be seen in figure 2.3, the coupling strength of quantum electrodynamics increases with larger momentum transfer, which has been experimentally verified.<sup>[11;12;13;14]</sup>

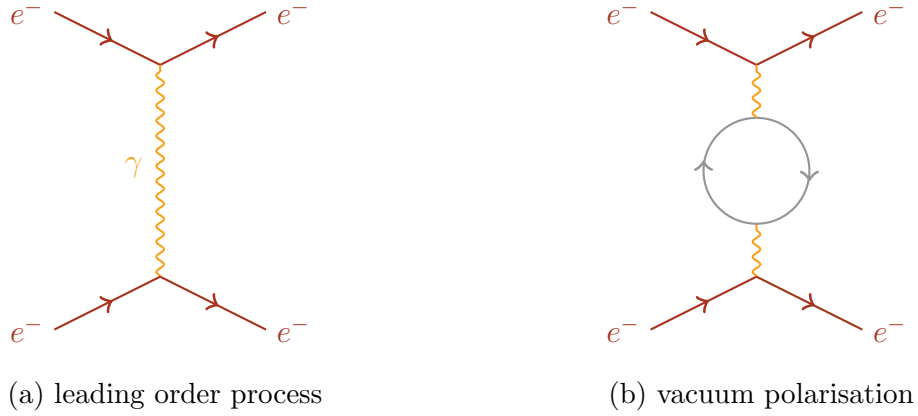


Figure 2.1: Electron electron scattering via the exchange of a virtual photon. The leading order process is shown on the left, a higher order correction, where a virtual photon splits up into an electron and positron pair which further annihilate again, on the right.

### 2.1.2. Quantum chromodynamics

The theory that describes the strong force is called quantum chromodynamics. It characterises the interaction of particles with colour charge, namely gluons and quarks. There are three kinds of colour charges: Red, green and blue which all can be understood as three axes of an abstract internal space. Since there is no distinguished colour, transformations in this space represent a symmetry. Such transformations are described by the  $SU(3)_C$  symmetry group<sup>(3)</sup>. A  $SU(N)$  set has a total of  $n^2 - 1$  generators, which translates into eight bicoloured gauge fields  $G_\mu^\alpha$ , called gluons. The Lagrangian is then given by

$$\mathcal{L}_{\text{QCD}} = -\frac{1}{4} \mathbf{G}_{\mu\nu} \mathbf{G}^{\mu\nu} + \sum_k \bar{q}_k (i\not{D} - m_k) q_k \quad (2.17)$$

where the sum runs over the different quark flavours. The corresponding covariant derivative reads

$$D_\mu = \partial_\mu + ig_s \frac{\boldsymbol{\lambda}}{2} \mathbf{G}_\mu \quad (2.18)$$

in which  $g_s$  denotes the coupling and where  $\boldsymbol{\lambda}$  and  $\mathbf{G}_\mu$  are vectors comprised of the group generators and respectively the gluon fields. The field strength tensor is given as

$$\mathbf{G}_{\mu\nu} = \partial_\mu \mathbf{G}_\nu - \partial_\nu \mathbf{G}_\mu - g_s \mathbf{G}_\mu \times \mathbf{G}_\nu \quad (2.19)$$

In addition to  $F_{\mu\nu}$  (2.12), this tensor contains a third term, which represents the fact, that the mediators itself, the gluons, carry colour and can consequently couple to themselves. This is a characteristic feature of quantum field theories, which are based on non-abelian symmetry groups. The additional possible vertices are shown in figure 2.2.

<sup>(3)</sup>the set of  $SU(N)$  is a subgroup of  $U(N)$  additionally fulfilling the constraint of  $|U| = 1$ , in the case of  $SU(3)$  the group generators can be represented by the Gell-Mann matrices  $\lambda_\alpha$



Figure 2.2: Additional vertices, due to the self coupling of gluons

The fact that gluons carry colour results in a coupling constant which reads

$$\alpha_s(Q^2) = \frac{g_s^2}{4\pi} = \frac{\alpha_s(\mu^2)}{1 + \frac{\alpha_s(\mu^2)}{12\pi} (33 - 2n_f) \ln\left(\frac{Q^2}{\mu^2}\right)} \quad (2.20)$$

where  $n_f$  is the number of quark flavours. Compared to the coupling constant of quantum electrodynamics (2.16), the striking difference is the sign of the logarithm. This means that  $\alpha_s$ , in contrast to  $\alpha$ , decreases for large four-momentum transfers  $Q^2$  while it increases for small  $Q^2$ , as it can be seen in fig. 2.3.

The regime of small distances<sup>(4)</sup> is called asymptotic freedom, since in this limit quarks behave as quasi-free particles. However, at larger distances, quarks are strictly bound into colourless objects, a phenomenon called confinement. The particles formed by quarks are called hadrons and can be subdivided in two groups, mesons and baryons.

Mesons consist of a quark and an antiquark, where the colour of the quark compensates the colour of the antiquark. Baryons, however, are made of three (anti-)quarks where each quark carries one of the three (anti-)colours. Consequently both, mesons and baryons are colourless particles. The process of quarks binding together to hadrons is referred to as hadronisation. This means that in an experiment instead of quarks one observes so called jets, consisting of uncoloured particles which were formed during the hadronisation process. [9;11;13;14;15]

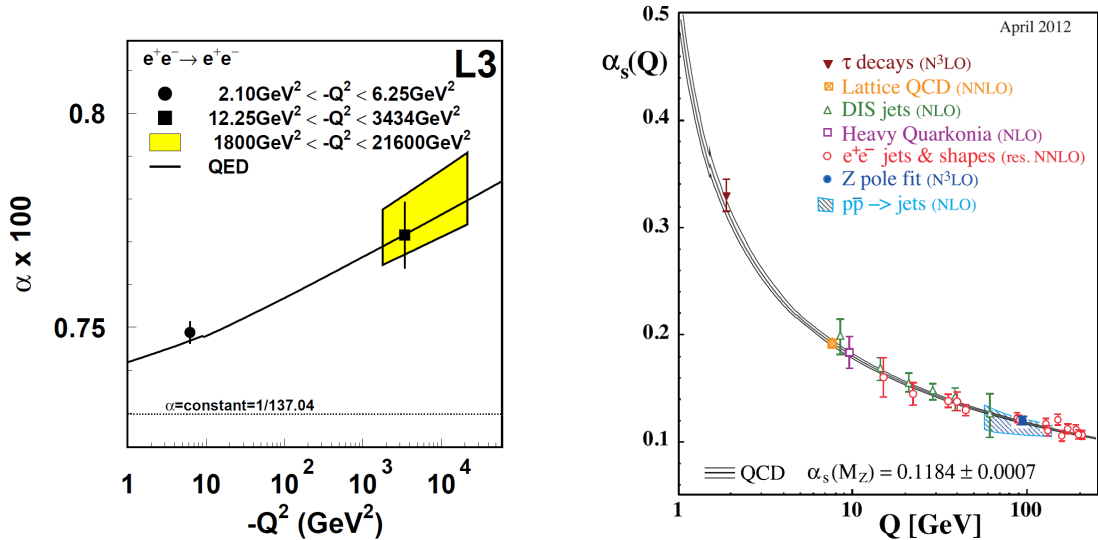


Figure 2.3: The running coupling constants of the electromagnetic interaction<sup>[16]</sup> on the left and strong interaction<sup>[8]</sup> on the right

<sup>(4)</sup>distance and energy are inversely proportional to each other

### 2.1.3. The electroweak theory

One of the tremendous achievements within the Standard Model is to show that both the electromagnetic and the weak force are low energy representatives of a single interaction.

This interaction is described by the electroweak theory, based on a  $SU(2)_L \times U(1)_Y$  gauge group, which implies four different gauge fields. Three of them,  $W_\mu^1$ ,  $W_\mu^2$  and  $W_\mu^3$ , are associated with the  $SU(2)_L$  and couple to the weak isospin<sup>(5)</sup>, where the fourth field  $B_\mu$  is affiliated with the  $U(1)_Y$  and couples to the weak hypercharge

$$Y = 2(Q - I_3) \quad (2.21)$$

here  $Q$  denotes the electrical charge and  $I_3$  represents the third component of the weak isospin. The Lagrangian of the electroweak theory is given by

$$\mathcal{L}_{\text{EW}} = \sum_k i\bar{\psi}_k \not{D}_\mu \psi_k - \frac{1}{4} \mathbf{W}_{\mu\nu} \mathbf{W}^{\mu\nu} - \frac{1}{4} B_{\mu\nu} B^{\mu\nu} \quad (2.22)$$

where the sum runs over the fermion flavours. The covariant derivative and field strength tensors are given by

$$D_\mu = \partial_\mu + \frac{1}{2} i g \tau \mathbf{W}_\mu + \frac{1}{2} i g' Y B_\mu \quad (6) \quad (2.23)$$

$$B_{\mu\nu} = \partial_\mu B_\nu - \partial_\nu B_\mu \quad (2.24)$$

$$\mathbf{W}_{\mu\nu} = \partial_\mu \mathbf{W}_\nu - \partial_\nu \mathbf{W}_\mu - g \mathbf{W}_\mu \times \mathbf{W}_\nu \quad (2.25)$$

In contrast to  $U(1)_Y$ ,  $SU(2)_L$  is a non-abelian group, thus equation (2.25) includes a term responsible for the self coupling of the gauge fields.

As already discussed, gauge bosons must not have mass, in order that equation 2.22 be invariant under local gauge transformations. Yet as experiments show, only one of the four gauge bosons of the electroweak interaction, the photon, is massless, while the  $W^\pm$  and  $Z^0$  are massive (cf. tab. 2.1). In order to satisfy gauge invariance and to meet the experimental data, the electroweak symmetry has to be broken.

Within the Standard Model this symmetry breaking can be achieved by the Higgs mechanism: In the electroweak Lagrangian a new complex scalar field

$$\Phi = \frac{1}{\sqrt{2}} = \begin{pmatrix} \phi^+ \\ \phi^0 \end{pmatrix} \quad (2.26)$$

is included. The additional terms of the Lagrangian then read

$$\mathcal{L}_{\text{Higgs}} = (D_\mu \Phi)^\dagger (D^\mu \Phi) - V(\Phi) \quad (2.27)$$

The potential  $V$  is given by

$$V(\Phi) = \mu^2 \Phi^\dagger \Phi + \lambda (\Phi^\dagger \Phi)^2 \quad (2.28)$$

<sup>(5)</sup>since only left handed fermions and right handed anti-fermions carry a weak isospin unequal zero, this is the same as saying the  $W_\mu^\alpha$  couple only to left handed particles and right handed antiparticles, which is known as parity violation

<sup>(6)</sup>this holds for left handed particles, the derivative for right handed particles reads:  $D_\mu = \partial_\mu + \frac{1}{2} i g' Y B_\mu$

and shown in figure 2.4. The minima of this potential depend on the choice of the parameter  $\mu^2$ . If  $\mu^2$  is selected to be larger than zero, the only minimum of  $V$  is at  $\Phi = 0$ . However, if one chooses  $\mu^2 < 0$ , the minima of the potential are shifted to

$$\Phi_{min} = \pm \sqrt{\frac{-\mu^2}{\lambda}} \equiv \pm \nu \quad (2.29)$$

where  $\nu$  is called the vacuum expectation value of the Higgs field. By choosing one of the  $\Phi_{min}$  particularly, the original symmetry of the potential is broken. This is referred to as spontaneously symmetry breaking, since the choice of the minimum is completely arbitrary. Expanding the potential around  $\Phi_{min}$  and rewriting the corresponding terms results in the physical mass eigenstates of the electroweak gauge bosons with their corresponding masses. By using the Weinberg angle  $\theta_W = \tan^{-1} \frac{g'}{g}$ , they can be written as

$$A_\mu = \sin \theta_W W_\mu^3 + \cos \theta_W B_\mu \quad m_\gamma = 0 \quad (2.30)$$

$$W_\mu^\pm = \frac{1}{\sqrt{2}} (W_\mu^1 \mp iW_\mu^2) \quad m_{W^\pm} = \frac{g\nu}{2} \quad (2.31)$$

$$Z_\mu^0 = \cos \theta_W W_\mu^3 - \sin \theta_W B_\mu \quad m_{Z^0} = \frac{m_{W^\pm}}{\cos \theta_W} \quad (2.32)$$

The two gauge fields of  $SU(2)_L$  are now absorbed in the  $W^\pm$  bosons. The photon and the  $Z^0$  are superpositions of the neutral  $W^3$  and the gauge field  $B_\mu$  of the  $U(1)_Y$  symmetry group. By adding an additional mass term to the Higgs Lagrangian, one can also account for fermions masses. This term reads

$$\tilde{g}_f \left( \bar{\Psi}_L^f \Phi \Psi_R^f + \bar{\Psi}_L^f \Phi^\dagger \Psi_R^f \right) \quad (2.33)$$

where  $\Psi^f$  denote the left and right handed Dirac spinors<sup>(7)</sup> of a fermion  $f$  and  $\tilde{g}_f$  its Yukawa coupling. With

$$m_f = \tilde{g}_f \frac{\nu}{\sqrt{2}} \quad (2.34)$$

the mass of a fermion is defined by the corresponding Yukawa coupling to the Higgs field. [11;12;15;17]

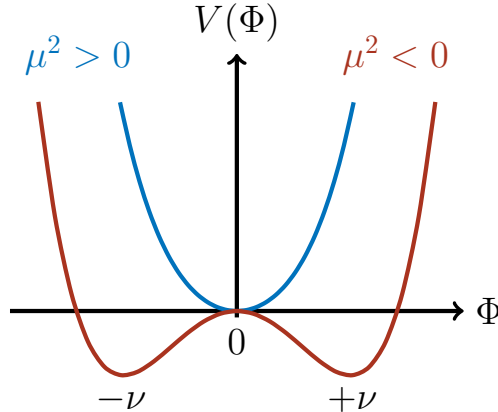


Figure 2.4: The potential  $V(\Phi)$  plotted for a one-dimensional scalar field  $\Phi$ , for both cases,  $\mu^2 > 0$  and  $\mu^2 < 0$ .

<sup>(7)</sup>because of the parity violation in the electroweak theory the left-handed spinors are represented by isospin doublets, while the right handed spinors are isospin singlets

In summary, the Standard Model of Particle Physics is a gauge theory which is described by a  $SU(3)_C \times SU(2)_L \times U(1)_Y$  symmetry group. In order to be renormalisable, the underlying symmetry of  $SU(2)_L \times U(1)_Y$  has to be broken. This electroweak symmetry breaking is achieved by the Higgs-mechanism, which ultimately gives rise to the masses of gauge bosons and elementary fermions.

## 2.2. The top-quark

The top-quark was discovered in 1995 by the experiments CDF<sup>[6]</sup> and D0<sup>[7]</sup> at the Tevatron accelerator. With a mass of  $m_{top} = 173.07 \pm 0.52 \pm 0.72 \text{ GeV}$ <sup>[8]</sup> it is the heaviest elementary particle known. The top-quark, mostly because of its high mass, plays an important role in various fields. Focusing on the most popular:

- the top-quark is the only quark which is not bound in hadrons. With a lifetime of  $\sim 10^{-24} \text{ s}$  it decays before it can hadronise. Thus, the study of the top-quark offers a unique possibility to measure bare quark properties.
- the Yukawa coupling of the top-quark is on the order of unity, therefore it could play an essential role in electroweak symmetry breaking.
- the top-quark is related to the question whether the vacuum is stable or not. Current results<sup>[18]</sup> point to a metastable vacuum, but for a final answer a more precise measurement of the top-quark mass is required.
- top-quarks are a major background for various processes in particle physics. A precise understanding of the top-quark properties is therefore crucial for the study of such processes.

To sum up, almost twenty years after its discovery, the research of the top-quark is far from over. With a wide range of analyses still ongoing and more being added continuously. In the next sections the production of top-quarks at particle accelerators and the corresponding decay topologies are discussed.

### 2.2.1. CKM matrix

For an appropriate discussion of top-quark production and decay, the CKM matrix has to be introduced. The CKM matrix, named after N. Cabibbo, M. Kobayashi and T. Maskawa, describes the mixing between the mass and the weak eigenstates of particles. The mass eigenstates represent the physical particles, with the weak eigenstates being the states the  $W^\pm$  bosons couple to. Since the electroweak symmetry is broken (cf. sec. 2.1.3), the two eigenstates are not identical. The weak eigenstates, denoted by a prime, can be written as superpositions of the mass eigenstates and vice versa, the relation between both is given by the CKM matrix:



$$\begin{pmatrix} d' \\ s' \\ b' \end{pmatrix} = \begin{pmatrix} V_{ud} & V_{us} & V_{ub} \\ V_{cd} & V_{cs} & V_{cb} \\ V_{td} & V_{ts} & V_{tb} \end{pmatrix} \begin{pmatrix} d \\ s \\ b \end{pmatrix} \quad (2.35)$$

The CKM elements are measured to be<sup>[8]</sup>:

$$V_{CKM} = \begin{pmatrix} 0.97427 \pm 0.00015 & 0.22534 \pm 0.00065 & 0.00351^{+0.00015}_{-0.00014} \\ 0.22520 \pm 0.00065 & 0.97344 \pm 0.00016 & 0.0412^{+0.00011}_{-0.00005} \\ 0.00867^{+0.00029}_{-0.00031} & 0.0404^{+0.0011}_{-0.0005} & 0.999146^{+0.000021}_{-0.000046} \end{pmatrix}$$

Focusing on the top-quark, the main point is that the probability for an electroweak process to change a quark flavour from  $i$  to  $j$ , is given by the particular CKM matrix element, as  $|V_{ij}|^2$ . As can be seen, the diagonal entries of the CKM matrix are almost unity, which means that a  $W$ -boson will preferably couple to quarks of the same generation.

For top-quarks, the corresponding CKM matrix elements give  $|V_{ts}|^2 = 7.5 \cdot 10^{-5}$ ,  $|V_{td}|^2 = 0.0016$  and  $|V_{tb}|^2 = 0.998$ . This means that if there is a top-quark involved in an electroweak process, in 99.8 % of the cases the top-quark is accompanied by a  $b$ -quark, instead of a  $d$  or  $s$ -quark.<sup>[13;19]</sup>

## 2.2.2. Top-quark production

To produce a top-quark, the minimum amount of energy needed is equal to the rest mass of the top-quark. On earth, this energy is, besides cosmic rays, only available at particle accelerators. The only collider having a sufficient centre-of-mass energy to produce top-quarks, is the LHC<sup>(8)</sup>.

There are two main mechanisms to produce top-quarks at hadron colliders. The first one, which is referred to as single top-quark production, is mediated via the electroweak interaction, while the second one is the production of a  $t\bar{t}$ -pair by the strong force.

### 2.2.2.1. Single top-quark production

Single top-quark productions can occur in three different channels. In the t-channel a top-quark is produced by a flavour excitation process. A virtual  $W$ -boson is radiated by a quark and couples to a  $b$ -quark, where the  $b$ -quark is either a sea quark from one of the hadrons or has its origin in a gluon splitting into a  $b\bar{b}$ -pair, thereby producing a top-quark.

The second production mechanism is the s-channel process, here an up-type quark annihilates with a down-type antiquark, or vice versa, to produce a virtual  $W$ -boson. This boson further splits up into a  $b$  and a top-quark.

The third and last mechanism is the associated production of a top-quark with a  $W$ -boson, referred to as  $Wt$ -channel. In this case either a  $b$ -quark is excited by a gluon, which hence has sufficient energy to decay into a  $W$ -boson and a top-quark, or a  $b$ -quark splits up into a virtual top-quark and a  $W$ -boson. The virtual top-quark then couples to a gluon, thereby

<sup>(8)</sup>as already mentioned, the top-quark was discovered at the Tevatron accelerator. Since the Tevatron has been shut down in 2011, the LHC is presently the only collider being able to produce top-quarks.

becoming real. The theoretical cross sections and Feynman graphs for the three processes can be found in table 2.2 and figure 2.5, respectively.

	t-channel [pb]	s-channel [pb]	Wt-channel [pb]
$\sigma_t$	$41.7^{+1.8}_{-0.8}$	$3.17^{+0.14}_{-0.11}$	$7.8^{+0.5}_{-0.6}$
$\sigma_{\bar{t}}$	$22.5^{+0.9}_{-1.0}$	$1.42^{+0.06}_{-0.07}$	$7.8^{+0.5}_{-0.6}$

Table 2.2.: Theoretical cross section predictions for single top-quark production at the LHC with  $\sqrt{s} = 7$  TeV and  $m_{top} = 173.0$  GeV<sup>[20;21;22]</sup>

It is worth mentioning, that at the LHC, the t-channel and s-channel cross sections for producing a top or an antitop-quark are different. This is caused by the structure of the proton itself, which is composed of one  $d$  and two  $u$  valence-quarks. In the case of the t-channel production the difference in cross sections can be understood in the following way: Since there applies charge conservation at each vertex, if radiating a  $W$ -boson, the  $u$ -quark has to emit a  $W^+$ , whereas the  $d$ -quark is obliged to radiate a  $W^-$ . Subsequently this  $W$ -boson, which is now  $W^+$  or  $W^-$ , annihilates either with a  $b$ -quark resulting in a top-quark or with a  $\bar{b}$ -quark producing an antitop-quark. As the number of  $u$  quarks in the proton is twice as large as the number of  $d$ -quarks and the sea quarks  $b$  and  $\bar{b}$  occur at same rate, the production cross section for top-quarks is roughly twice as large as the cross section of antitop-quark production. A similar argument holds for the s-channel. Since there are more  $u$ -quarks than  $d$ -quarks in the proton, the virtual  $W$ -boson, which is exchanged, will rather be a  $W^+$  than a  $W^-$ . This again leads to an enhanced cross section for top-quark production.

Taking these effects into account, the total predicted cross section of single top-quark production at the LHC is  $\sigma_{t/\bar{t}} = 84.4^{+2.2}_{-1.7}$  pb (cf. tab. 2.2).

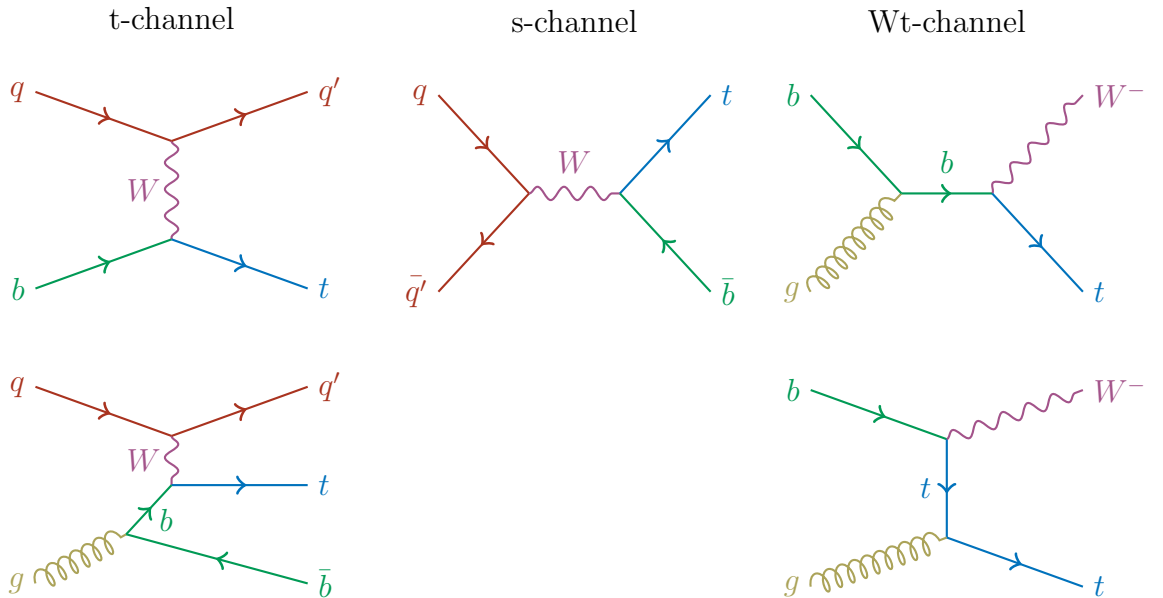


Figure 2.5: Production mechanism of top-quarks via the electroweak interaction

### 2.2.2.2. Top-quark pair production

In contrast to single top-quark production, the creation of a  $t\bar{t}$ -pair happens via the strong interaction. The leading order processes are shown in figure 2.6 and can be classified in three different categories, the s-, t- and u-channel. Similar to section 2.2.2.1, the s-channel production describes the annihilation of a quark and an antiquark under the emission of a gluon. The gluon subsequently splits up into a top and an antitop-quark. In contrast to the electroweak s-channel however, there is a supplementary process possible. As discussed in section 2.1.2, the gluons carry colour charge on their own and consequently couple to themselves. This allows the additional process, in which two gluons annihilate under the emission of a virtual gluon, again splitting up into a  $t\bar{t}$ -pair.

The t-channel, however, explicitly requires two gluons in the initial state. Under the exchange of a virtual top-quark, a new  $t\bar{t}$ -pair is created. The u-channel has in principle the same initial and final state particles as the t-channel, but it reverses the assignment of the top and antitop-quark to the initial state gluons.

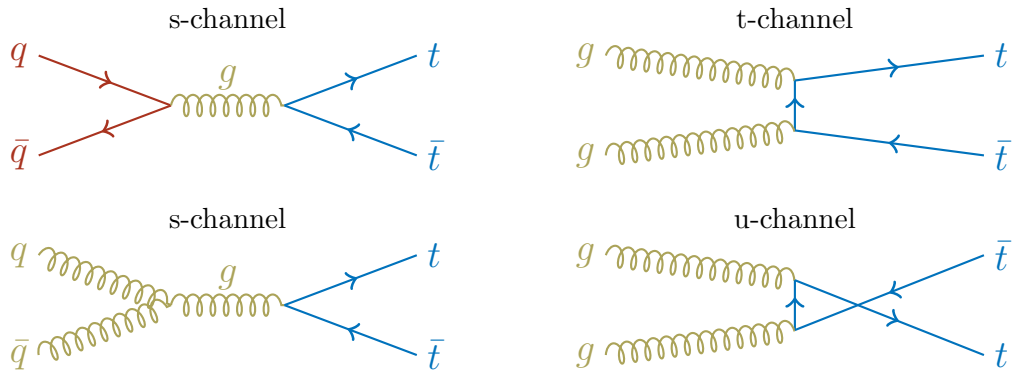


Figure 2.6: Feynman graphs of the leading order  $t\bar{t}$ -pair production mechanisms

In addition to the leading order diagrams, one can also include higher order processes, which for next-to-leading order are shown in figure 2.7.

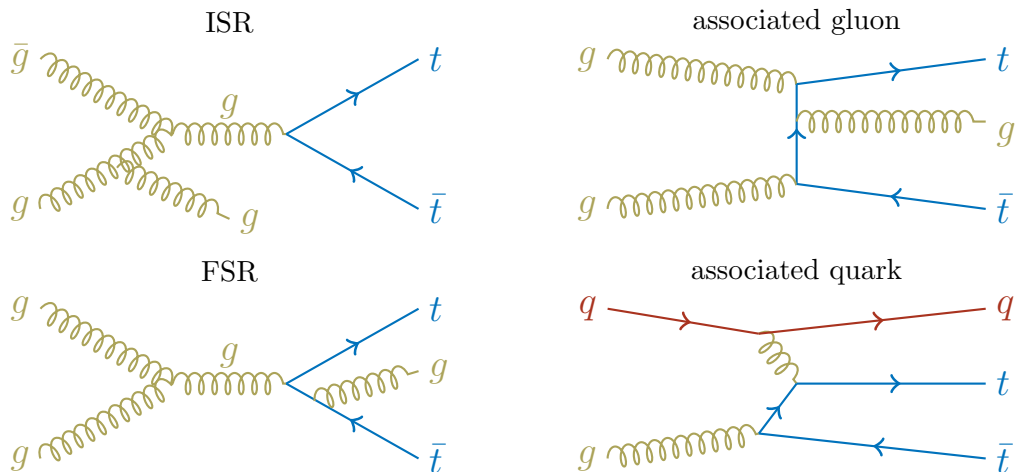


Figure 2.7: Feynman graphs of the next-to-leading order  $t\bar{t}$ -pair production

A simple case of such a correction is the initial or final state radiation, which means that a gluon is radiated by one of the ingoing or outgoing partons. The second is the production of a  $t\bar{t}$ -pair with an extra final state parton, which is referred to associated production. This can happen by the radiation of a gluon from the virtual top-quark in the t-channel, where the gluon appears as a final state particle. Another possibility is the associated quark production, which is in close analogy to one of the  $Wt$ -channel processes in figure 2.5. A  $t\bar{t}$ -pair with associated quark is produced, if an incoming quark radiates a virtual gluon, which combines with a virtual top-quark, originally emitted by an initial state gluon.<sup>[23]</sup> In total, the cross section for  $t\bar{t}$ -production with  $177_{-11}^{+10}$  pb<sup>(9)</sup> is roughly twice as large as the combined cross section of the electroweak production, and therefore the main mechanism for top-quark production at the LHC.

### 2.2.3. Top-quark decay

The top-quark decays via the electroweak interaction into a  $W$ -boson and a down-type quark. As already discussed in section 2.2.1, this down-type quark is mainly a  $b$ -quark. For a  $t\bar{t}$ -pair decay one can distinguish three different decay channels, characterised by the decay of the involved  $W$ -bosons.

A  $W$ -boson can either decay into a lepton plus a corresponding neutrino, which is referred to as leptonic decay or into an up-type quark and a down-type antiquark, and vice versa, called hadronic decay. Another main point is that although the process  $W \rightarrow tb$  is technically allowed, it is prohibited by the high rest mass of the top-quark, which is roughly twice as large as the  $W$ -mass. The corresponding branching fractions, which are  $\approx 1/3$  for a leptonic decay and  $\approx \frac{2}{3}$  for a hadronic decay, are given in table 2.3.

decay mode	$W \rightarrow e\nu_e$	$W \rightarrow \mu\nu_\mu$	$W \rightarrow \tau\nu_\tau$	$W \rightarrow q\bar{q}'$
branching ratio	$(10.75 \pm 0.13)\%$	$(10.57 \pm 0.15)\%$	$(11.25 \pm 0.20)\%$	$(67.60 \pm 0.27)\%$

Table 2.3.:  $W$ -boson decays with the corresponding branching fractions  $\Gamma_i/\Gamma$ <sup>[8]</sup>

Therefore the three modes of the  $t\bar{t}$ -decay are:

- the **dileptonic channel**, in which both  $W$ -bosons decay into leptons and neutrinos
- the **semileptonic channel**, in which one  $W$ -boson decays hadronically and the other one leptonically
- the **all-hadronic channel**, where both  $W$ -bosons decay into quarks

The corresponding probabilities for the different channels are shown in figure 2.11.

<sup>(9)</sup>The  $t\bar{t}$  cross section for  $pp$  collisions at a centre-of-mass energy of  $\sqrt{s} = 7$  TeV is  $\sigma_{t\bar{t}} = 177_{-11}^{+10}$  pb for a top-quark mass of 172.5 GeV. It has been calculated at next-to-next-to leading order (NNLO) in QCD including resummation of next-to-next-to-leading logarithmic (NNLL) soft gluon terms with top++2.0<sup>[24;25;26;27;28;29]</sup>. The PDF and  $\alpha_S$  uncertainties were calculated using the PDF4LHC prescription<sup>[30]</sup> with the MSTW2008 68% CL NNLO<sup>[31;32]</sup>, CT10 NNLO<sup>[33;34]</sup> and NNPDF2.3 5f FFN<sup>[35]</sup> PDF sets, added in quadrature to the scale uncertainty.

### 2.2.3.1. The dileptonic channel

With a probability of roughly 33 % for a  $W$ -boson to decay leptonically, the predicted branching ratio of this channel is 10.5%<sup>(10)</sup>. Therefore it has the smallest branching ratio of the three channels. Its final state signature is characterised by two  $b$ -quarks, two high energetic leptons and large  $E_T^{\text{miss}}$  (cf. fig. 2.8). Since there are two neutrinos in the final state, a kinematic reconstruction of the  $t\bar{t}$ -pair in this decay is not possible. To measure quark properties in this channel elaborated techniques have to be applied. Despite the low branching fraction and a minor background mainly from single top-quark production, the dileptonic decay offers a very clean event topology.

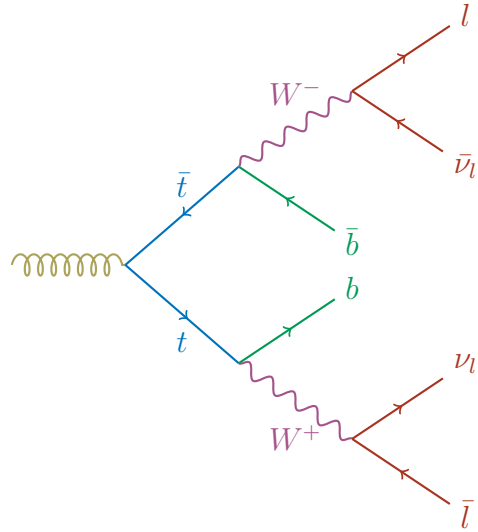


Figure 2.8: The dileptonic  $t\bar{t}$ -decay

### 2.2.3.2. The semileptonic channel

The theoretical chance that a  $t\bar{t}$ -pair decays semileptonically is 43.8%<sup>(10)</sup>. In this channel the final state consists of two  $b$ -quarks and two light-quarks, one high energetic electron and one neutrino (cf. fig. 2.9). In contrast to the dileptonic channel, the kinematic reconstruction of the  $t\bar{t}$ -decay is still feasible, although a neutrino is present. The main background in this channel originates in  $W + \text{jet}$  production, while a minor contribution comes from QCD multijet. Since the semileptonic decay channel is well-balanced between a clean event signature and a large branching fraction, it is the preferred channel for many top-quark measurements.

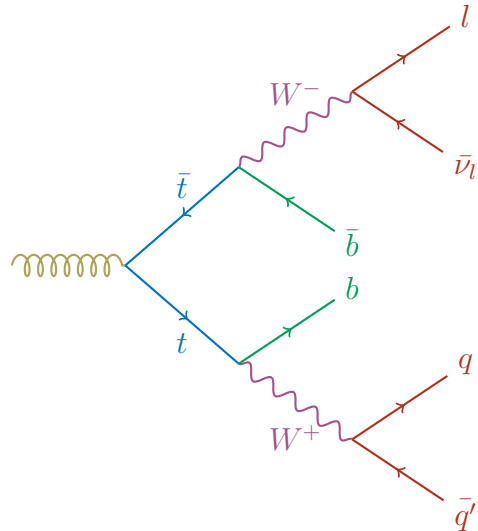


Figure 2.9: The semileptonic  $t\bar{t}$ -decay

<sup>(10)</sup>These numbers include the contribution from all three leptons<sup>[8]</sup>. Since  $\tau$ -lepton decays are to roughly 65% hadronic and furthermore always accompanied by a  $\nu_\tau$ , most analyses exclude  $\tau$  leptons from their top-quark measurements. This reduces the branching fractions to  $\approx 4.7\%$  and  $\approx 29.2\%$  in the dileptonic and semileptonic channel, respectively.

### 2.2.3.3. The all-hadronic channel

In the all-hadronic channel both  $W$ -bosons decay hadronically. This results in a probability of 45.7% for this channel. Therefore it has the largest branching ratio of the three channels. The event signature is described by four light and two  $b$ -quarks (cf. fig. 2.10). In contrast to the other two channels there are no high energetic leptons or neutrinos in the final state. The absence of neutrinos has the advantage that all decay particles of the  $t\bar{t}$ -system can be detected, allowing a full reconstruction. The predominant background for the all-hadronic channel is QCD multijet production. Due to the absence of leptons or  $E_T^{\text{miss}}$  the rejection of these background events is very challenging. Furthermore, since there are only quarks in the final state, a detailed understanding of the detector performance is crucial for precise measurements in this channel.

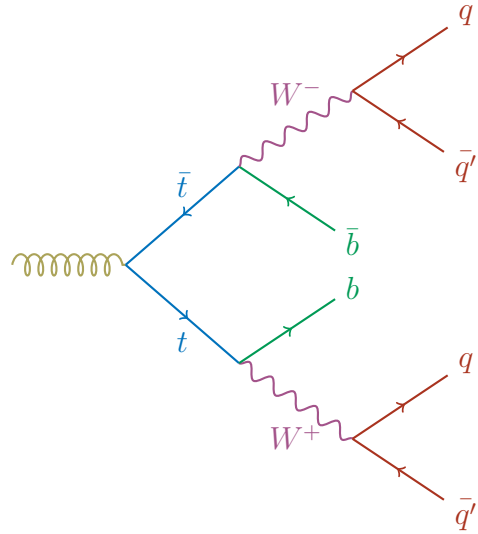


Figure 2.10: The all-hadronic  $t\bar{t}$ -decay

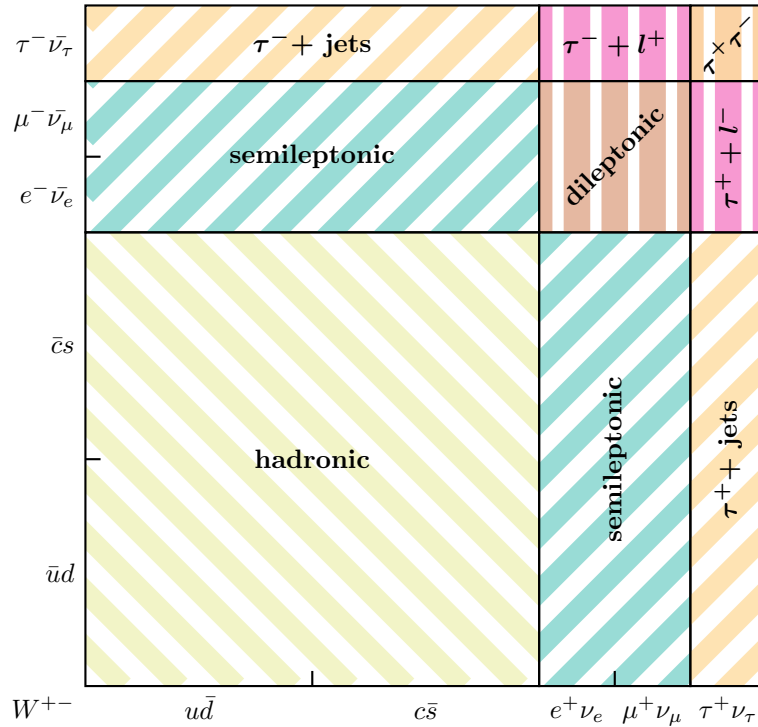


Figure 2.11: Decay channels of a  $t\bar{t}$ -system

### 3. Experimental setup

In the following, an overview of the experimental setup is given. While the first two parts briefly describe the LHC and the ATLAS experiment, the last part summarises the production of top quarks at the LHC.

#### 3.1. The Large Hadron Collider

The Large Hadron Collider (LHC) is an international experiment to test the Standard Model of Particle Physics and to unveil physics beyond. It is a superconducting accelerator based at the European Organization for Nuclear Research (CERN) near Geneva. The LHC is designed to accelerate and collide protons up to a centre of mass energy of 14 TeV. In addition, it also enables the collision of lead ions up to an energy of 2.76 TeV per nucleon.

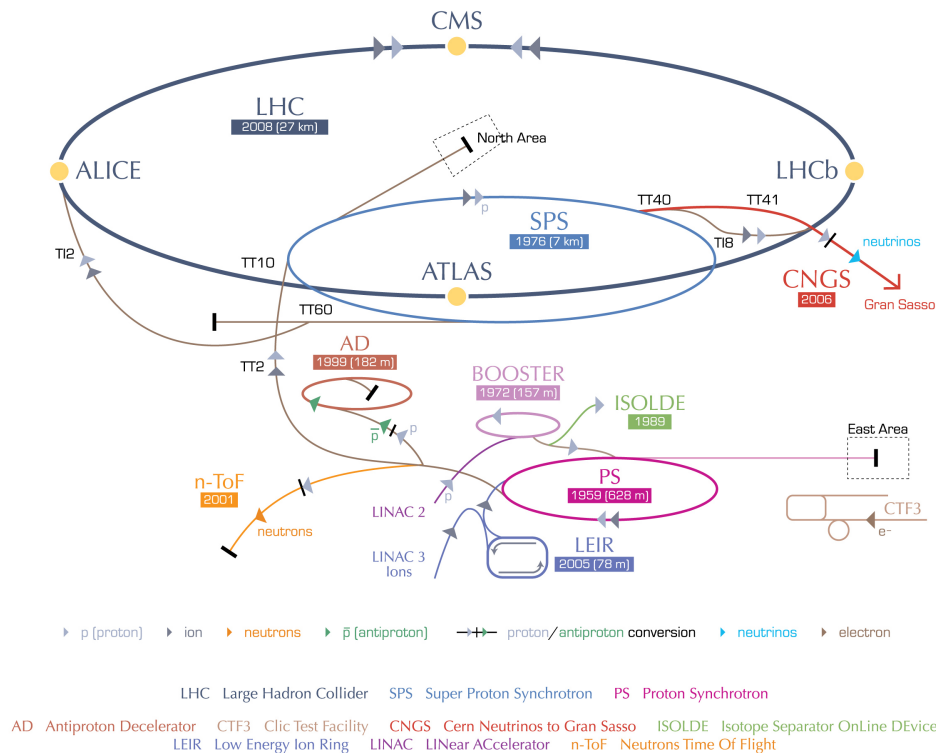


Figure 3.1: The CERN accelerator complex: The LHC ring with the four major experiments (in black) and the pre-accelerator chains for protons and heavy ions<sup>[36]</sup>

Besides two smaller experiments, LHCf and TOTEM, there are four major experiments affiliated to the LHC. The ALICE experiment is dedicated to the study of the quark-gluon plasma in heavy ion collisions, whereas the LHCb experiment is devoted to *b*-physics. The ATLAS

and CMS experiments are both general-purpose detectors covering a broad field of particle physics, with the benefit to cross check each others measurements.

Since the LHC is a particle-particle collider, it consists of two rings of counter-rotating beams. These rings are installed in the 27 km long tunnel originally built for the ancestor experiment LEP<sup>(1)</sup>. The LHC uses already existing infrastructure at CERN to pre-accelerate particles. Protons, in a first step, are pushed to 50 MeV in the Linac 2 accelerator. The particles are subsequently inserted in the Proton Synchrotron Booster and Proton Synchrotron to be further accelerated to 1.4 GeV and 25 GeV. The Super Proton Synchrotron speeds up the protons to 450 GeV as the last part of the pre-acceleration process. The particles are finally injected into the LHC rings and further accelerated by RF cavities, which are also responsible for the longitudinal focusing of the proton bunches. To keep the particles on circular paths, dipole magnets, with a nominal magnetic field of 8.33 T, are used. While quadropole magnets focus the beam in the transverse plan. A variety of additional magnets are in place for further beam corrections.

The observed number of proton-proton collisions in an experiment with a cross section  $\sigma_{event}$  is directly related to the performance of the collider via

$$N_{event} = L \cdot \sigma_{event} \quad (3.1)$$

where L denotes the luminosity, which is a sole function of collider parameters. The amount of data produced is then given by

$$\mathcal{L} = \int L \cdot dt \quad (3.2)$$

For the 2011 data taking period, the centre of mass energy denoted by  $\sqrt{s}$  was 7 TeV, while each ring was filled with 1380 bunches of up to  $1.45 \cdot 10^{11}$  protons and a spacing of 50 ns.<sup>(2)</sup> With this parameters, a peak luminosity of  $L = 3.6 \cdot 10^{33} \text{ cm}^2\text{s}^{-1}$  was achieved, corresponding to a total integrated luminosity delivered to the ATLAS experiment of  $\mathcal{L} = 5.63 \text{ fb}^{-1}$ , where one barn is defined as  $b = 10^{-24} \text{ cm}^2$ .<sup>[37;38]</sup>

## 3.2. The ATLAS experiment

The ATLAS detector<sup>(3)</sup> is a forward-backward symmetric multiple purpose detector based at the LHC ring at CERN. It is designed to cover a wide range of particle physics topics. Amongst other tasks, it aims to investigate the Higgs and top-sectors and to search for beyond Standard Model physics.

The ATLAS detector, presented in figure 3.2, has a cylindrical shape and consists of three main detector parts, the inner detector, the calorimeter and the muon spectrometer. In order to work properly the whole detector is embedded in a magnetic field. The huge amount of experimental data is handled by a trigger and data acquisition system.

Beside these main detector parts, which are briefly described in the following, there are three additionally smaller detector modules. The main purpose of the LUCID and ALFA detectors is to measure the luminosity delivered to ATLAS, while the intent of the zero-degree calorimeter is to determine the centrality of heavy-ion collisions.<sup>[39]</sup>

---

<sup>(1)</sup>the Large Electron Positron Collider has been shutdown in the year 2000

<sup>(2)</sup>the numbers are taken for the phase five of the 2011 data taking<sup>[37]</sup>

<sup>(3)</sup>ATLAS is the acronym for A Toroidal LHC Apparatus



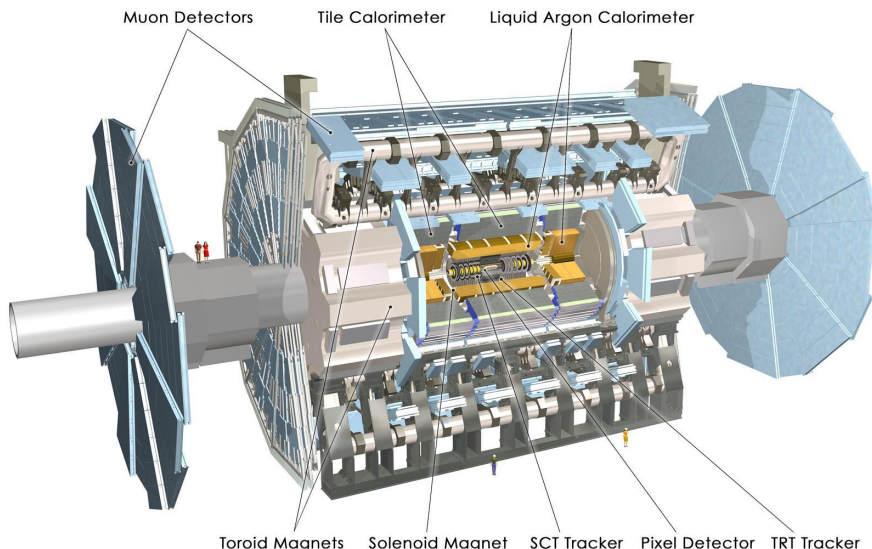


Figure 3.2: The ATLAS detector with its main components: The inner detector, the calorimeter, the muon spectrometer and the magnetic system<sup>[40]</sup>

### 3.2.1. The ATLAS coordinate system

The centre of the right handed ATLAS coordinate system is defined as the nominal interaction point of the colliding particles. In this system, the x-axis is pointing to the centre of the LHC ring, the y-axis is required to point upwards and the z-axis is defined to be along the beam-line. The plane spanned by the x- and y-axes is called the transverse plane and quantities carrying the label "T" are defined within this plane.

Coordinates used to describe positions in the detector are the azimuthal angle  $\phi$ , covering the transverse plane and the pseudorapidity  $\eta \equiv -\ln \tan \frac{\theta}{2}$ <sup>(4)</sup>. According to this, the distance between two objects is given by  $\Delta R = \sqrt{\Delta\phi^2 + \Delta\eta^2}$ .

### 3.2.2. The magnet system

The ATLAS magnet system consists of four superconducting aluminium-stabilised NiobTitan magnets, which are cooled to 4.5 K. The magnetic field provided by the magnets is essential for the inner detector and the muon spectrometer. According to the Lorentz force

$$\mathbf{F}_L = q(\mathbf{v} \times \mathbf{B}) \quad (3.3)$$

charged particles experience a force proportional to their momentum, which leads to a bending of the particle's path. Thus by measuring the particle's track, one can deduce its momentum. The ATLAS magnet system is shown in Figure 3.3 and splits up into a solenoid and three toroid magnets, which provide the magnetic fields for the inner detector and the muon spectrometer. The solenoid is centred along the beam axis and consists of 1154 windings. It is built to supply a central field of 2 T for the inner detector.

<sup>(4)</sup>where  $\theta$  denotes the polar angle with respect to the z-axis. For high energies,  $\eta$  is approximately equal to the lorentz-invariant rapidity  $y$ , defined as  $y = \frac{1}{2} \cdot \ln[(E + p_z) / (E - p_z)]$

The toroids, one in the barrel and two in the end-caps, consist of eight coils each. They are arranged radially symmetric around the beam axis, to minimise the interference with the particles under investigation. With a nominal current of 20.5 kA the barrel and the end-cap toroids provide a peak field of 3.9 T and 4.1 T. [39;41]

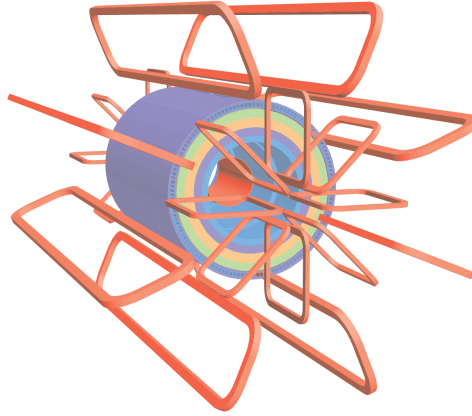


Figure 3.3: The ATLAS magnet system: Shown are the barrel coil, the end-cap toroidal coils and the solenoid embedded in the calorimeter (all shown in red) [39]

### 3.2.3. The inner detector

The inner detector is the most central element of ATLAS and was designed to provide high-precision momentum resolution and vertex identification. It covers the region from 5 cm to 115 cm from the beam axis and a pseudorapidity of  $|\eta| < 2.5$ . The inner detector is built of three parts, the pixel detector, the semiconductor tracker and the transition radiation tracker. In the barrel region, the different parts are arranged cylindrical around the beam pipe, while in the end-cap region the elements are attached on disks perpendicular to the beam.

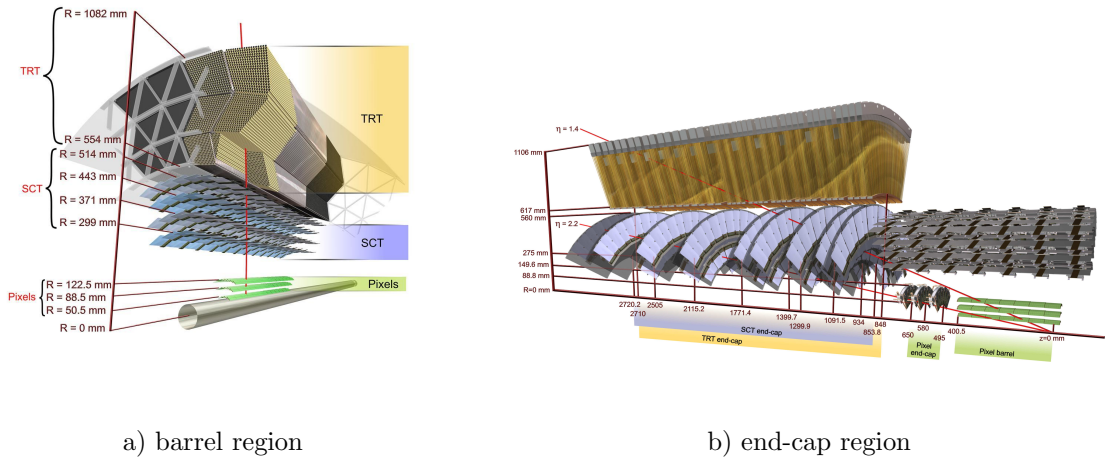


Figure 3.4: Schematic of the inner detector with its components: the pixel detector, the semiconductor tracker and the transition radiation tracker. [39]

The pixel detector is designed to give a hermetic coverage and a fine granularity. In order to be able to reconstruct secondary vertices from short lived particle decays like  $b$ -hadrons the

detector is as close to the interaction point as possible. It consists of 1744 overlapping pixel sensors, mounted on three barrels at radii of 50.5 - 122.5 mm from the beam axis, while in the end-caps region they are attached to disks with distances from 495 - 650 mm to the nominal interaction point. The pixel detector provides a spatial resolution of about  $\approx 10 \mu\text{m}$  in the  $R\text{-}\phi$  plane and  $\approx 115 \mu\text{m}$  in  $z$  direction.

The semiconductor tracker is composed of 4088 stereo silicon strip modules, each consisting of two layers rotated by 40 mrad with respect to each other. The elements are arranged in four barrels around the pixel detector and are mounted on nine disks in each of the end-caps. Overall, the semiconductor tracker covers an area of  $63 \text{ m}^2$  and is designed to give at least four precision space-point measurements, with an accuracy of  $\approx 17 \mu\text{m}$  in the transverse plane and  $\approx 580 \mu\text{m}$  along the beam direction.

The outermost part of the inner detector is the transition radiation tracker. It is build up of 4 mm thin gas-filled proportional drift tubes, equipped with an  $31 \mu\text{m}$  thick gold-plated tungsten wire. In the barrel region about 52544 of these tubes, each 144 cm long, are aligned in 73 layers along the beam pipe. Another 122880 tubes with a length of 37 cm are radially positioned in each end-cap. The transition radiation tracker has a spatial resolution of  $\approx 130 \mu\text{m}$  per tube and provides an average of 36 hits per track. Additionally, the identification of electrons is possible due to the detection of transition-radiation photons. [39]

### 3.2.4. The calorimeter

The ATLAS sampling calorimeter system consists of different types of calorimeters, which account for the varying physics environment in the detector. Its purpose is to measure the energies of the objects under investigation and to enable the reconstruction of jets, in a range of  $|\eta| < 4.9$ . To allow for the measurement of missing transverse energy the calorimeter system offers a full coverage in the azimuthal angle.

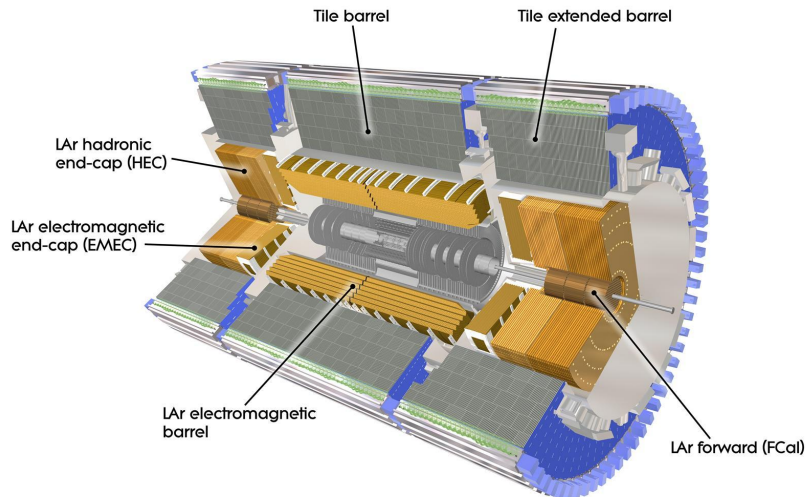


Figure 3.5: The ATLAS calorimeter system: **barrel region:** the electromagnetic calorimeter encloses the inner detector, which itself is enclosed by the tile calorimeter **end-cap region:** the electromagnetic end-cap calorimeter followed by the forward calorimeter, embedded in the hadronic end-cap calorimeter, surrounded by the extended tile barrel calorimeter [40]

### 3.2.4.1. EM calorimeter

The electromagnetic calorimeter is an accordion-shaped sampling detector specially designed to measure the energies of electromagnetically interacting particles. It uses lead as absorber and liquid argon as active medium. Liquid argon is chosen because of its linear behaviour, radiation hardness and stable response over time. The module uses an electric field to collect ionisation charges produced by incoming particles. A particle crossing the lead absorber material creates an electromagnetic cascade, which subsequently ionises argon atoms. With an electric field applied, the ionised charges, which are proportional to the energy of the incoming particle, drift to the electrodes and are readout.

The calorimeter covers a range of  $|\eta| < 3.2$ , with a barrel module sprawling up to  $|\eta| < 1.475$  and two end-cap modules extending in pseudorapidity from 1.375 to 3.2. The overlap between the modules ensures a continuous  $\eta$  coverage. With its fine granularity<sup>(5)</sup> and the additional presampler detector, an additional liquid argon layer at  $|\eta| < 1.8$ , the electromagnetic calorimeter provides a design energy resolution of  $\frac{\sigma_E}{E} = \frac{10\%}{\sqrt{E(\text{GeV})}} \oplus 0.7\%$ <sup>[42]</sup>. The electromagnetic calorimeter offers a total thickness of 22 and 24 radiation lengths for the barrel and end-cap regions.<sup>[39]</sup>

### 3.2.4.2. Hadronic calorimeter

The hadronic calorimeter consists of three different components, the tile calorimeter, the hadronic end-cap calorimeter and the forward calorimeter. All are sampling calorimeters, where the latter two employ liquid argon as active medium.

The main component of the hadronic calorimeter is the tile calorimeter. The barrel part covers a pseudorapidity of  $|\eta| < 1$ , while the extended barrels reach from  $0.8 < |\eta| < 1.7$ , the overlap again avoids gaps in  $\eta$ . The tile calorimeter surrounds the electromagnetic calorimeter and is made of steel absorbers and scintillating tiles. Attached to the scintillators are wavelength-shifting fibres, converting the light induced by ionising particles to visible light for readout photomultiplier tubes.

The hadronic end-cap calorimeter resides directly aside the electromagnetic end-cap calorimeters and is mounted on two wheels per end-cap. On each wheel 32 calorimeter modules are attached, using copper as absorber material. The 8 mm spacing between the copper plates is filled with liquid argon. The hadronic end-cap calorimeter covers a range of  $1.5 < |\eta| < 3.2$ , thereby overlapping with the forward calorimeter.

This last part of the ATLAS calorimeter system encloses the beam pipe and is surrounded by the electromagnetic and hadronic end-cap calorimeters. The forward calorimeter is mounted about 1.2 m apart from the electromagnetic barrel calorimeter to avoid the backscattering of neutrons into the same. It consists of three 45 cm long parts. The first one, closest to the interaction point, is a copper liquid argon calorimeter mainly designed to measure electromagnetic interactions, while the other two calorimeters are intended for hadronic measurements, with tungsten absorbers.

The design energy resolution of the tile and hadronic end-cap calorimeters is  $\frac{\sigma_E}{E} = \frac{50\%}{\sqrt{E(\text{GeV})}} \oplus 3\%$ <sup>[43]</sup>, where the forward calorimeter yields a resolution of  $\frac{\sigma_E}{E} = \frac{100\%}{\sqrt{E(\text{GeV})}} \oplus 10\%$ <sup>[44]</sup>. In total the hadronic calorimeter provides a thickness of about 10 interaction lengths over the whole region.<sup>[39]</sup>

<sup>(5)</sup>of about  $0.003 \times 0.1$  and  $0.025 \times 0.025$  in  $\Delta\eta \times \Delta\phi$ , for  $|\eta| < 1.40$  and  $1.40 < |\eta| < 1.75$ , respectively

### 3.2.5. The muon spectrometer

The task of the ATLAS muon spectrometer is to measure the tracks and momenta of muons and to enable triggering on them. Since muons are minimal ionising particles they are usually the only particles, except for neutrinos, which escape the inner parts of the detector.

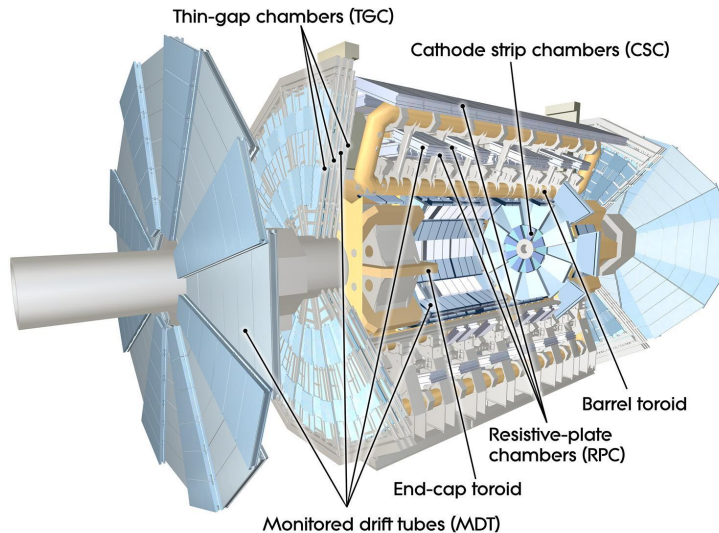


Figure 3.6: The ATLAS muon system<sup>[40]</sup>

For that purpose, ATLAS is equipped with monitored drift tubes, arranged in three consecutive cylindrical layers in the barrel and four disks in each end-cap region, covering a pseudorapidity of  $|\eta| < 2.7$ . Due to the high rate of particles near the beam axis, the first wheel in the region  $2.0 < |\eta| < 2.7$  is equipped with cathode strip chambers instead of monitored drift tubes.

The monitored drift tubes are designed to deliver precision-tracking information in the  $\eta$  plane. They consist of up to 8 layers of aluminum tubes with a diameter of 29.97 mm and are filled with a gaseous mixture of 93% argon and 7% carbon dioxide, mainly for its good resistance to ageing. In the middle of each tube, a 50  $\mu\text{m}$  thick gold-plated tungsten rhenium wire at a potential of 3080 V is strained. With this setup, a spatial z-resolution of about 35  $\mu\text{m}$  is achieved.

To trigger on muon tracks, the muon system is complemented with additional fast read-out resistive-plate and thin-gap chambers in the barrel and end-cap region. These detectors offer the benefit of providing a rough  $\phi$  position measurement with a resolution of about 3 – 10 mm.

### 3.2.6. The trigger and data acquisition system

Since it is not achievable to record all of the proton-proton collisions in the  $\approx 20 \cdot 10^6$  bunch crossings<sup>(6)</sup> per second occurring in the ATLAS detector, the purpose of the trigger and data acquisition system is to filter and record only the interactions of interest for the physics

<sup>(6)</sup>for the 2011 data taking period, with a bunch spacing of 50 ns. The average number of interactions per bunch crossing is 6 and 12, for  $\beta^* = 1.5$  m and  $\beta^* = 1.0$  m, respectively<sup>[45]</sup>

analysis. To enable that, a tripartite trigger system is in place, consisting of the level-1 trigger, the level-2 trigger and the event filter.

The task of the level-1 trigger is to search for high transverse momentum objects like electrons or jets and to look for high values of total and missing transverse energy. Since the level-1 trigger has to decide in  $< 2.5 \mu\text{s}$  whether to reject an event or not, it uses only limited detector information, namely from the muon system and the calorimeter, both with a reduced granularity. The level-1 trigger is build to handle a maximum rate of 100 kHz. If the level-1 trigger accepts an event, it defines regions of interest, which are handed over to the level-2 trigger. For these regions, which contain about 2 % of the total event data, the level-2 trigger utilises the full detector information to further reduce the number of events to a rate of 3.5 kHz. In a final step, the event filter, which employs an off line analysis procedure, reduces the rate to up to 600 Hz<sup>[46]</sup>.

The events which make it through the trigger system, each with a size of  $\approx 1.3$  Mbyte, are further analysed and stored permanently in dedicated computer centres across the world.<sup>[39]</sup>

### 3.3. Top-quark physics at the Large Hadron Collider

As previously discussed, there are two mechanisms to generate top-quarks. First, the single top-quark production via the electroweak interaction with a cross sections of  $\sigma_t = 84.4_{-1.7}^{+2.2}$  pb and secondly the creation of  $t\bar{t}$ -pairs through the strong force with  $\sigma_{t\bar{t}} = 177_{-11}^{+10}$  pb. This production happens either through the annihilation of a pair of quark and antiquark or the fusion of two gluons (cf. sec. 2.2.2).

To determine the dominant strong production process occurring at the LHC at a centre-of-mass energy of  $\sqrt{s} = 7$  TeV, one can look at the momentum fractions the interacting partons have to carry to produce a  $t\bar{t}$ -system. The squared centre-of-mass energy of two colliding partons can be written as

$$\hat{s} = (p_a + p_b)^2 \quad (3.4)$$

To produce a  $t\bar{t}$ -pair  $\sqrt{\hat{s}}$  has to be at least equal to the rest mass of the  $t\bar{t}$ -system, hence

$$\hat{s} = (p_a + p_b)^2 \geq (2 m_{top})^2 \quad (3.5)$$

The momentum of a parton  $p_i$  can be written in terms of the fraction  $x_i$  of the proton's momentum. In relativistic approximation, the momentum of the proton is described by the beam energy as

$$p_a = \begin{pmatrix} x_a \\ 0 \\ 0 \\ x_a \end{pmatrix} \cdot E_{beam} \quad p_b = \begin{pmatrix} x_b \\ 0 \\ 0 \\ -x_b \end{pmatrix} \cdot E_{beam} \quad (3.6)$$

With the assumption of  $x_a \approx x_b$  the moment fraction required to create a  $t\bar{t}$ -pair is

$$x \geq \frac{2 m_{top}}{\sqrt{s}} \quad (3.7)$$

where  $\sqrt{s} = 2 \cdot E_{beam}$  is the centre-of-mass energy of the collider.

For a centre-of-mass energy of 7 TeV and an assumed top-quark mass of 172.5 GeV, the momentum fraction a parton has to carry is about 0.05. The momentum fraction of partons

within a proton can be extracted from experimental data, which results in a so called parton distribution function. According to this function, the probability for a gluon to carry a fraction of 0.05 is much higher than for a quark (cf. Fig. 3.7). Consequently, the main  $t\bar{t}$ -production process at the LHC with roughly 80%<sup>[8]</sup> is the gluon gluon fusion.

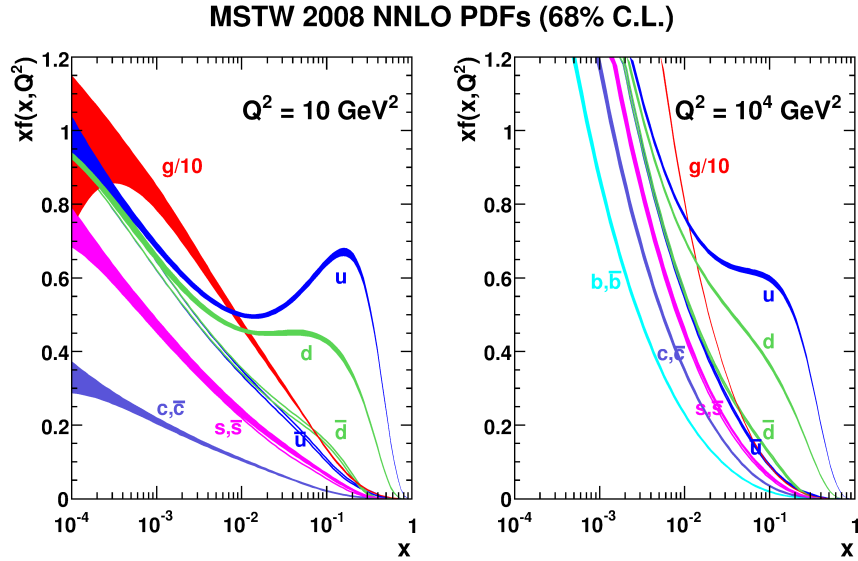


Figure 3.7: The MSTW2008NNLO parton density function, for a scale of  $Q^2 = 10 \text{ GeV}^2$  on the left and  $Q^2 = 10^4 \text{ GeV}^2$  on the right<sup>[47]</sup>

With the already mentioned cross section for the  $t\bar{t}$ -production and an instantaneous luminosity of  $L = 3.6 \cdot 10^{33} \text{ cm}^2\text{s}^{-1}$ <sup>[37]</sup> this results in about one  $t\bar{t}$ -event occurred every 1.5 s of LHC data taking, corresponding to roughly one million  $t\bar{t}$ -pairs produced in the whole 2011 data taking period.

## 4. Analysis

Purpose of this thesis is to investigate an approach for a precise measurement of the top-quark mass, denoted as  $m_{\text{top}}$ , in the all-hadronic channel. The precision of a measurement is obviously related to the size of the experimental error and splits up into a statistical and a systematic component. The statistical error reflects the fact that the measured value in an experiment can randomly fluctuate from one measurement to another. Such an uncertainty can only be reduced by repeating the measurement over and over again. The systematic error, however, is an intrinsic feature of the experimental setup, which results in a bias. In order to remove this kind of uncertainty, its source has to be identified and either eliminated, or at least its effects have to be reduced.

In the case of the top-quark mass, the uncertainty due to statistical fluctuations has been lowered by taking more and more experimental data over time, from  $\pm 8$  GeV measured by the CDF-collaboration at the time of the top-quark discovery<sup>[6]</sup>, to  $\pm 0.2$  GeV in one of the latest ATLAS results<sup>[48]</sup>. Since by now the statistical error is fairly small, the main bottleneck for a precise measurement of  $m_{\text{top}}$  is the systematic uncertainty. For the top-quark mass measurement this component consists of many different contributions, like:

- **Monte Carlo generator**, representing the variation between Monte Carlo programs
- **background modelling**, related to the quality of the background prediction
- **jet energy scale**, describing the uncertainty on the measurement of jet energies
- **ISR/FSR**<sup>(1)</sup>, considers the uncertainty introduced by the emission of additional partons
- **hadronisation**, accounting for the insufficient theoretical knowledge of building hadrons

One of the main systematic errors is the jet energy scale. This originates in the method, that is used to measure the top-quark mass. The principle idea is to extract  $m_{\text{top}}$  by a full kinematic reconstruction of the event. In order to restore the kinematics of the  $t\bar{t}$ -event, the objects in the final state are matched to the partons of the  $t\bar{t}$ -decay. Since there are only jets in the final state in the all-hadronic channel, a shift in the jet energy measurement directly translates into a change of the kinematics of the system, and therefore of  $m_{\text{top}}$ .

This thesis investigates a procedure to reduce the uncertainty on the jet energy scale, to decrease the systematic error on the top-quark mass. This is achieved by both choosing an estimator for  $m_{\text{top}}$ , which is less sensitive to the jet energy scale, and introducing an additional observable to account explicitly for this jet energy scale dependence.

---

<sup>(1)</sup>abbreviation for initial/final state radiation



In this chapter, first the concept of Monte Carlo generated data is established, while in a second part the physics objects used in the analysis are introduced. Subsequently, the reconstruction of the  $t\bar{t}$ -system is presented. In conclusion, the last section deals with the actual top-quark mass determination.

## 4.1. Monte Carlo datasets

The analysis presented in this thesis is solely based on Monte Carlo (MC) datasets. Monte Carlo generators are dedicated software tools intended to simulate real events, in order to study their properties. For that purpose, an event is split up into different sub processes. The first step emulates the hard scattering process. In case of  $t\bar{t}$ -production, this includes the scattering of the initial partons, as well as the production and decay of the  $t\bar{t}$ -pair. This is done by calculating the corresponding matrix element, taking into account a given parton distribution function. The second step replicates the emission of partons in the initial and final state, referred to as parton showering. Thereafter, the hadronisation of the final state partons and in the case of short lived particles, their subsequent decay is executed. Finally, the detector response is simulated. The name Monte Carlo hereby reflects the fact that Monte Carlo (pseudo-)random numbers are intended to reproduce the quantum mechanical probabilities of the various processes.

The hard process in this analysis is simulated by the next-to-leading order POWHEG [49;50;51] generator which uses the CT10 parton distribution function [34]. The parton showering, hadronisation and decay, however are simulated by the general-purpose generator PYTHIA [52], adopted to the Perugia2011C tune [53]. While the hard process and the parton showering, can be calculated in perturbative quantum chromodynamics, due to a small energy scale the hadronisation can not be treated perturbatively. A phenomenological approach has to be applied to describe this process, instead.

The approach used by PYTHIA is the Lund string model. In this approach coloured particles are connected by field lines, consisting of gluons. Due to their self coupling, these field lines form narrow tubes, referred to as strings. To explain the mechanism of hadronisation, it is instructive to look at the simple example of a  $q\bar{q}$ -pair (cf. fig. 4.1). By separating two quarks, the energy stored in the string between them increases linearly. For large separations the string breaks up into a new  $q'q'$ -pair, thereby forming two uncoloured systems,  $q\bar{q}'$  and  $q'\bar{q}$ , each connected again by a colour string. This process will recur, until only final state hadrons are left. [54;55]

The final step in the Monte Carlo dataset production is the detector simulation, which is done with the GEANT4 package [56].

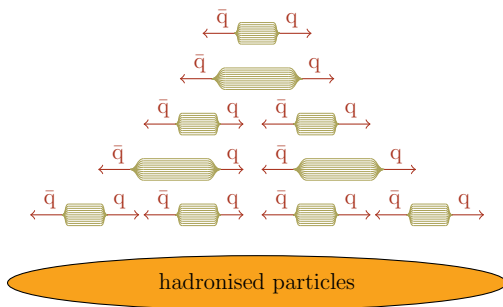


Figure 4.1: The Lund string model shown for a  $q\bar{q}$ -system

This analysis is based on various Monte Carlo datasets with all-hadronic  $t\bar{t}$ -events only, simulated for the 2011 data taking period of the LHC. The samples differ in the used simulated top-quark mass and the level of detail of the ATLAS detector simulation. As signal Monte Carlo, a dataset with  $m_{top}^{sim} = 172.5$  GeV and a full detector simulation is used. Additionally, seven samples with different top-quark masses ranging from 165 - 180 GeV are employed. Since a full detector simulation is very CPU time consuming, the detector response in these samples is simulated with a faster simulation, referred to as ATLFAST II. This approach uses a simplified description of the ATLAS calorimeter, while the inner detector and muon system are still simulated in full precision. Like this, CPU time reduces by a factor of ten.<sup>[57]</sup> An overview over the different Monte Carlo datasets together with the containing number of events, is given in table 4.1

MC dataset	$m_{top}^{sim}$ [GeV]	$\sigma_{t\bar{t}}$ [pb]	k-factor	# of events	detector simulation
signal sample	172.5	67.36	1.229	$3.5 \cdot 10^6$	full simulation
mass variation 1	165.0	84.71	1.132	$1.5 \cdot 10^6$	ATLFAST II
mass variation 2	167.5	78.39	1.132	$1.5 \cdot 10^6$	ATLFAST II
mass variation 3	170.0	72.72	1.130	$1.5 \cdot 10^6$	ATLFAST II
mass variation 4	172.5	67.36	1.229	$4.0 \cdot 10^6$	ATLFAST II
mass variation 5	175.0	62.51	1.131	$1.5 \cdot 10^6$	ATLFAST II
mass variation 6	177.5	58.11	1.130	$1.5 \cdot 10^6$	ATLFAST II
mass variation 7	180.0	53.98	1.131	$1.5 \cdot 10^6$	ATLFAST II

Table 4.1.: MC datasets used in this analysis, with the corresponding cross sections, k-factors and number of events.<sup>(2)</sup>

## 4.2. Physics object definitions

The physics objects used in this analysis are electrons, muons, missing transverse energy and jets. The criteria<sup>(3)</sup>, that objects have to fulfil to be considered in the analyses, are given in this section. Figure 4.2 shows the tracks some fundamental particles leave in the ATLAS detector.

### 4.2.1. Electrons

Within ATLAS, electrons are reconstructed by searching for seed clusters in the electromagnetic calorimeter, which exceed a threshold value of 2.5 GeV. These clusters have a size of  $0.075 \times 0.125$  in the  $\eta/\phi$ -plane and are selected by a sliding window algorithm<sup>[59]</sup>. If at least one track from the inner detector can be associated to a seed cluster, within  $\eta < 2.5$ , this object is identified as an electron.

Three sets of selection criteria exist. They differ in their background rejection power and are referred to as loose, medium and tight. These cut-based selections take diverse tracking and calorimeter variables into account and vary in the stringency of their cut-values. The selection

<sup>(2)</sup>The k-factor is a correction, which accounts for higher order contributions to the cross section.

<sup>(3)</sup>The applied criteria are in accordance with the ATLAS top-quark working group recommendations for 2011 analysis<sup>[58]</sup>.

criteria are inclusive, that means that in order to fulfil the tight requirement, an electron also has to meet the loose and medium conditions. [59;60]

For being considered in this analysis, electrons identified by the ATLAS electron algorithm have to satisfy the following specifications:

- meet the tight++ selection criteria<sup>(4)</sup>
- be within a region of  $|\eta| < 2.47$ , excluding the sector of  $1.37 < |\eta| < 1.52$
- exceed a transverse energy of 25 GeV
- have a longitudinal impact parameter smaller than 2 mm
- fulfil isolation criteria<sup>(5)</sup>

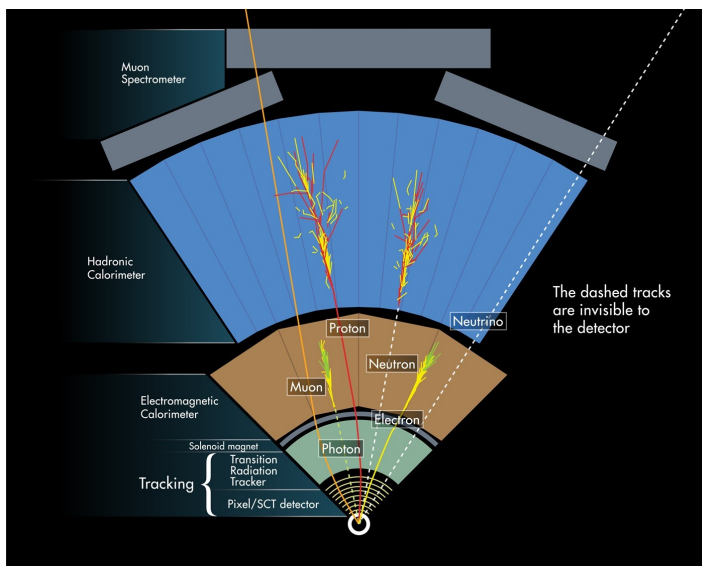


Figure 4.2: Identification of particles in the the ATLAS detector<sup>[40]</sup>

#### 4.2.2. Muons

Muons are reconstructed by a set of complementary algorithms utilising information from the muon spectrometer and inner detector. The algorithms can be divided into three categories. The standalone reconstruction extrapolates tracks in the muon spectrometer back to the interaction point. It explicitly takes the energy loss and multiple scatterings of muons in the detector into account. The combined reconstruction, however, matches hits of both, the muon spectrometer and the inner detector, in order to reconstruct a single track for a muon. Finally, the tagging method associates inner detector tracks to proximate hits in the muon spectrometer.

<sup>(4)</sup>tight++ represents an optimised tight selection for the 2011 data taking period

<sup>(5)</sup>In order to reduce the rate of hadrons mimic leptons and to reject leptons from heavy flavour decays within jets, the sum of transverse energy in a cone of  $\Delta R = 0.2$  around the electron must not exceed an  $E_T$  and  $\eta$ -dependent value, varying from 1.4 to 3.7 GeV. For the same purpose the sum of transverse momentum within a cone of  $\Delta R = 0.3$  has to be smaller than 1 GeV. Additionally the distance in  $\Delta R$  of the lepton to the next jet may not come below a value of 0.4

By 2012 there were two sets of reconstruction algorithms employed, referred to as Staco muon collection and MuID collection. Both sets apply algorithms of each kind to identify muons, while their name origins in the particular combined reconstruction algorithm used. The Staco algorithm performs a statistical combination of tracks in both subsystems, while the MuID algorithm does a combined refit of the hits in the muon spectrometer and inner detector.<sup>[61]</sup> In order to be used in the analysis, muons have to:

- be identified by the MuID algorithm
- lie in a pseudorapidity range  $|\eta| < 2.5$
- exceed a transverse momentum of 20 GeV
- have a longitudinal impact parameter smaller than 2 mm
- fulfil isolation criteria<sup>(6)</sup>
- not be cosmic<sup>(7)</sup>

### 4.2.3. Jets

As discussed in sections 2.1.2 and 4.1, quarks can not be observed in nature, but form narrow sprays of particles instead. Such bunches of particles are commonly referred to as jets.

#### 4.2.3.1. Jet reconstruction

In ATLAS jets consist of topological clusters constructed from neighbouring calorimeter cells, exceeding a certain signal to noise ratio. An algorithm searches for cells, passing a threshold ratio of 4 and adds them to a ‘seed list’. For each cell in the seed list all neighbouring cells are considered. If an adjacent cell exceeds a signal to noise ratio of 2, it is merged to the cluster and appended to a ‘neighbour seed list’. After processing the original seed list, it is replaced by the list of neighbouring seeds and the last step is repeated. This procedure is iterated until there are no more entries left in the resulting list. Finally, all cells contiguous to the topological clusters are attached as well. The resulting energy of the cluster is the sum of the individual calorimeter cells. Its direction, however, is a weighted average of the individual cells, with respect to the origin of the ATLAS coordinate system.<sup>[62]</sup>

The combination of the resulting topological clusters to jets is done with the anti- $k_t$  jet clustering algorithm<sup>[63]</sup> which is included in the FastJet software package<sup>[64]</sup>. In a first step, the separations for each pair of topological clusters  $i$  and  $j$  are calculated according to

$$d_{ij} = \min \left( k_{T_i}^{-2}, k_{T_j}^{-2} \right) \frac{\Delta R_{ij}}{R^2} \quad (4.1)$$

<sup>(6)</sup>see (5), but for muons the thresholds are 4 GeV and 2.5 GeV, for the sum of transverse energy and momentum, respectively.

<sup>(7)</sup>cosmic muons appear as a pair of oppositely signed muons in the detector. Oppositely signed muons are rejected if their distance from the interaction point is larger than 0.5 mm and their separation in  $\phi$  exceeds 3.1

where  $R$  is a radius parameter given to the algorithm and  $\Delta R_{ij}$  represents the separation of the corresponding objects in the  $\eta - \phi$  plane. Additionally, the separation of the cluster  $i$  to the beam axis is evaluated with

$$d_{iB} = k_{ti}^{-2} \quad (4.2)$$

If the minimum of the  $d_{ij}$  values is smaller than  $d_{iB}$  the clusters  $i$  and  $j$  are combined. If the smallest  $d_{ij}$  is larger than  $d_{iB}$ , the object  $i$  is called a jet and is removed from the list of available objects. This process is repeated until all topological clusters in the event have been assigned to a jet. Finally, the four-momenta of the jets are built by summing up the four-momenta of the corresponding topological clusters.

The advantage of the anti- $k_t$  algorithm is that it offers both circular cone shaped jets and IRC safety. This stands for infrared and collinear safety and means, that the jet does not disappear neither under the emission of a soft particle nor by the splitting of a parton into two collinear particles (cf. fig. 4.3).

In this analysis jets have been reconstructed with a radius parameter of 0.4. To be considered, a jet has to be within a pseudorapidity region of  $|\eta| < 2.5$  and is required to be separated to an electron by  $\Delta R > 0.2$ . To reduce the sensitivity to pile-up, only jets with a jet vertex fraction larger than 0.75 are considered.<sup>(8)</sup>

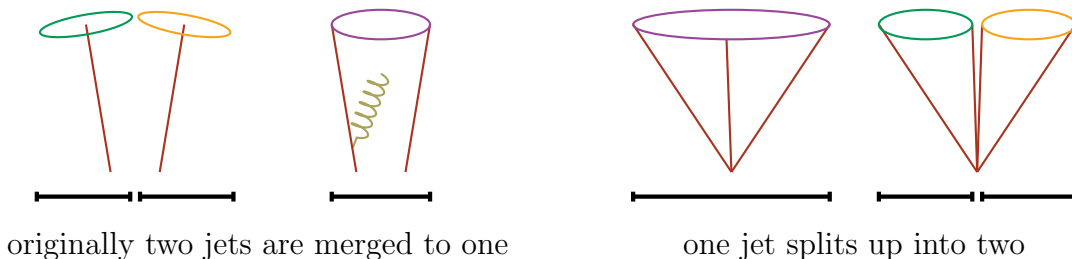


Figure 4.3: Behaviour of a not infrared and collinear safe jet reconstruction algorithm

#### 4.2.3.2. B-tagging

Additionally to pure jet reconstruction there is also, to a certain extent, the possibility to determine the flavour of the quark which has induced the jet. One differentiates between jets originating from gluons,  $u$ -,  $d$ -,  $s$ - or  $c$ -quarks and jets stemming from  $b$ -quarks, referred to as light<sup>(9)</sup> and  $b$ -jets. The identification of the jet flavour is done by elaborated algorithms which use  $b$ -hadron decay characteristics. The main feature exploited by these tagging algorithms is the comparatively long life-time of  $b$ -hadrons, which causes a displaced vertex in the detector. In ATLAS a combination of different algorithms is used to differentiate light from  $b$ -jets. The MV1  $b$ -tagging algorithm consists of a neural network. It utilises the output weights of the IP3D and SV1 taggers and a combination of the JetFitter + IP3D algorithm as input. To discriminate light from  $b$ -jets, the IP3D tagger uses the impact parameter between tracks associated to the jet and the primary vertex, while the SV1 algorithm explicitly reconstructs the secondary vertex of the  $b$ -hadron decay. The JetFitter tagger exploits the topology of

<sup>(8)</sup>The jet vertex fraction represents the probability that a jet originates from the primary vertex. It is determined by associating tracks from the inner detector to jets reconstructed within the calorimeter.<sup>[65]</sup>

<sup>(9)</sup>for this analysis also jets origin from  $c$ -quarks are referred to as light-jets

weak  $b$  and the subsequent  $c$ -quark decays, to deduce the origin of the jet.<sup>[66]</sup>

In this analysis the MV1 tagger is chosen to work at an efficiency of 70 %, which represents the probability with which a jet originating from a  $b$ -quark is tagged by the algorithm.

#### 4.2.3.3. Jet energy scale

Since there are various effects, which affect the measurement of jet energies in the calorimeter, one important question is how to calibrate a reconstructed jet energy to its original value. Such calibrations have been done by investigating the electromagnetic response of the calorimeter in dedicated test beams. However, the total energy of a jet not only involves electromagnetic deposits but also comprises:

- hadronic energy, introduced by decays to mesons and baryons
- invisible energy, carried away from uncharged particles like neutrons
- escaped energy, due to decays involving neutrinos

Besides these effects, related to how the energy of a jet is deposited in the calorimeter, it also has to be accounted for implications like:

- additional energy deposits, due to pile up and the underlying event<sup>(10)</sup>
- inefficiencies of the jet algorithm, e.g. out of cone particles
- detector related issues like poorly instrumented regions or noise

In order to compensate the various effects and restore the original jet energies, a  $p_T$  and  $\eta$  dependent correction scheme, referred to as jet energy scale, is employed. For this purpose the jet energy scale incorporates four different corrections:

- **pile-up correction:** the average additional energy introduced by multiple proton-proton interactions is subtracted from the jet energy
- **vertex correction:** topological clusters are evaluated with respect to the nominal interaction point of the ATLAS detector. Therefor the jet coordinates  $\eta$  and  $\phi$  are modified to point to the primary vertex of the interaction
- **jet energy calibration:** the reconstructed energies are compared to dedicated Monte Carlo simulations and corrected accordingly
- **in situ calibration<sup>(11)</sup>:** the jet energy is corrected by exploiting the  $p_T$  balance in real data events, as for example a jet recoiling from a photon or  $Z$  boson, or a subsystem of low  $p_T$  jets recoiling from a high  $p_T$  jet

<sup>(10)</sup>The underlying event denotes processes, which occur aside the primary hard scattering in a proton-proton collision.

<sup>(11)</sup>The in situ calibration is only used for data events

Figure 4.4 shows the result of the jet energy scale calibration, in terms of the average energy response  $\mathfrak{R}$ , for the 2011 data taking period. The quantity  $\mathfrak{R}$  corresponds to the inverse of the jet energy correction, and is defined as the ratio of the measured jet energy on the electromagnetic scale and the original energy of the jet.

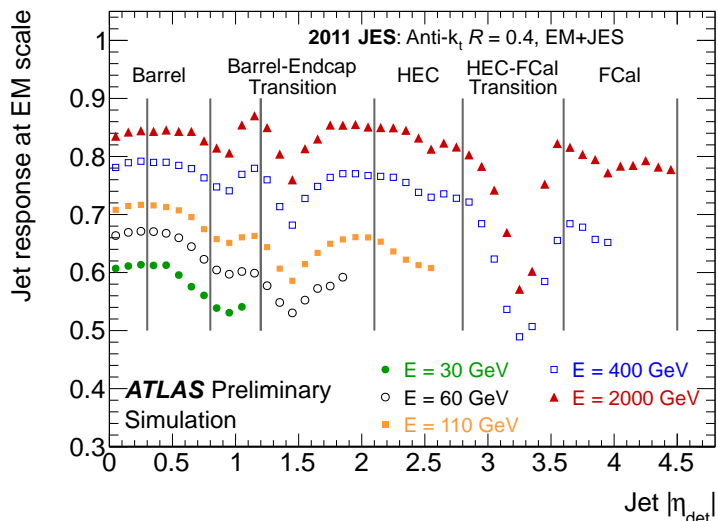


Figure 4.4: The average jet energy response for 2011 data taking as function of the jet  $\eta$ . The different colours represent different values of the jet energy.<sup>[67]</sup>

Despite the effort undertaken to calibrate the response of the calorimeter, a residual uncertainty on the jet energy scale remains. This error has to be considered in analyses and is one of the largest contributions to the total uncertainty in the case of the top-quark mass measurement.

Since the response of the calorimeter is flavour dependent<sup>(12)</sup>, it is sensible to split the error on the jet energy scale into two components. One for light-jets and one for  $b$ -tagged jets. The corresponding uncertainties for light and  $b$ -tagged jets for 2011 data are shown in Figure 4.5.<sup>[67;68]</sup>

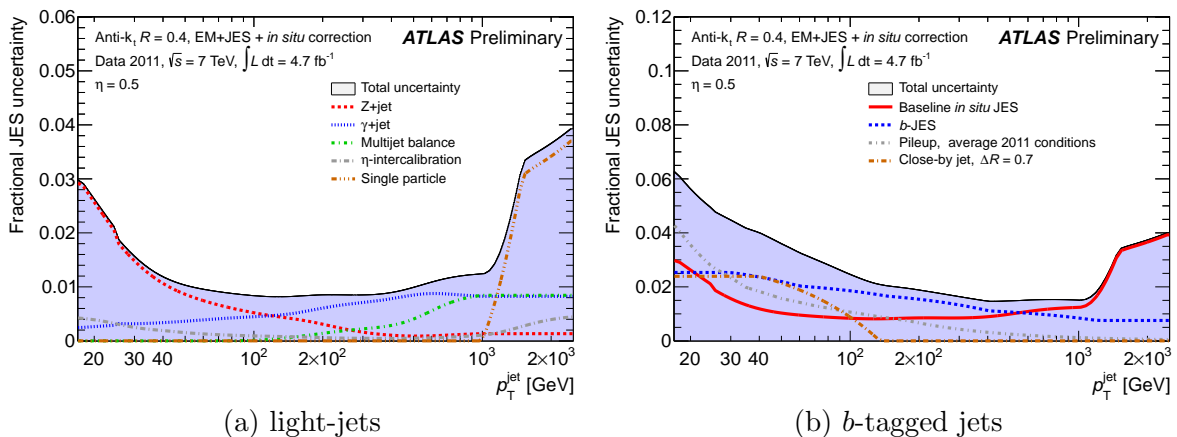


Figure 4.5: Relative errors on the jet energy scale for the 2011 data taking period, for light-jet flavours, left, and  $b$ -tagged jets on the right.<sup>[67]</sup>

<sup>(12)</sup> For example the average energy loss due to decays involving neutrinos is larger for  $b$  induced than for light-jets.

#### 4.2.4. Missing transverse energy

Unfortunately at the LHC a total missing energy can not be defined, since at hadron colliders it is not possible to determine the momentum fraction of the initial partons. The quantity of transverse missing energy  $E_T^{\text{miss}}$  has to be used instead. It is defined as

$$E_T^{\text{miss}} = \sqrt{(E_x^{\text{miss}})^2 + (E_y^{\text{miss}})^2} \quad (4.3)$$

with

$$- E_{x,y}^{\text{miss}} = E_{x,y}^{\text{elec}} + E_{x,y}^{\text{muon}} + E_{x,y}^{\text{jet}} + E_{x,y}^{\text{soft jet}} + E_{x,y}^{\text{cell out}} \quad (4.4)$$

Hence, the missing transverse energy contains contributions from electrons, muons and jets. The latter one is split up into a part for jets with  $p_T > 20 \text{ GeV}$  and a soft part for jets with  $7 < p_T < 20 \text{ GeV}$ . All energies have been calibrated according to the objects they are associated to. The last term in (4.4) has been included to also account for energy deposits in the calorimeter not associated with one of the aforementioned physic objects.<sup>[69]</sup>

### 4.3. Event selection

To extract particular processes from the tremendous amount of data collected at the LHC, different selection criteria have to be applied. The purpose of these criteria is not only to choose events of interest but also to reduce the number of background processes selected.

The process of interest in this study is the all-hadronic decay of a  $t\bar{t}$ -pair. As mentioned, an all-hadronic  $t\bar{t}$ -event is characterised by a total number of six jets, a lack of high energy leptons as well as large  $E_T^{\text{miss}}$ . (cf. sec. 2.2.3)

The first selection criterion for this specific event topology is the ATLAS trigger system. The used trigger chooses only events which have at least five jets with a minimum transverse momentum of 30 GeV.<sup>(13)</sup> To achieve a maximum efficiency of the trigger, the transverse momentum of the first five jets are required to exceed 55 GeV while the  $p_T$  of the sixth jet has to be at least 30 GeV. The events have to contain at least two  $b$ -tagged jets, to account for the expected appearance of  $b$  induced jets in the final state. Apart from that, the primary vertex of the event is required to be associated to at least four tracks, while events affected by noise in the liquid argon calorimeter are rejected to ensure data quality. For the same reason events which contain a reconstructed bad jet<sup>(14)</sup> with positive energy and a  $p_T$  larger than 20 GeV, are discarded.

Besides these selections, additional criteria are applied in order to reject background events. In case of the all-hadronic  $t\bar{t}$ -decay the main indicator for a background process is the presence of a high energetic lepton. Therefore events which contain electrons with  $E_T > 25 \text{ GeV}$  or muons with  $p_T > 25 \text{ GeV}$  are removed.

The use of the observables ‘centrality’ and ‘missing transverse energy significance’ further

<sup>(13)</sup>The particular trigger chosen is EF\_5j30\_a4tc\_EFFS. This trigger reconstructs jets at the event filter level, which are reconstructed from topological clusters by the anti- $k_t$  algorithm with a radius parameter of 0.4. The topological clusters are build from the full calorimeter readout, instead of using information from the regions of interest defined by the level-1 trigger, only.

<sup>(14)</sup>The term bad jet refers to jets which are not associated to real energy deposits in the calorimeter. Such deposits can originate from various sources as for example problems with malfunctioning hardware or from cosmic ray showers.



decrease contributions from QCD multijet production and residual electroweak processes. The centrality in an event is defined as the ratio of transverse energy and total mass. The missing transverse energy significance however is calculated by dividing the  $E_T^{\text{miss}}$  by the scalar sum of the transverse momenta of jets. Events with a centrality smaller than 0.6 or a missing transverse energy significance larger than 3 are rejected.

Moreover, the separation between the two leading  $b$ -tagged jets has to pass a threshold of  $\Delta R > 1.2$ . This is done to exclude events in which a gluon splits up into a  $b\bar{b}$ -pair.

The final selection criteria demands that the event does not contain more than eight jets. The reason for excluding larger jet multiplicities is of physical as well as of computational nature. Since an all-hadronic  $t\bar{t}$ -decay is expected to produce six jets, additional jets in the final state can not originate from the decay itself. These extra jets arise either from initial as well as final state radiation or are associated to the underlying event. Jets induced by initial state radiation or by underlying event processes are independent of the top-decay and should not be considered. In case of final state radiation however, the additional jets are related to the top-quark decay and therefore carry information about the mass of the top-quark. The reconstruction of a top-quark, however, is done with merely six jets, hence the information of the additional jets is lost, this will be explained in the next section.

However, a far more banal reason for restricting the jet multiplicity, is the complexity of the decay reconstruction. The CPU time required to reconstruct a  $t\bar{t}$ -event rises tremendously with an increasing number of jets in the final state. Hence, also from this point of view a restriction on the number of jets in the final state is desired. The question arises why even eight jets are considered and not only six? The answer is that exactly six jets in the final state would severely reduce the available number of  $t\bar{t}$ -events. Since at the energies of the LHC additional jets in the final state are highly probable. A jet multiplicity of eight is therefore a reasonable trade-off between available statistics and physical as well as computational requirements.

The number of signal MC events, which survive the individual selection criteria, are stated in table 4.7. After applying all criteria 32559 events remain. In experimental data, the residual background of the all-hadronic  $t\bar{t}$ -decay is mainly due to QCD multijet production, which is irreducible. This means that the processes are indistinguishable, since their final states contain the same objects as the  $t\bar{t}$ -decay. An example of QCD multijet production is shown in figure 4.6.

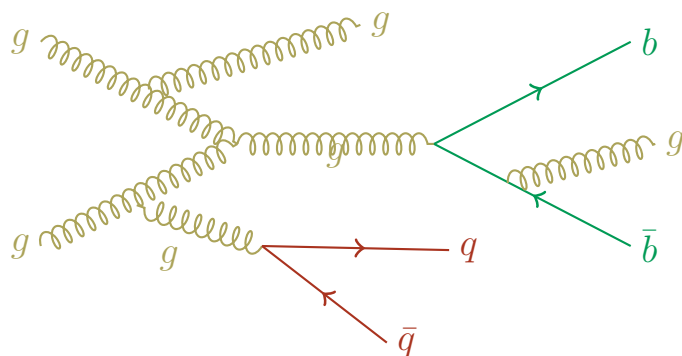
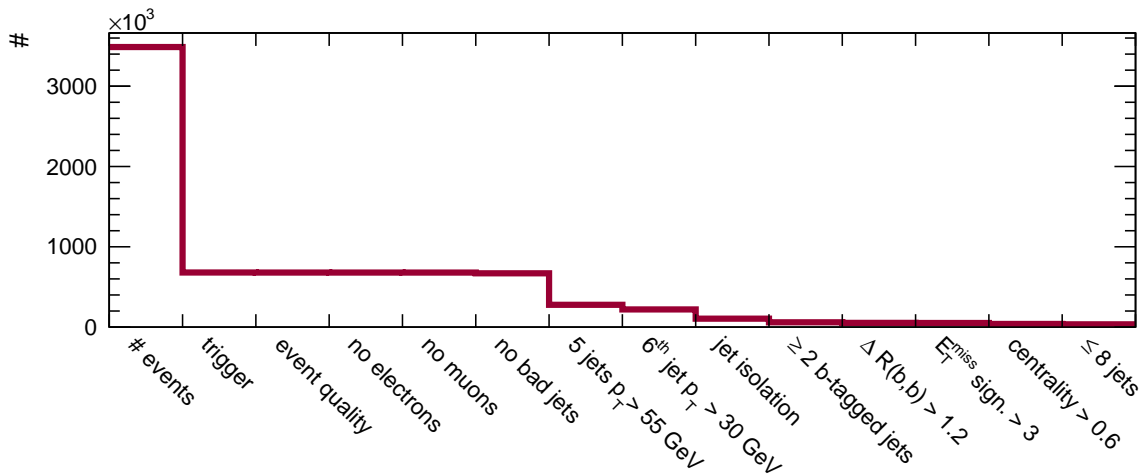
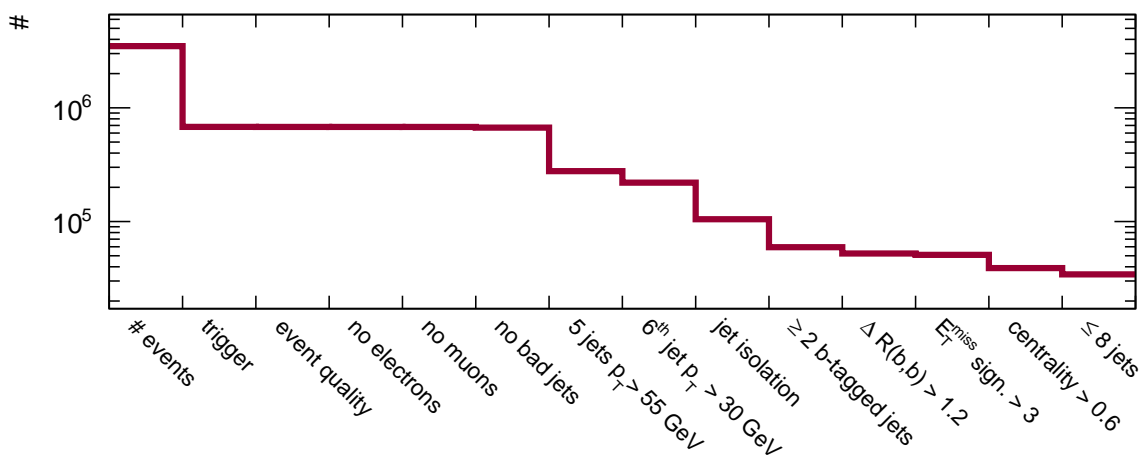


Figure 4.6: Example of QCD multijet production with the same final state signature as an all-hadronic  $t\bar{t}$ -decay



(a) without logarithmic scale



(b) with logarithmic scale

Figure 4.7: Number of events remaining in the signal MC dataset after the individual selection criterion have been applied, without and with logarithmic scale on the y-axis.

#### 4.4. Event reconstruction

One of the main challenges in studying processes involving top-quarks is their reconstruction. A priori, it is not known how to associate an object in the final state to a parton from the  $t\bar{t}$ -decay. Especially in the all-hadronic channel with an event signature consisting of jets only, this is a hard task. In a final state with six jets the number of possible jet-parton assignments is 90. This number arises from subsequently assigning the available jets to the partons of the  $t\bar{t}$ -decay. There are six possibilities to associate a jet to the  $b$ -quark originating from the top-quark decay. Accordingly, there are five jets left which can be assigned to the  $\bar{b}$ -quark. Since the order of partons originating from a W boson decay does not matter for the analysis, the total number of possibilities to associate the remaining four jets to the two W bosons in the event is  $\binom{4}{2} = 6$ . For the same reason, the three jets related to the respective (anti-)top-quark can be exchanged. This reduces the total number of possibilities by a factor of two. Hence, in cases of seven or eight jets in the final state, a total of 630 and 2520 possibilities

have to be considered, respectively. In this analysis the jet-parton assignment and therefore the reconstruction of the  $t\bar{t}$ -system is done with a kinematic likelihood approach, using the KLFitter package<sup>[70]</sup>. The heart of this method is the kinematic likelihood function which in the all-hadronic case reads

$$\begin{aligned} L = & BW\{m_{jj}^1|m_W, \Gamma_W\} \cdot BW\{m_{jj}^2|m_W, \Gamma_W\} \cdot \\ & BW\{m_{jjj}^1|m_{top}, \Gamma_{top}\} \cdot BW\{m_{jjj}^2|m_{top}, \Gamma_{top}\} \cdot \\ & \prod_{i=1}^4 W\left(\tilde{E}_{jet_i}|E_{q_i}\right) \cdot \prod_{j=1}^2 W\left(\tilde{E}_{jet_j}|E_{b_j}\right) \end{aligned} \quad (4.5)$$

where  $m_{jj}^i$  and  $m_{jjj}^i$  denote the invariant masses of the objects, representing the reconstructed W bosons and top-quarks. For each jet in the  $t\bar{t}$ -final state, the likelihood incorporates a transfer function  $W$ . The transfer functions are split up into two sets, accounting for light as well as  $b$ -tagged jets. The purpose of these functions is to correct for physics as well as detector effects. This is done by mapping the measured energies of jets, referred to as  $\tilde{E}$ , back to the original parton values  $E$ . In the likelihood the terms  $BW$  represent modified relativistic Breit-Wigner distributions. They account for the natural decay widths of the top-quark and W boson. These distributions are given by

$$BW(x|m, \Gamma) = \frac{1}{(x^2 - m^2)^2 + \Gamma^2 m^2} \quad (4.6)$$

where  $m$  is the mass of a particle and  $\Gamma$  denotes its decay width. In this analysis, the W boson mass is fixed to 80.4 GeV, while its width is set to 2.1 GeV. The top-mass, however, is a free fit parameter and its width is adjusted accordingly<sup>(15)</sup>. Furthermore, CPT symmetry is assumed, which means that, the masses of particles and their corresponding anti-particles are equal.

The reconstruction of the  $t\bar{t}$ -system is done by building all possible combinations of affiliating jets in an event to the six final state partons. For each permutation the KLFitter maximises the likelihood function by varying the energies within a range of<sup>(16)</sup>

$$\min\left(0, \tilde{E} - 7 \cdot \sqrt{\tilde{E}}\right) < E < \tilde{E} + 7 \cdot \sqrt{\tilde{E}}$$

For each permutation the fit parameters and the value of the likelihood function is returned. By construction the permutation, which corresponds to the smallest likelihood value<sup>(17)</sup>, is the one, which agrees best with the  $t\bar{t}$ -decay hypothesis. The top-and antitop-quark are reconstructed according to the jet-parton assignment of this permutation. This is done by adding the four-momenta of the jets associated to the particular partons. Figure 4.8 shows the likelihood values for the permutations, chosen to reconstruct the  $t\bar{t}$ -system.

To decrease the huge amount of permutations an additional reconstruction criteria is introduced. For that purpose, all combinations in which a non  $b$ -tagged jet is placed in the position of a  $b$ -quark of the  $t\bar{t}$ -decay are rejected. This reduces the total number of jet-parton assignments per event to 6, 30 and 90 for a final state consisting of six, seven and eight jets, respectively.

<sup>(15)</sup>A discussion of the top-quark width can be found in ‘Review of Particle Physics’ (p. 669)<sup>[8]</sup>

<sup>(16)</sup>This particular range is motivated by the detector resolution and is chosen in accordance with reference<sup>[70]</sup>.

<sup>(17)</sup>for computational reasons it is more reasonable to minimise  $-\ln L$  instead of maximising  $L$

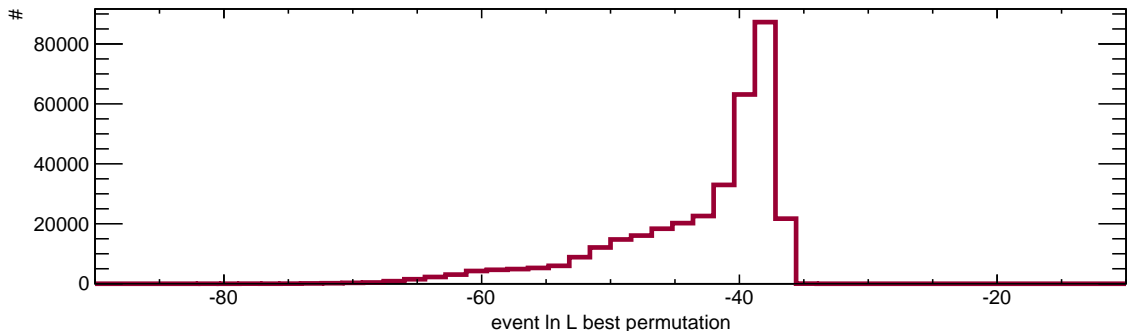


Figure 4.8: The  $\ln L$  values of the best permutations obtained from the MC signal sample

## 4.5. The top-quark mass

One way to determine the mass of the top-quark<sup>(18)</sup> is to use its reconstructed four-momentum. According to the relativistic energy-momentum relation the mass of a particle is related to its energy and momentum by

$$m = \sqrt{E^2 - \mathbf{p}^2} \quad (4.7)$$

In this approach  $m_{\text{top}}$  equals the invariant mass of the three jet system  $m_{jjj}$ , built by the jets associated to the top-quark. The notation  $m_{jjj}$  emphasises the fact, that the particular permutation, chosen by the kinematic likelihood fit, does not necessarily represent the original top-quark. On the one hand the jet-parton assignment could be wrong, which is referred to as combinatorial background, or on the other hand, the particular event could be physical background, not related to a top-quark at all. The distributions of  $m_{jjj}$  are shown for three generated top-quark masses in figure 4.9.

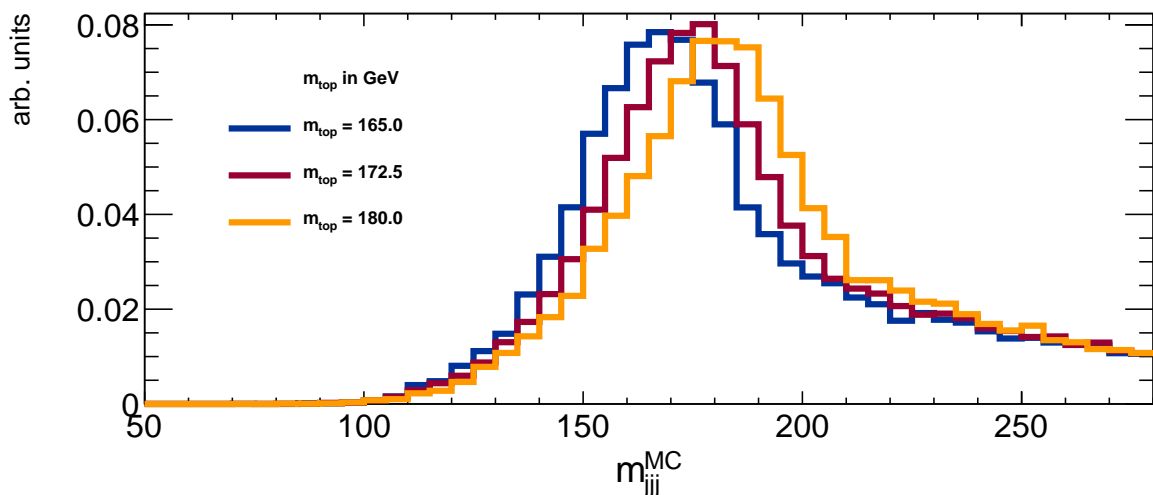


Figure 4.9: Distribution of  $m_{jjj}$  for input top-quark mass of 165 GeV, 172.5 GeV and 180 GeV

As expected, the  $m_{jjj}$  distribution shifts to higher masses as the value for the input top-quark mass is increased.

Obviously, opposed to the assumption of the kinematic likelihood approach, the obtained

<sup>(18)</sup>In the following the top-quark as well as the anti-top-quark are referred to as top-quark

distributions do not look like Breit-Wigner distributions (cf. app. B). One reason is, that the energies and momenta of the original jets smear out, due to the detector simulation. This results in a broadening of distributions related to jet four-momenta, like  $m_{jj}$ . The shoulder starting at about 200 GeV, however, originates from permutations in which the likelihood fitter has not returned the right combination of jet-parton assignments. This results in a shift of the mean of the  $m_{jj}$  distribution towards higher masses.

As shown before, the top-quark is severely influenced by the jet energy scale uncertainty (cf. sec. 4), especially in the all-hadronic channel. Since this uncertainty is not included in the used MC sample, it is artificially introduced by multiplying the reconstructed jet four momenta with a so called jet scale factor. As the error on the jet energy scale, the jet scale factor also is split. It is differentiated between a term accounting for light-jets and a term allowing for  $b$ -jets, referred to as lJSF and bJSF. These factors are varied in 5 % steps from 0.9 to 1.1, to reproduce the effects of different jet energy scale uncertainties. The resulting four-momenta of reconstructed jets are given by

$$\begin{aligned} p_{light} &= p_{light}^{measured} \cdot \text{lJSF} \\ p_b &= p_b^{measured} \cdot \text{lJSF} \cdot \text{bJSF} \end{aligned} \quad (4.8)$$

where the lJSF is applied to both types of jets, while the bJSF is only utilised on  $b$ -tagged jets. The influence of the jet scale factors on the invariant mass of the reconstructed W bosons  $m_{jj}$  are shown in figure 4.10.

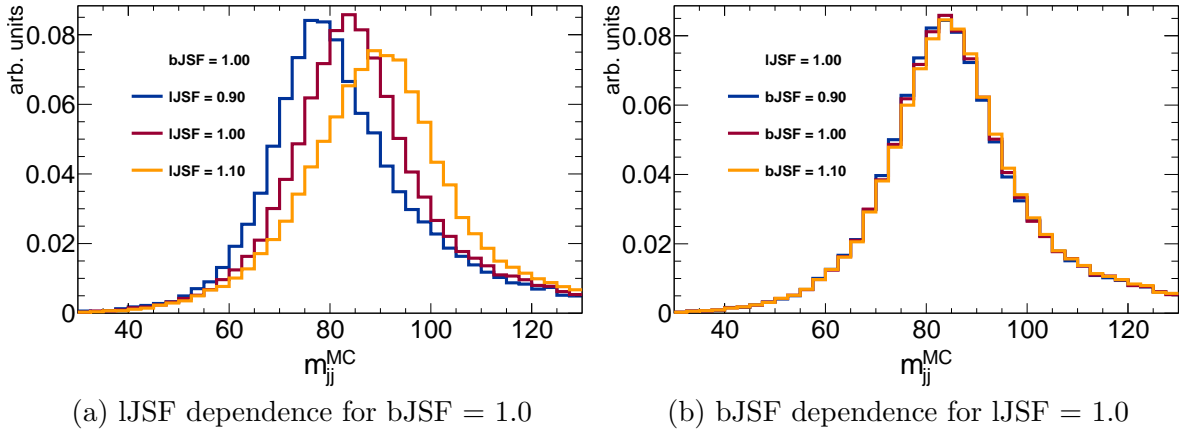


Figure 4.10: Influence of the jet scale factors lJSF and bJSF on  $m_{jj}$

The variation of lJSF has a considerable influence on the reconstructed mass of the W boson. Since the light-jet scale factor linearly modifies the jet energies, an increase of lJSF leads to a shift in the corresponding distributions of  $m_{jj}$  to larger values. The linear implementation also results in a broadening of the  $m_{jj}$  distribution for growing lJSF, because large values of  $m_{jj}$  experience a larger variation than small values.

In contrast to the light-jet scale factor, the bJSF barely influences the  $m_{jj}$  distribution. This behaviour is expected, since the hadronic W boson decay involves only light-jets<sup>(19)</sup>, while the bJSF is solely applied to  $b$ -tagged jets. The small dependence on  $m_{jj}$  is therefore introduced either due to a wrongly  $b$ -tagged light-jet, or a correctly  $b$ -tagged jet, which has been wrongly assigned to the W boson decay. Despite this small influence, the reconstructed W boson mass

<sup>(19)</sup>There is also the possibility of a W boson decaying into a top and  $b$ -quark. However, because of the high mass of the top-quark this process is very unlikely.

is in good approximation independent of the bJSF.

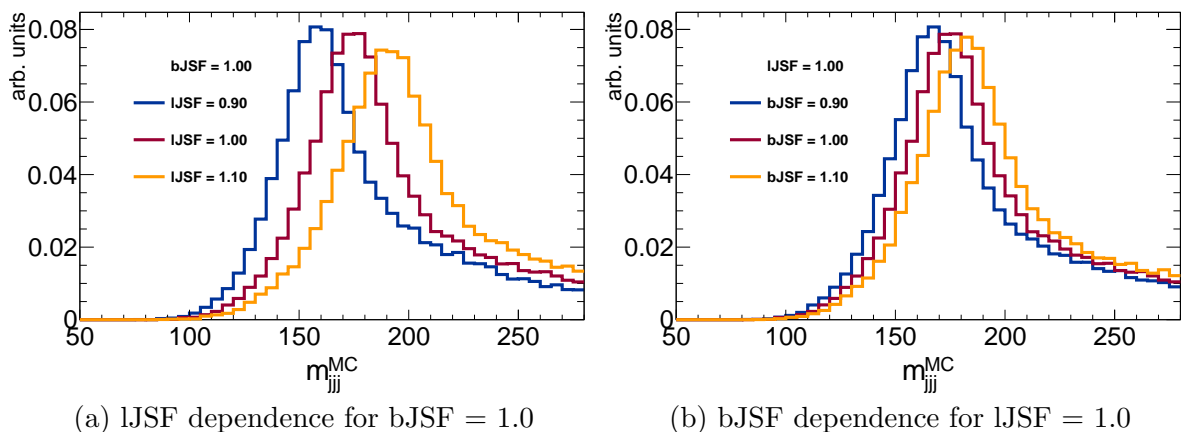


Figure 4.11: Influence of the jet scale factors LJSF and bJSF on  $m_{jjj}$

Similar to these plots, figure 4.11 shows the dependence of  $m_{jjj}$  on both jet scale factors. Again, the reconstructed top-quark mass is highly influenced by the LJSF, due to the linear implementation of the scale factor. But in contrast to the reconstructed W boson mass,  $m_{jjj}$  is also dependent on the  $b$ -jet scale factor, since the top-quark is reconstructed by explicitly asking for a  $b$ -tagged jet. Except for the two aforementioned cases of wrong tagging or assignment, the top-quark is build exactly from one  $b$ -tagged jet and two light-jets. In case of the  $t\bar{t}$ -decay, these jets carry on average similar momenta (cf. fig. D.1). Considering that the bJSF solely influences  $b$ -tagged jets, while the LJSF applies to light as well as  $b$ -tagged jets, the impact of the latter one on  $m_{jjj}$  predominates. If either the LJSF or the bJSF is varied as done for the plots in figure 4.11, the dependence of  $m_{jjj}$  is roughly twice as large for LJSF as for bJSF.

## 4.6. The $R_{23}$ and $R_{32}$ estimators

Since  $m_{jjj}$  is severely influenced by the jet energy scale uncertainties, another estimator is chosen to determine the top-quark mass. The estimators investigated in this analysis are  $R_{23}$  and  $R_{32}$ . They are defined as ratios of the invariant mass of the three jet system, representing the reconstructed top-quark and the invariant mass of the reconstructed W boson and read

$$R_{23} \equiv \frac{m_{\text{W}}^{\text{rec}}}{m_{\text{top}}^{\text{rec}}} = \frac{m_{jj}}{m_{jjj}} \quad R_{32} \equiv \frac{m_{\text{top}}^{\text{rec}}}{m_{\text{W}}^{\text{rec}}} = \frac{m_{jjj}}{m_{jj}} \quad (4.9)$$

The two estimators are chosen to be inverse to each other and are built for each event. The main idea in choosing the ratio of these two quantities is, that common uncertainties in both,  $m_{jjj}$  and  $m_{jj}$ , cancel out. Especially the impact of global jet scale factors, like LJSF, is reduced. The main difference of the two estimators is the range of possible values. Since  $m_{jjj}$  is always larger than  $m_{jj}$ , it follows that

$$0 < R_{23} < 1 \quad \text{while} \quad 1 < R_{32} < \infty$$

This results in a more symmetric distribution for  $R_{23}$  than for  $R_{32}$ . Since, the use of  $R_{23}$  yields a smaller bias in the top-mass measurement than the usage of  $R_{32}$  (cf sec. 4.9.2 and

app. A.2), in the following, only the estimator  $R_{23}$  is reviewed. The corresponding discussion of  $R_{32}$  can be found in appendix A.

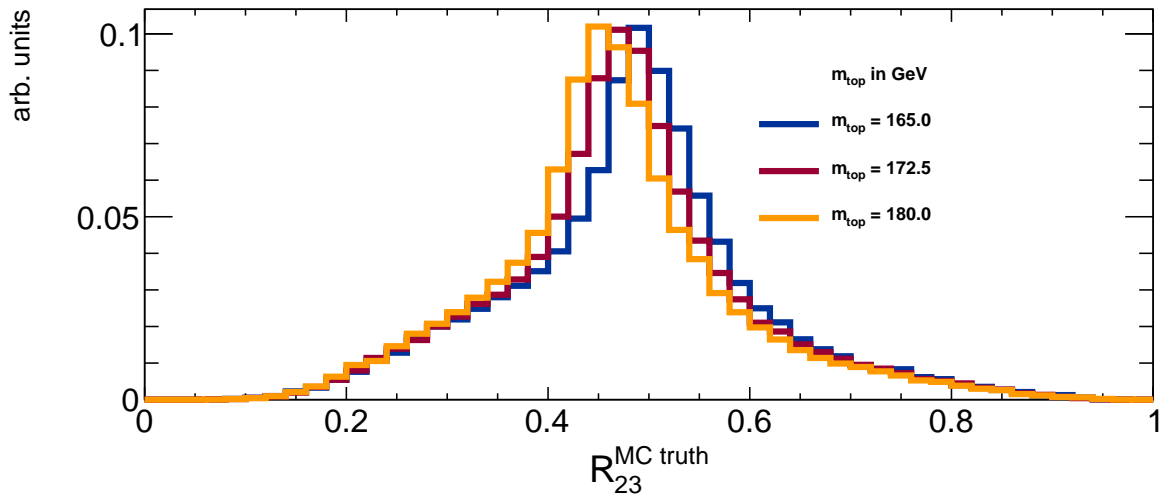


Figure 4.12: Distribution of  $R_{23}$  for input top-quark mass of 165 GeV, 172.5 GeV and 180 GeV

The distribution of  $R_{23}$  for a varied MC input top-quark mass is presented in figure 4.12. According to this, a variation of the simulated top-quark mass shifts the distribution of  $R_{23}$ . However, in contrast to  $m_{jjj}$ , the values of  $R_{23}$  become smaller for an increasing top-quark mass. This is expected since the input top-quark mass of the MC sample is not related to the W boson mass<sup>(20)</sup>. Therefore the numerator remains constant, while the denominator of equation (4.9) changes. Aside from the influence of  $m_{\text{top}}$ , figure 4.12 also reveals the contribution of the combinatorial background, which results in an enhanced left flank of the  $R_{23}$  distribution.

By construction, the dependence of  $R_{23}$  on the light jet scale factor is reduced, which results in an only slight variation of the distribution for different lJSF values. However, there is still an influence of the bJSF on the  $R_{23}$  distribution. Similar to  $m_{jjj}$  (fig. 4.11b),  $R_{23}$  is shifted for a varied  $b$ -jet scale factor.

The main reason for introducing  $R_{23}$  is its reduced dependence on the jet energy scale. Figure 4.13 shows the according distributions for different values of lJSF and bJSF. By construction, the dependence of  $R_{23}$  on the light jet scale factor is reduced, which results in an only slight variation of the distribution for different lJSF values. However, there is still an influence of the bJSF on the  $R_{23}$  distribution. Similar to  $m_{jjj}$  (fig. 4.11b),  $R_{23}$  is shifted for a varied  $b$ -jet scale factor.

This behaviour is problematic, since it perturbs the determination of  $m_{\text{top}}$ . As is explained in section 4.9 the extraction of the underlying top-quark mass is done by fitting the shape of the estimator distribution. Moreover, the measured  $m_{\text{top}}$  is particularly sensitive to the peak value of this distribution. Considering that a change in the underlying top-mass as well as a variation of the bJSF have the same influence on the estimator, namely a shift in the corresponding distribution, these two effects are indistinguishable. With an experimental uncertainty on the  $b$ -jet energy scale of up to 6 % (cf. fig. 4.5b), a measurement of  $m_{\text{top}}$  with

<sup>(20)</sup>Actually, there is an implicit dependence of the W boson on the real  $m_{\text{top}}$ , introduced by radiative loop corrections. Since however, the experimental verified mass of the W boson is used in the MC samples, this dependence is already naturally accounted for. Varying the input top-quark mass in the MC datasets has therefore no influence on  $m_W$ .

$R_{23}$  on its own will always be considerably influenced by the bJSF. In this analysis a second estimator, especially designed to determine the bJSF, is introduced. This estimator explicitly allows to account for the influence of bJSF on the  $R_{23}$  distribution and will be discussed in the next section.

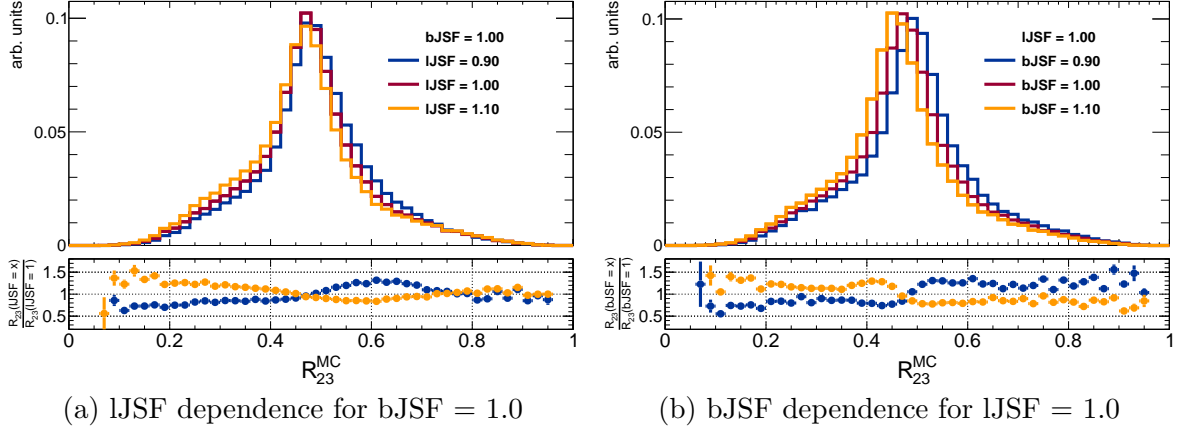


Figure 4.13: Influence of the jet scale factors lJSF and bJSF on  $R_{23}$

## 4.7. The $R_{bl}$ estimator

To enable a precise determination of the  $b$ -jet scale factor, an estimator has to fulfil two criteria. It has to depend on bJSF and be immune to influences other than that. Especially it should be as insensitive to the top-quark mass as possible. The estimator chosen for this task is  $R_{bl}$ , which is shown in figure 4.14.

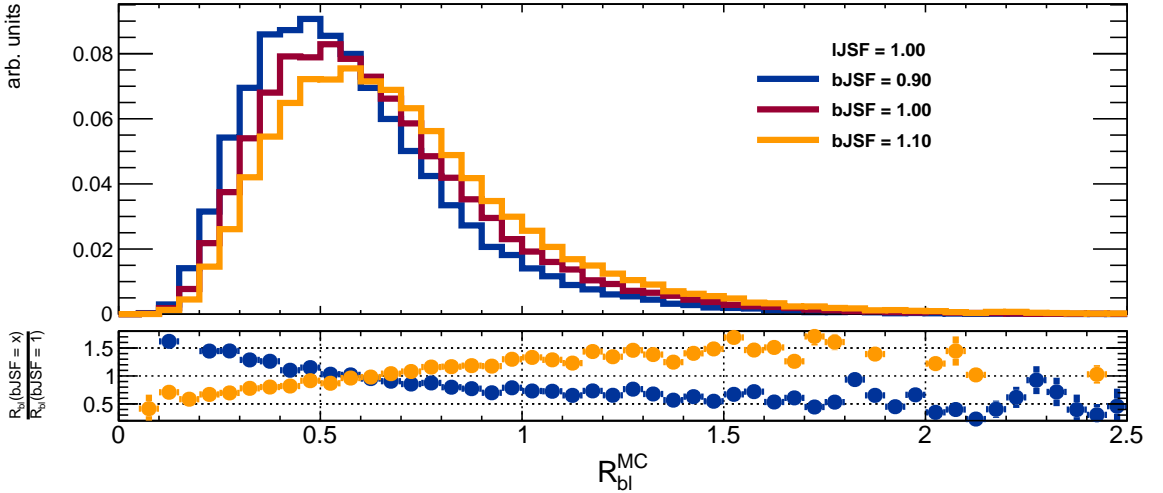


Figure 4.14: Dependence of  $R_{bl}$  on bJSF for a fixed lJSF

It is constructed by dividing the sum of the absolute values of the jet- $p_T$ , assigned to  $b$ -quarks of the  $t\bar{t}$ -decay by the sum of transverse momenta of the light jets associated to the  $W$  bosons, thus exploiting the knowledge about the jet-parton assignment in a  $t\bar{t}$ -event. Hence  $R_{bl}$  is given by<sup>[48]</sup>



$$R_{bl} = \frac{\sum p_T^b}{\sum p_T^{\text{light}}} \quad (4.10)$$

Since the reconstruction particularly demands a  $b$ -tagged jet in the position of a  $b$ -quark of the top-quark decay  $R_{bl}$  is sensitive to the  $b$ -jet scale factor. By construction the dependence on IJSF should vanish. The influences of the light as well as the  $b$ -jet scale factor are shown in figure 4.15.

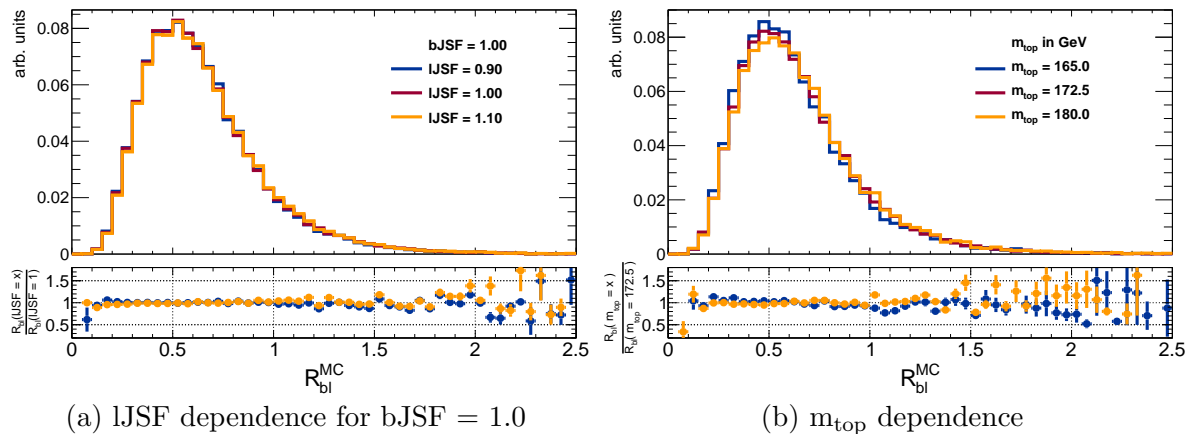


Figure 4.15: Influence of the IJSF and  $m_{\text{top}}$  on  $R_{bl}$

However there is a minor dependence on IJSF according to figure 4.15a. Since the correction of the jet energy scale is done before the kinematic reconstruction, the jet-parton assignment can be alternated. Therefore, the IJSF can slightly influence the  $R_{23}$  distribution. Besides, figure 4.15b reveals a minor dependence of  $R_{bl}$  on the top-quark mass, which results in a slightly shifted distribution. This dependence of the estimator on  $m_{\text{top}}$  will be specifically considered in the analysis.

The main feature of  $R_{bl}$  clearly is its dependence on the  $b$ -jet scale factor, as can be seen in figure 4.14. This allows the use of  $R_{bl}$  for an explicit determination of bJSF from experimental data.

## 4.8. Parametrisation of $R_{23}$ and $R_{bl}$

As mentioned previously, the determination of the top-quark mass relies on a proper description of the estimator distributions. An accurate parametrisation of  $R_{23}$  and  $R_{bl}$  is therefore crucial.

The agreement of a parametrisation with an underlying distribution can be expressed in terms of the goodness of fit value which is given by  $\chi^2/\text{ndf}$ . The number of degrees of freedom, ndf, is calculated as the number of bins considered in the fit subtracted by the total number of fitting parameters. Furthermore, the weighted sum of squared errors is defined by

$$\chi^2 = \sum_i^{\text{bins}} \frac{(y_i - f(x_i))^2}{\sigma_i^2} \quad (4.11)$$

where  $y_i$  is the number of events in bin  $i$ ,  $f(x_i)$  is the expected number of events in this bin and  $\sigma_i$  denotes its statistical error. In the context of hypothesis tests it can be shown, that a distribution is well described by a parametrisation, if  $\chi^2/\text{ndf} \approx 1$  [8].

The parametrisation of the  $R_{23}$  distribution is done with the sum of a Landau and a Breit-Wigner function, while the  $R_{bl}$  distribution is parametrised by a Novosibirsk function. The parameters describing these functions are listed below, while their impact on the particular distributions can be found in appendix B.

- |                                     |   |  |
|-------------------------------------|---|--|
| • Landau function<br>(cf. eqn. B.1) | • Breit-Wigner function<br>(cf. eqn. B.2) | • Novosibirsk function<br>(cf. eqn. B.4) |
| – normalisation                     | – normalisation                           | – normalisation                          |
| – most probable value               | – mean                                    | – mean                                   |
| – scale parameter                   | – width                                   | – width                                  |
|                                     |   | – tail parameter                         |

The ranges of the distributions are restricted in order to ensure a good fit result. For the  $R_{23}$  distributions the fit considers values from 0.2 up to 0.7, corresponding to top-quark masses of 115 GeV and 400 GeV, while the parametrisation of  $R_{bl}$  ranges from 0.2 up to 0.7. The parametrisations of the  $R_{23}$  and  $R_{bl}$  distributions are shown in figure 4.16. For  $R_{23}$  the contributions of the individual Landau and Breit-Wigner function is indicated.

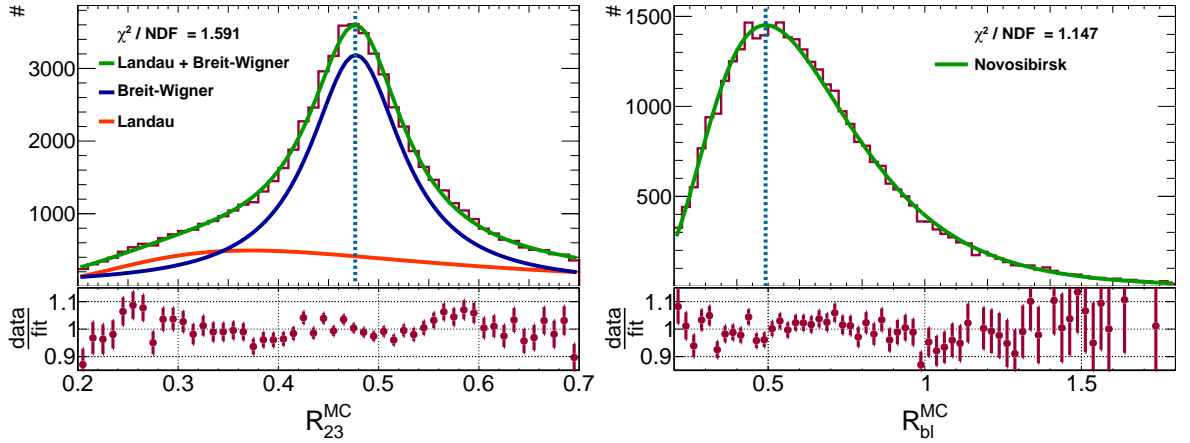


Figure 4.16: Parametrisation of  $R_{23}$  and  $R_{bl}$  shown in green. In case of the  $R_{23}$  distribution the Landau function is marked in orange, while the Breit-Wigner function is drawn in blue. Additionally the maximum is indicated.

The distributions are well parametrised by the corresponding fitted functions. The fitting yields a goodness of fit value of  $\chi^2/\text{ndf} = 1.591$  for  $R_{23}$  and  $\chi^2/\text{ndf} = 1.147$  for  $R_{bl}$ . Firstly it is worth to mention, that the combinatorial background, which is present in  $R_{23}$ , is correctly accounted for by the Landau function, while the peak, which is sensitive to  $m_{\text{top}}$ , is well described by the Breit-Wigner function. And secondly, one analytical function alone is suitable to characterise the  $R_{bl}$  distribution.

In conclusion, the chosen parametrisation is well suited to describe the  $R_{23}$  and  $R_{bl}$  distributions and can therefore be used to determine  $m_{\text{top}}$  as well as bJSF.

## 4.9. The template method

The approach used to determine the top-quark mass is referred to as template method. This technique uses the known shapes of the estimator distributions obtained from MC simulations. Thereby changes of these distributions, due to variations in the implemented values of  $m_{\text{top}}$  and bJSF, can be parametrised. The knowledge of this parametrisation enables the extraction of the true values of  $m_{\text{top}}$  and bJSF from estimator distributions measured in experiment.

### 4.9.1. Construction of templates

For all seven MC mass variation samples (cf. tab. 4.1), the bJSF is varied from 0.9 to 1.1 in 5% steps. The resulting distributions for both estimators are parametrised, according to the functions described in section 4.8. These parametrisations are shown in figures 4.19 and 4.20 for all combinations of  $m_{\text{top}}$  and bJSF. In these figures, distributions arranged in columns correspond to a constant value of bJSF, with an increasing  $m_{\text{top}}$  from top to bottom. Furthermore, distributions aligned in rows represent an increasing bJSF for a constant  $m_{\text{top}}$ . As can be seen in these plots, the parametrisations are suitable to describe the  $R_{23}$  as well as the  $R_{\text{bl}}$  distributions for all values of  $m_{\text{top}}$  and bJSF.

The parametrisation returns a total number of ten parameters for each combination of  $m_{\text{top}}$  and bJSF. Six of them describe the parametrisation of  $R_{23}$  while the other four correspond to the  $R_{\text{bl}}$  description. Each of the ten parameters is separately drawn versus the corresponding input value of  $m_{\text{top}}$  and bJSF. According to their dependence, the resulting parameter plots are split into two parts. In the first, the parameters are plotted as a function of  $m_{\text{top}}$ , while bJSF is fixed. Since there are several bJSF, this is repeated for every particular value. In the second part, the parameters are plotted as a function of bJSF, while now  $m_{\text{top}}$  is constant. Again, this is done for all seven values of  $m_{\text{top}}$ . Consequently, this results in a total of twelve sets of parameter distributions, which can be found in appendix C. In figures 4.21 and 4.22 two of these sets are shown. The first set represents the parameter dependence on  $m_{\text{top}}$  for bJSF = 1 and corresponds to the third column in figures 4.19 and 4.20. The second set is equivalent to the fourth row in these plots and illustrates the influence of bJSF for a constant  $m_{\text{top}}$  of 172.5 GeV.

For each of the parameters a linear dependence on either  $m_{\text{top}}$  or bJSF is assumed. The parametrisation parameters  $p_i$  can therefore be written either as

$$p_i = a_i^{m_{\text{top}}} + b_i^{m_{\text{top}}} \cdot m_{\text{top}} \quad (4.12)$$

if the input top-quark mass has been varied, or

$$p_i = c_i^{\text{bJSF}} + d_i^{\text{bJSF}} \cdot \text{bJSF} \quad (4.13)$$

for a change of bJSF. Each of the parameter distributions are fitted according to these linear assumptions. The results of these fits are also included in figures 4.21 and 4.22.

However, the assumption of a linear dependence of  $p_i$  on  $m_{\text{top}}$  and bJSF has to be verified. Therefore, a simultaneous fit of all available estimator distributions is done. In this combined fit the parameters  $p_i$  are not allowed to vary freely anymore, instead they are parametrised by a linear combination of  $m_{\text{top}}$  as well as bJSF, with

$$p_i = a_i + b_i \cdot m_{\text{top}} + c_i \cdot \text{bJSF} \quad (4.14)$$

The parameters  $a_i$ ,  $b_i$  and  $c_i$  are determined by explicitly using the known values of  $m_{\text{top}}$  and bJSF in the particular estimator distributions. These fit results are also shown in figures 4.21 and 4.22. The corresponding parameter values of the individual and combined fits are given in tables C.3 and C.2.

Overall, except for some minor deviations, which are covered by the corresponding uncertainties, the separated and combined fits are in agreement with each other. What can be seen in figure 4.21 is on the one hand a small dependence of  $R_{\text{bl}}$  on  $m_{\text{top}}$  and on the other hand the high sensitivity of the  $R_{23}$  parametrisation on  $m_{\text{top}}$ , particularly the mean parameter of the Breit-Wigner function. Similar arguments hold for the parameter distributions in figure 4.22. Again, the dependence of bJSF on the  $R_{23}$  parameters emerges, while the  $R_{\text{bl}}$  distributions reveals the behaviour it was constructed for, a high sensitivity on bJSF.<sup>(21)</sup>

Therefore two conclusions are possible: First, the assumption of a linear dependence of the parametrisation parameters  $p_i$  is valid and second, the parametrisation of  $R_{23}$  and  $R_{\text{bl}}$  is capable of determining  $m_{\text{top}}$  as well as bJSF from experimental data.

The final measurement of the top-quark mass is done by a binned likelihood fit. The likelihood function consists of two terms, one accounting for  $R_{23}$  and one considering  $R_{\text{bl}}$ . It is given by

$$L(R_{23}, R_{\text{bl}}|m_{\text{top}}, \text{bJSF}) = L_{R_{23}}(R_{23}|m_{\text{top}}, \text{bJSF}) \cdot L_{R_{\text{bl}}}(R_{\text{bl}}|m_{\text{top}}, \text{bJSF}) \quad (4.15)$$

For each bin a Poissonian distribution of the number of observed events  $N_{\text{obs},j}$  is assumed. The individual likelihood functions  $L_{R_{23}}$  and  $L_{R_{\text{bl}}}$  therefore can be written as

$$L_{R_{23}/R_{\text{bl}}}(R_{23}/R_{\text{bl}}|m_{\text{top}}, \text{bJSF}) = \prod_j^{\text{bins}} \left( \frac{\lambda_j^{N_{\text{obs},j}}}{N_{\text{obs},j}!} \right) \cdot \exp(-\lambda_j) \quad (4.16)$$

where  $\lambda_j$  denotes the number of expected events in bin  $j$ . This number is derived from the particular parametrisation of the estimator. In case of  $L_{R_{23}}$  this is the sum of the Landau and Breit-Wigner function, where in the case of  $L_{R_{\text{bl}}}$  it is given by the Novosibirsk parametrisation. In this calculation, the parameter values derived from the separate fits:  $a_i^{m_{\text{top}}}$ ,  $b_i^{m_{\text{top}}}$ ,  $c_i^{\text{bJSF}}$  and  $b_i^{\text{bJSF}}$  are used. This means, that the only parameters in this likelihood fit are the unknown values of  $m_{\text{top}}$  and bJSF.

The operational capability of the template method is validated with the signal MC dataset. The resulting estimator distributions for bJSF = 1 are shown in figure 4.17. Moreover, figure 4.18 presents the obtained top-quark masses for the five different values of bJSF.

The three central values in figure 4.18 agree within their errors with the simulated value of  $m_{\text{top}}$ . However, the deviation between  $m_{\text{top}}^{\text{fit}}$  and  $m_{\text{top}}$  for bJSF = 1.1 and bJSF = 0.9 exceed the corresponding errors. While for the first this aberration is very small, the deviation for the latter corresponds to about two and half times its error.

<sup>(21)</sup>As can be seen, the individual parameters of the Landau and Breit-Wigner functions are highly correlated. The corresponding values are given in table C.1.

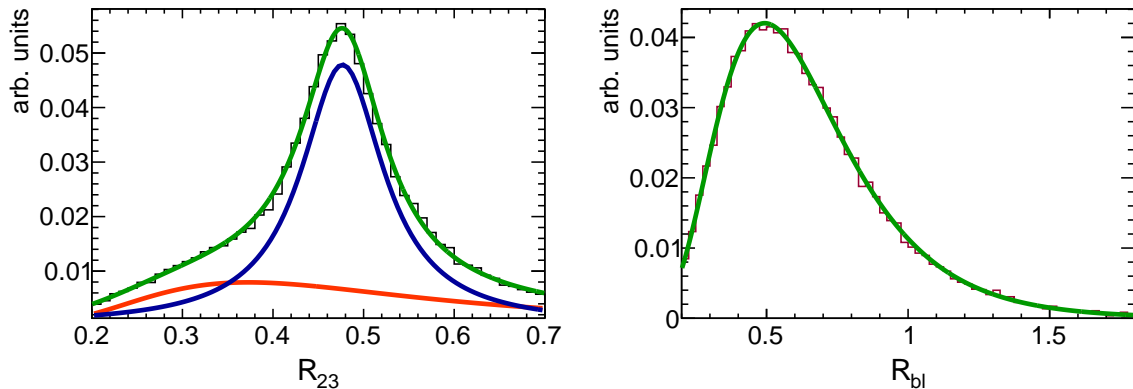


Figure 4.17: Estimator distributions for a binned likelihood fit of the signal MC with bJSF=1. The likelihood yields  $m_{\text{top}} = 172.29 \pm 0.31$  GeV and bJSF =  $1.007 \pm 0.03$ .

However, all fitted values of  $m_{\text{top}}$  tend to underestimate the top-quark mass. This could be a hint, that the analysis causes a bias in the measurement, resulting in shifted values for  $m_{\text{top}}^{\text{fit}}$ . In particular, this could be responsible for the large deviation in case of bJSF = 0.9. An approach to check for such a bias is presented in the next section.

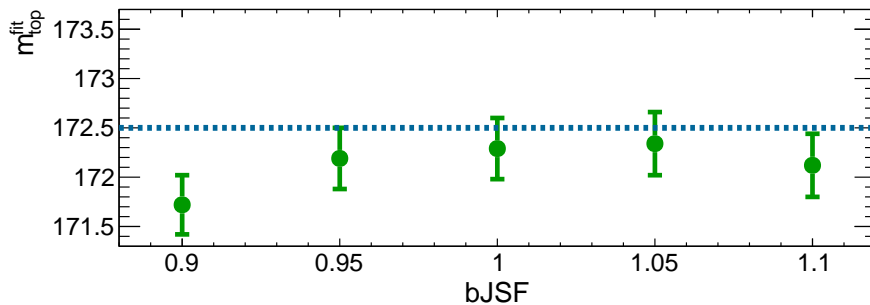


Figure 4.18: Result of the binned likelihood fit, for different input values of bJSF. The fitted values for  $m_{\text{top}}$  with the corresponding fit uncertainty are shown in green. Indicated in blue is the simulated top-quark mass of the used signal MC sample

#### 4.9.2. Check method for bias

In this analysis pseudo-experiments are used to conclude, whether the underestimation of  $m_{\text{top}}$  is just a statistical fluctuation or indicates a bias in the measurement. The pseudo-experiment in this analysis are constructed by randomly drawing as many values from the  $R_{23}$  distribution as events are expected in real data. These values are treated as the results of a pseudo-measurement. The number of expected events can be calculated with

$$N_{\text{exp}} = \frac{N_{\text{MC}} \cdot \sigma_{t\bar{t}} \cdot \text{k-factor} \cdot \int L dt}{N_{\text{MC}}^{\text{total}}} \quad (4.17)$$

In case of the mass variation sample with  $m_{\text{top}} = 172.5$  GeV, the number of expected events in 2011 LHC data is 3617. Thus, each pseudo-experiment corresponds to a  $R_{23}$  like distribution, with a total number of events of pseudo-events, which is poisson distributed around  $N_{\text{exp}}$ .

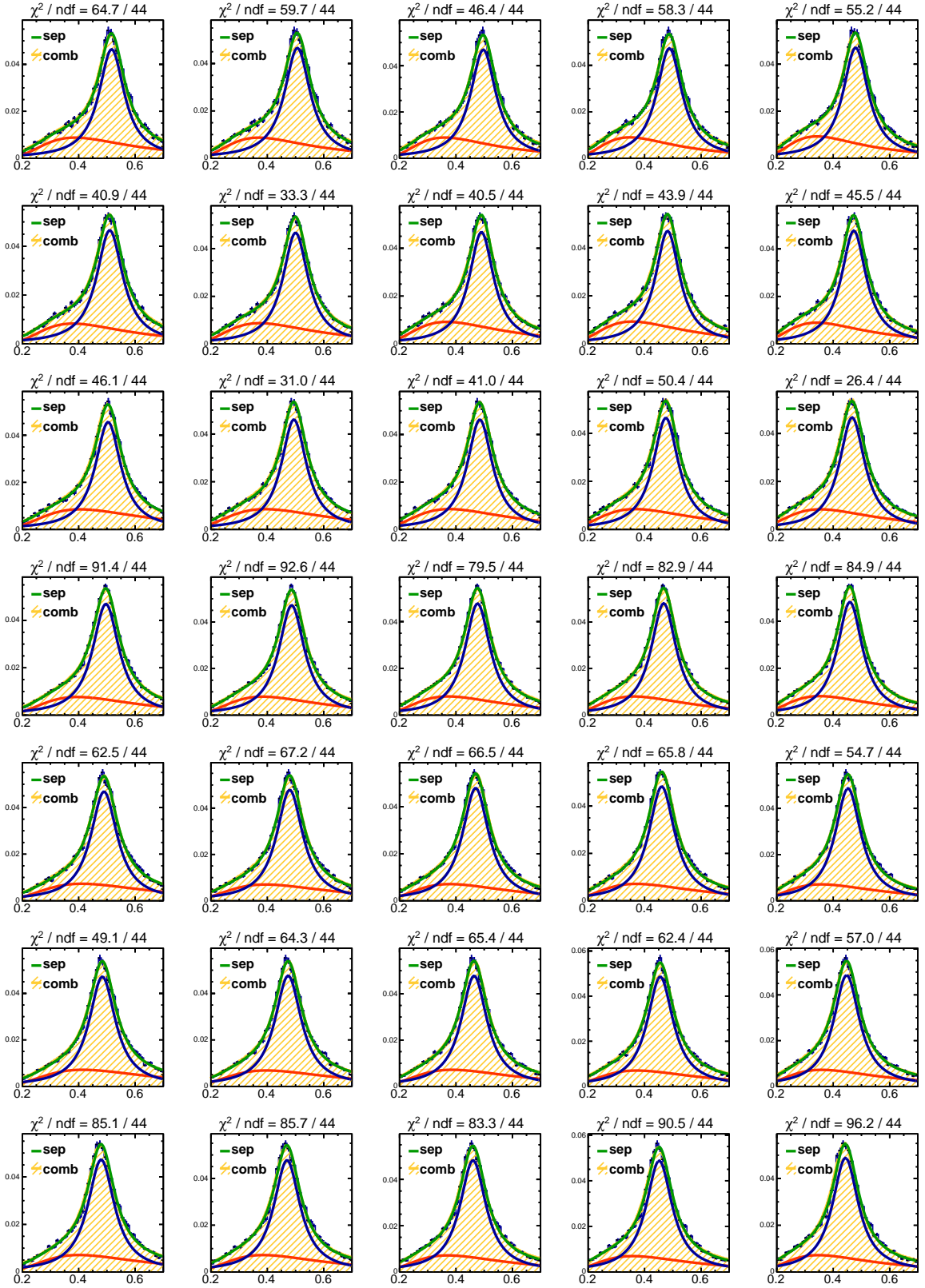


Figure 4.19: Distributions of  $R_{23}$  for all seven mass variation samples and five values of  $b_{JSF}$ . The individual fit is shown in green while the combined fit is indicated in yellow. The goodness of fit values stated correspond to the individual fits. The distributions arranged in one line correspond to the same masspoint, but differ in their value of  $b_{JSF}$ , while distributions assembled in a column belong to the same  $b_{JSF}$  but differ in the  $m_{top}$ .

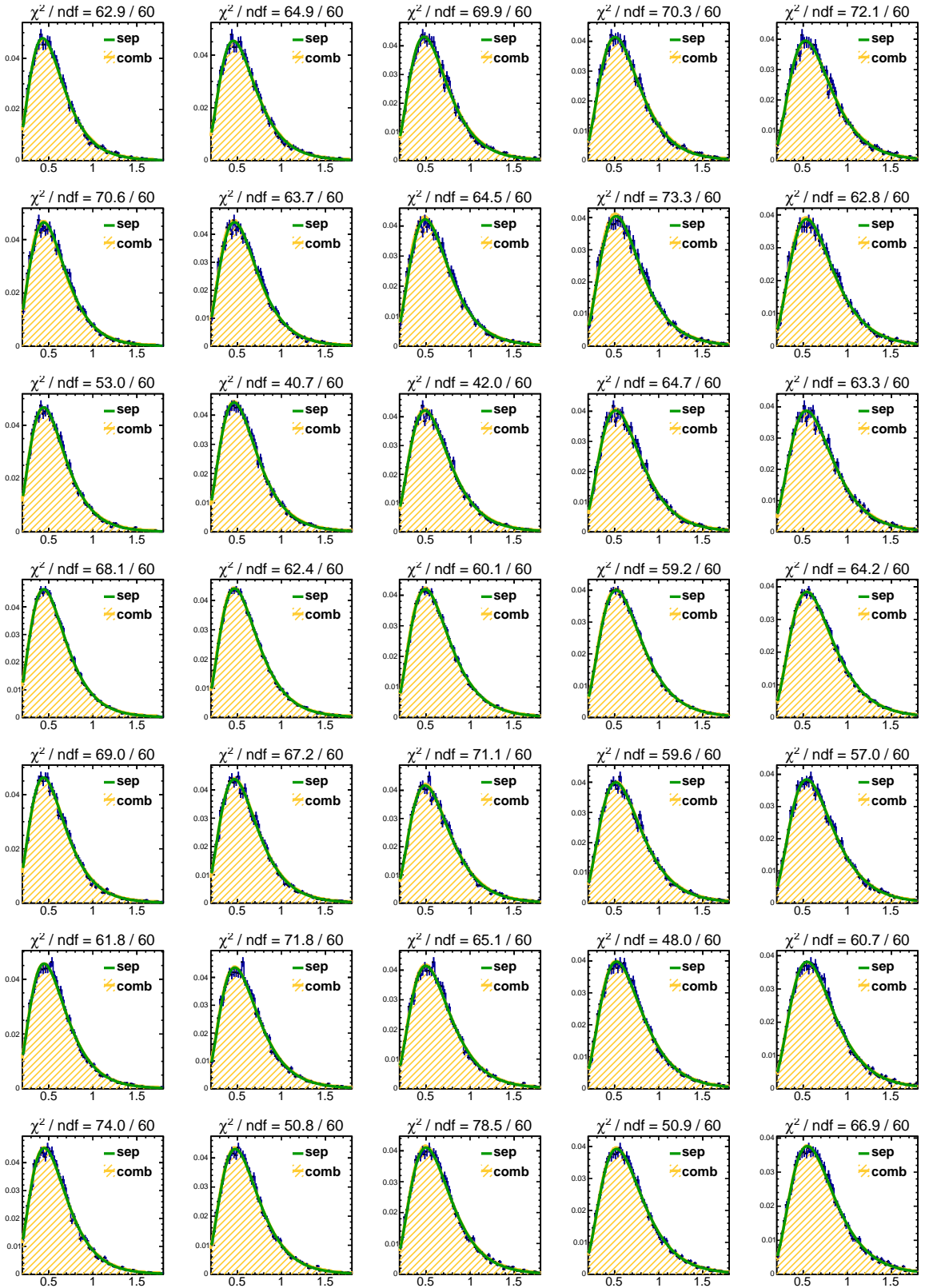


Figure 4.20: Distributions of  $R_{b1}$  for all seven mass variation samples and five values of  $bJSF$ . The individual fit is shown in green while the combined fit is indicated in yellow. The goodness of fit values stated correspond to the individual fits. The distributions arranged in one line correspond to the same masspoint, but differ in their value of  $bJSF$ , while distributions assembled in a column belong to the same  $bJSF$  but differ in the  $m_{top}$ .

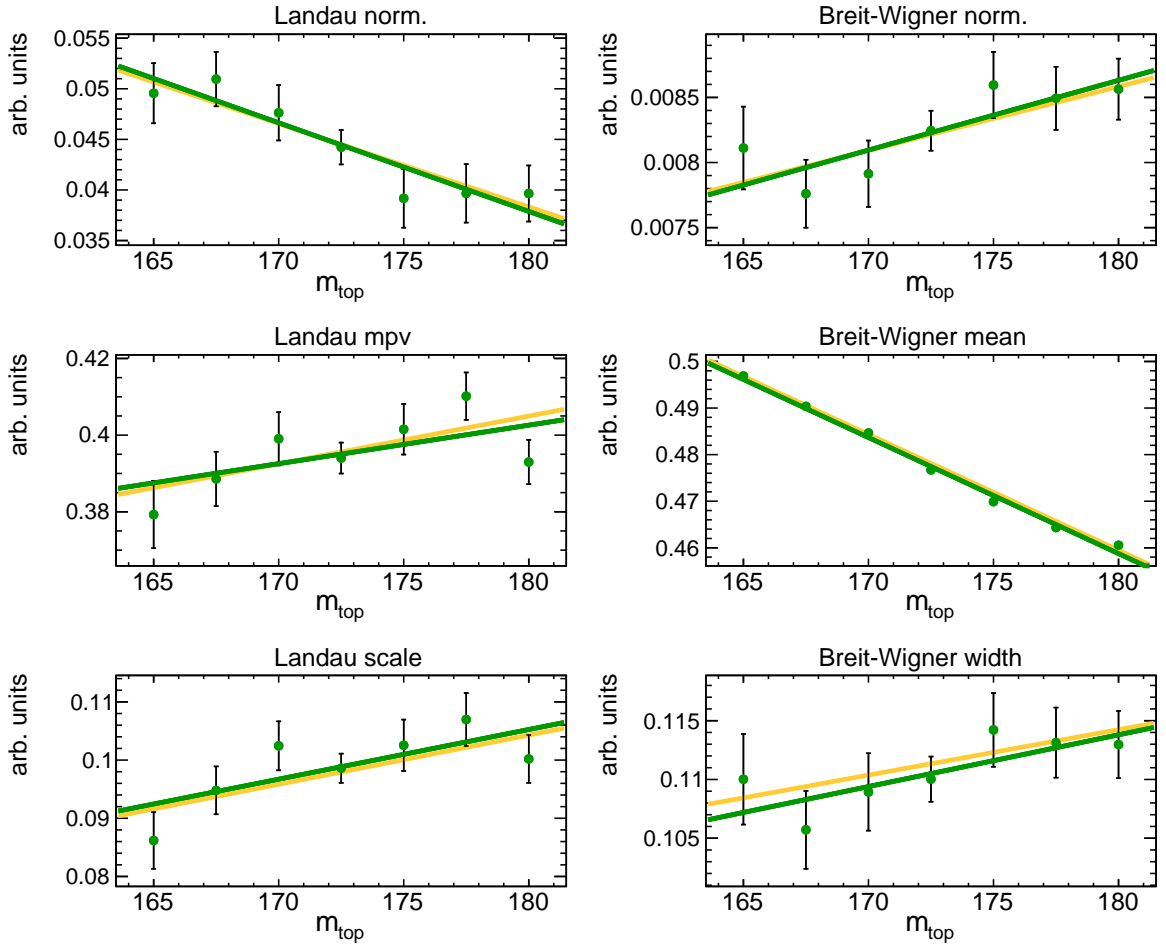
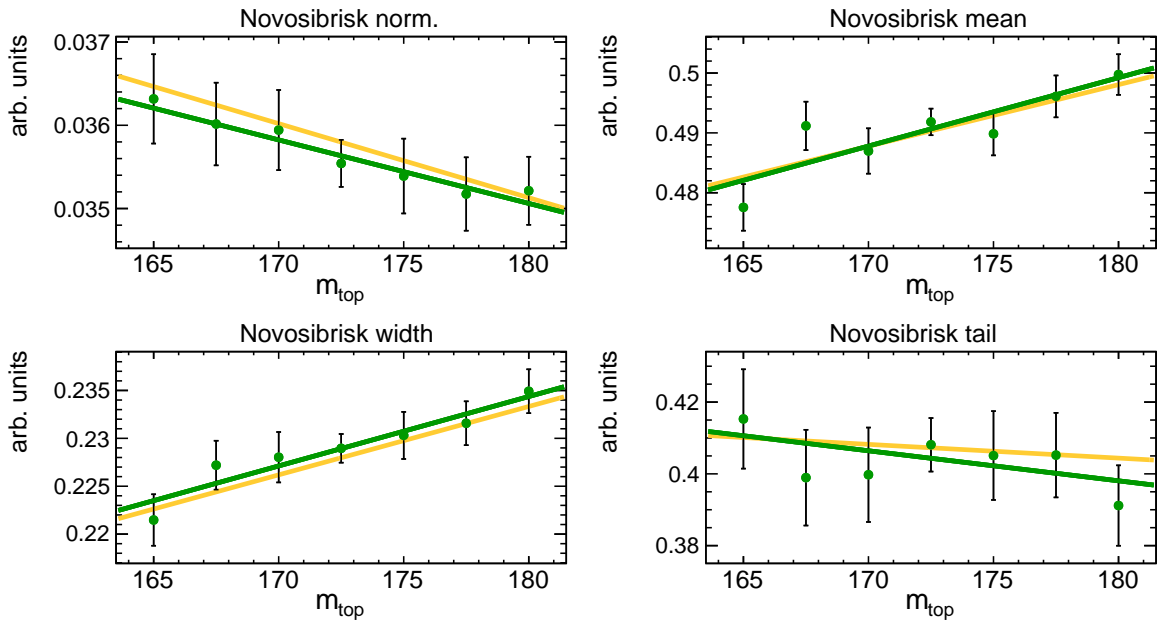
(a) Parameter distributions for  $R_{23}$ (b) Parameter distributions for  $R_{\text{bl}}$ 

Figure 4.21: Dependence of the parameters  $p_i$  on  $m_{\text{top}}$  for  $\text{bJSF} = 1$ . The linear fit of the individual parameters is shown in green. The yellow line represents the result of the combined fit.



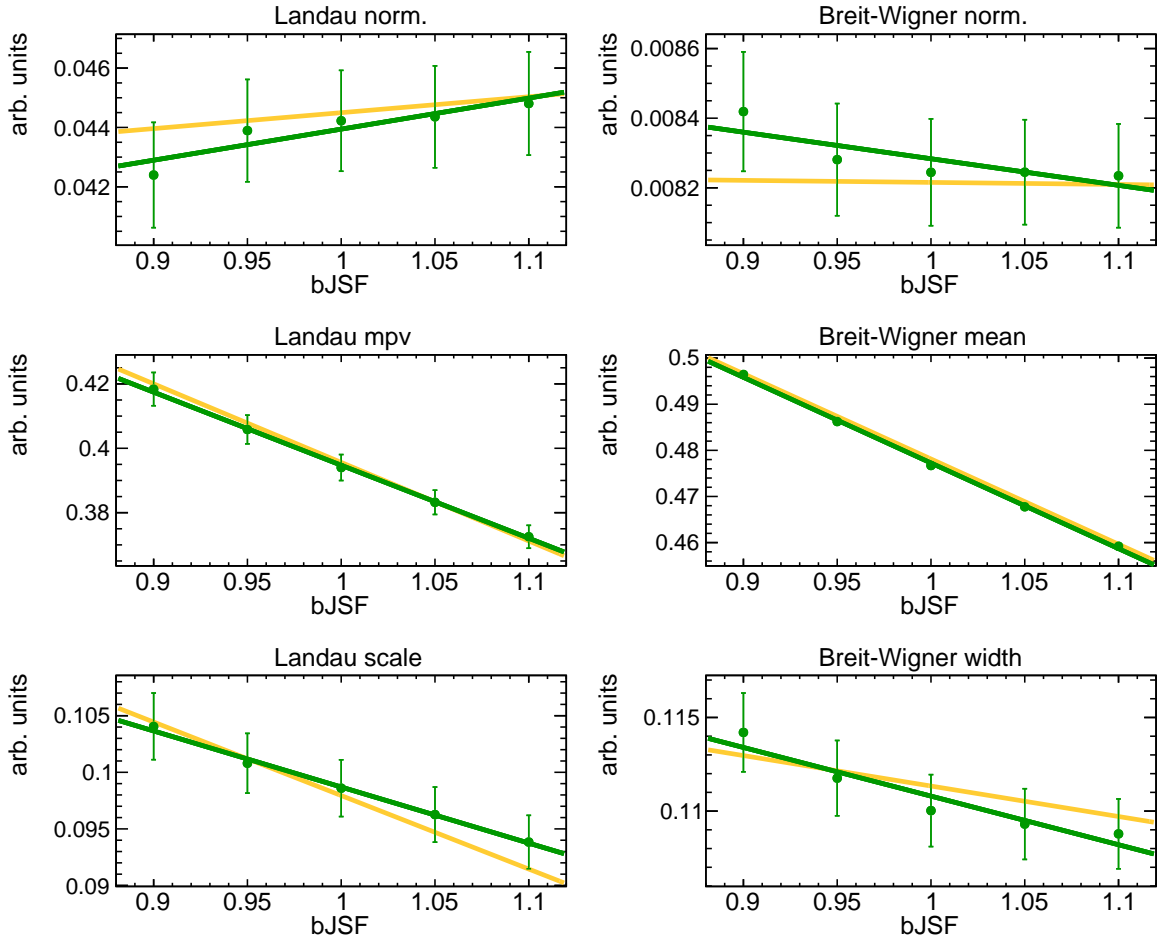
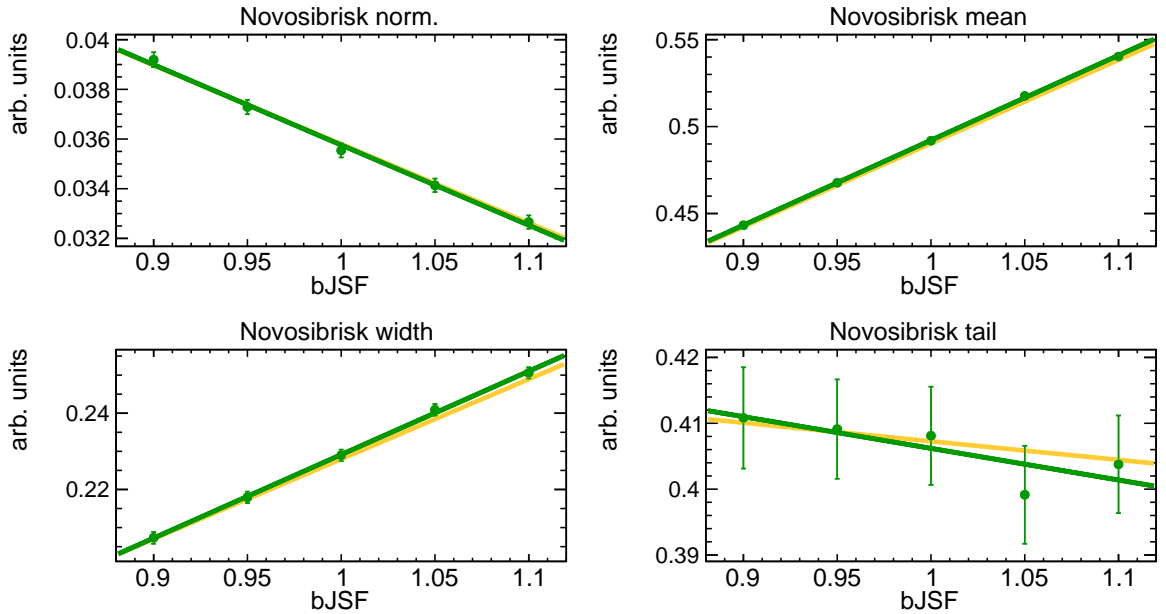
(a) Parameter distributions for  $R_{23}$ (b) Parameter distributions for  $R_{bl}$ 

Figure 4.22: Dependence of the parameters  $p_i$  on bJSF for  $m_{top} = 172.5$  GeV. The linear fit of the individual parameters is shown in green. The yellow line represents the result of the combined fit.

The template method is used to extract the value for  $m_{\text{top}}^{\text{fit}}$  from these distributions. For each  $m_{\text{top}}^{\text{fit}}$  a pull value

$$\text{pull} = \frac{(m_{\text{top}}^{\text{fit}} - m_{\text{top}})}{\sigma_{\text{fit}}} \quad (4.18)$$

is calculated, where  $m_{\text{top}}$  represents the simulated top-quark mass of the MC sample and  $\sigma_{\text{fit}}$  denotes the fit error on  $m_{\text{top}}^{\text{fit}}$ . This procedure is repeated 5000 times.

The resulting distribution of pull values is fitted with a Gauss function. The main property of this pull distribution is that its mean is equal to the bias introduced in the measurement. Furthermore, the width of the distribution is related to the quality of the fit error estimation. A width smaller than one means that the error on  $m_{\text{top}}^{\text{fit}}$  is overestimated, while a width larger than one implies an underestimation of the uncertainty.

For each of the seven mass MC variation samples, 5000 pseudo-experiments have been created. The result of the gaussian fits to the pull distributions is presented in figure 4.23.

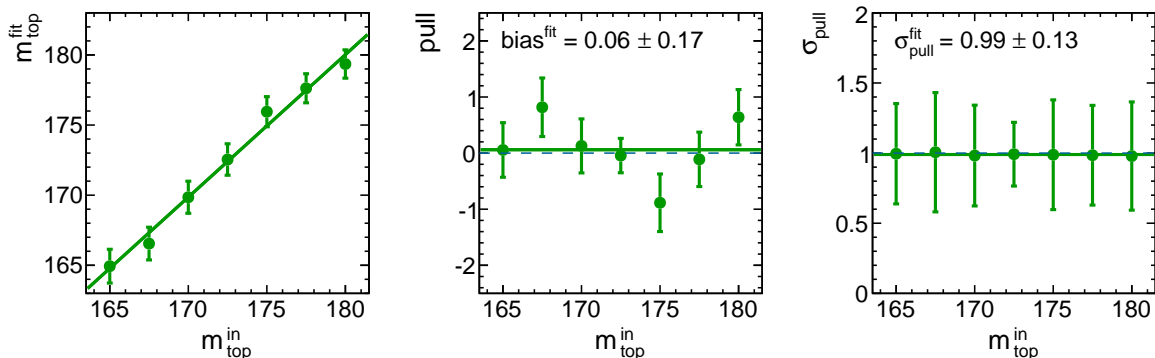


Figure 4.23: Result of 5000 pseudo-experiments. On the left, the mean value  $m_{\text{top}}^{\text{fit}}$  for the pseudo-experiments versus the input value is shown. In the middle and on the right, the mean and the width of the pull distributions are shown <sup>(22)</sup>.

The pseudo-experiments reveal no significant bias introduced by the analysis. A linear fit of the different pull means yields an offset of 0.06, which corresponds to a shift in the measured top-quark mass of only 90 MeV. With a pull width, close to one, the fit error also is well estimated. Therefore, the shift in the values of  $m_{\text{top}}^{\text{fit}}$  in figure 4.17, especially in the case of  $\text{bJSF} = 0.9$ , is likely to be a statistical fluctuation.

In total, it can be concluded, that the template method described in this chapter is valid to determine the values of  $m_{\text{top}}$  and  $\text{bJSF}$  in experimental data.

<sup>(22)</sup>Due to the 5000 pseudo-experiments, the count of pseudo-events outnumbers the available MC events by far. This causes an underestimation of the pull parameter errors, which is explicitly corrected for. <sup>[71]</sup>

## 5. Conclusion

In this analysis a MC based approach was presented, which aims to reduce the impact of the jet energy scale on the top-quark mass uncertainty. Therefore, instead of the invariant mass of the reconstructed top-quark, another estimator for  $m_{\text{top}}$  is chosen. The two estimators under study are  $R_{23}$  and  $R_{32}$ , which both possess a reduced dependence on the light-jet energy scale. However, these estimators are still influenced by the  $b$ -jet energy scale. To account for this dependence, a second observable is introduced. The  $R_{b1}$  estimator is especially constructed to be primarily dependent on the specific value of the  $b$ -jet energy scale factor. Additionally, a minor dependence on the top-quark mass is explicitly taken into account.

The main estimator used in this analysis is  $R_{23}$ . Compared to  $R_{32}$  this observable offers two advantages. First,  $R_{23}$  allows for a larger range of top-quark masses, while second, it introduces only a negligible bias in the measurement.

With the results shown in figure 4.18, the impact of the bJSF on a measurement of  $m_{\text{top}}$  can be estimated. The expected error due to a variation of the  $b$ -jet scale uncertainty is given by the half of the maximum difference of the fitted top-quark masses. Taking into account bJSF values from 0.9 to 1.1, the error on  $m_{\text{top}}$  is 0.31 GeV. However, the  $b$ -jet scale factor is experimentally verified to a precision of  $\leq 5\%$  in the momentum range considered for this analysis (cf. fig. 4.5). Therefore, values of bJSF smaller than 0.95 and larger than 1.05 are excluded experimentally. Hence, the anticipated contribution to the error on  $m_{\text{top}}$ , due to the  $b$ -jet scale uncertainty, can be reduced to 0.08 GeV.

Although this study is solely based on MC simulations, the impact of a successful application of the presented method in real data looks quite promising. With this approach the systematic uncertainty on a top-quark mass measurement with the ATLAS detector could be reduced considerably.

## A. The $R_{32}$ estimator

In this chapter the same analysis done for  $R_{23}$  is shown for the  $R_{32}$  estimator.

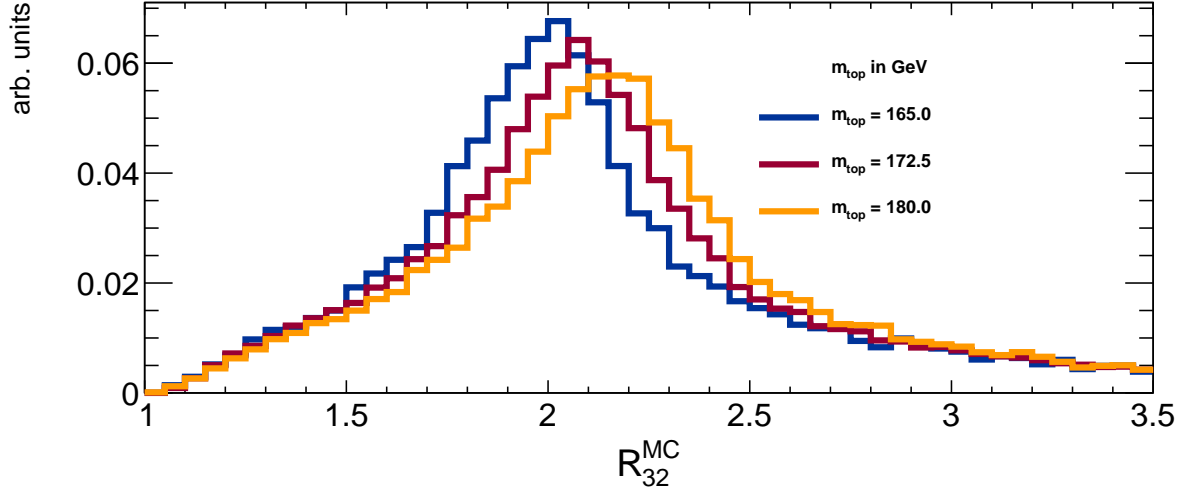


Figure A.1: Distributions of  $R_{32}$  for input top quark mass of 165 GeV, 172.5 GeV and 180 GeV

For different mass points, the distribution of  $R_{32}$  is shown in figure A.1. Similar to the  $m_{jjj}$  distribution (cf. figure 4.9)  $R_{32}$ -values become larger for an increasing top quark mass. Still visible is the tail of the distribution, which corresponds to wrong jet-parton assignments. Figure A.2 shows the dependence of  $R_{32}$  on the light an  $b$ -jet scale factors.

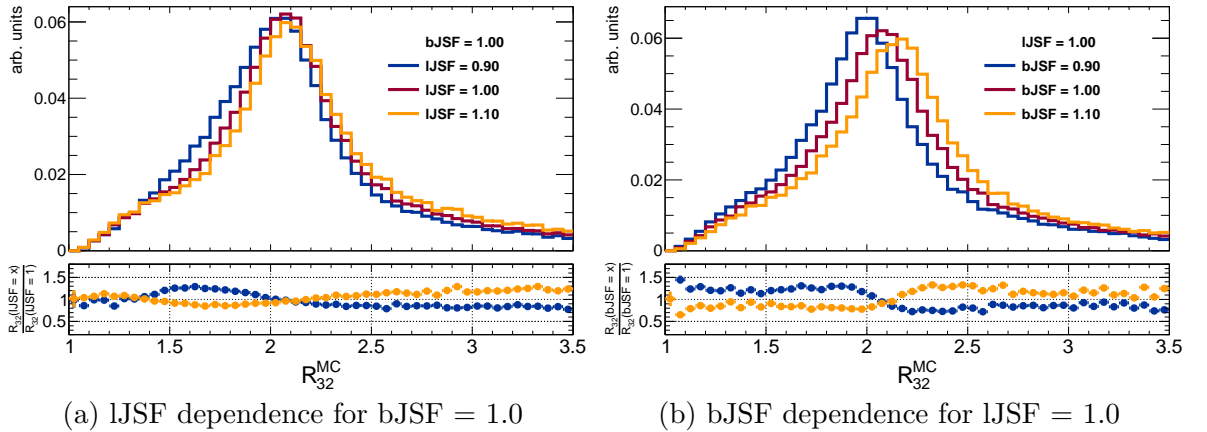


Figure A.2: Influence of the jet scale factors lJSF and bJSF on  $R_{32}$

The  $R_{32}$  estimator is shifted to higher values for an increased  $b$ -jet scale factor, while there is only a minor shift for a variation of the light jet scale factor.

## A.1. Parametrisation

The parametrisation of  $R_{32}$  is done with the sum of a Landau function and a Gauss function. Again the Landau function accounts for the combinatorial background while the Gauss function describes the signal peak. The parametrisation of  $R_{32}$  has therefore six free parameters and is shown in A.3. The fitted function ranges from 1.5 to 3.49 and consequently accounts for hypothetical top quark masses of 120 to 280 GeV.

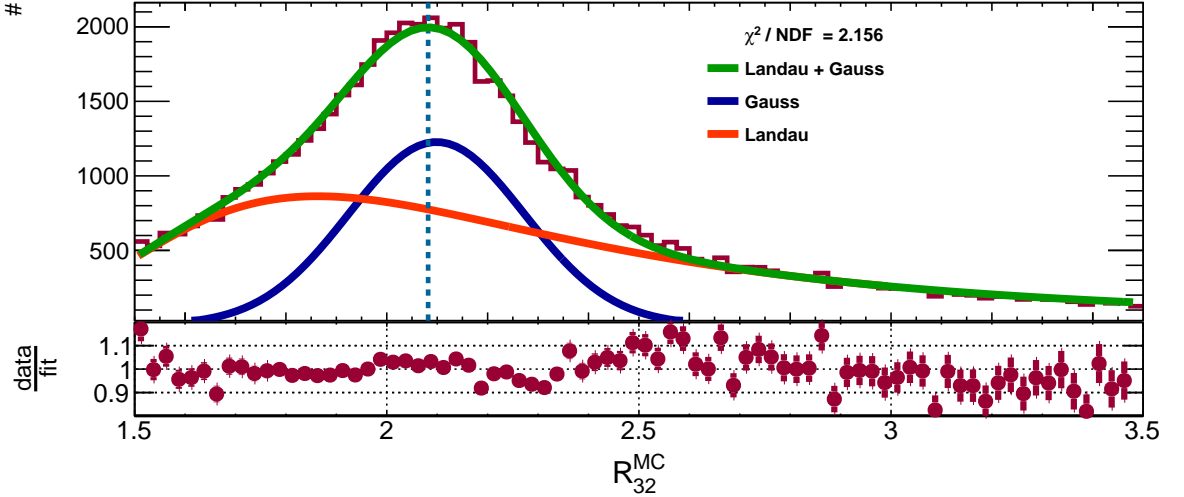


Figure A.3: LJSF dependence for  $bJSF = 1.0$

## A.2. Templates for $R_{32}$

In this section the templates for the  $R_{32}$  distributions are shown. The parametrised distributions can be found in figure A.5, while the parameter set corresponding to a fixed value of  $bJSF$  and  $m_{top}$  is shown in figure A.6.

Also in this case the linear description of the  $R_{32}$  parameter dependence on  $m_{top}$  and  $bJSF$  is valid. The agreement between the separate and the combined fit is slightly worse than in case of  $R_{23}$ , but the main point is the sensitivity of the Gauss mean to the top quark mass. Applying pseudo-experiment reveals a slightly larger bias of the  $R_{32}$  estimator than for  $R_{23}$ . This bias corresponds to a shift in the top quark mass of about 200 MeV and is the main reason why the  $R_{23}$  estimator is chosen to determine the top quark mass. (cf. fig. A.4)

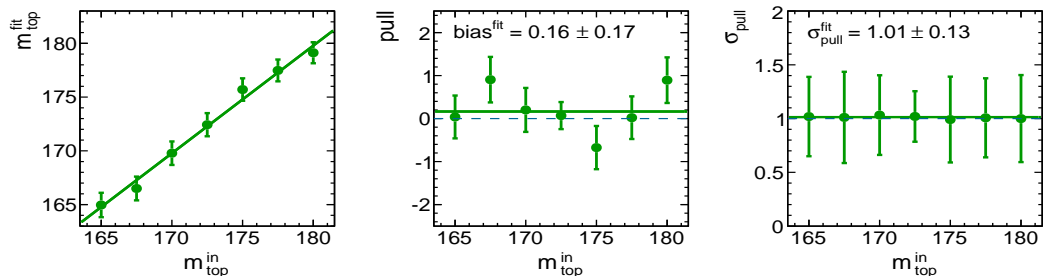


Figure A.4: Result of 5000 pseudo-experiments. On the left, the mean value  $m_{top}^{fit}$  for the pseudo-experiments versus the input value is shown. In the middle and on the right, the mean and the width of the pull distributions are shown.

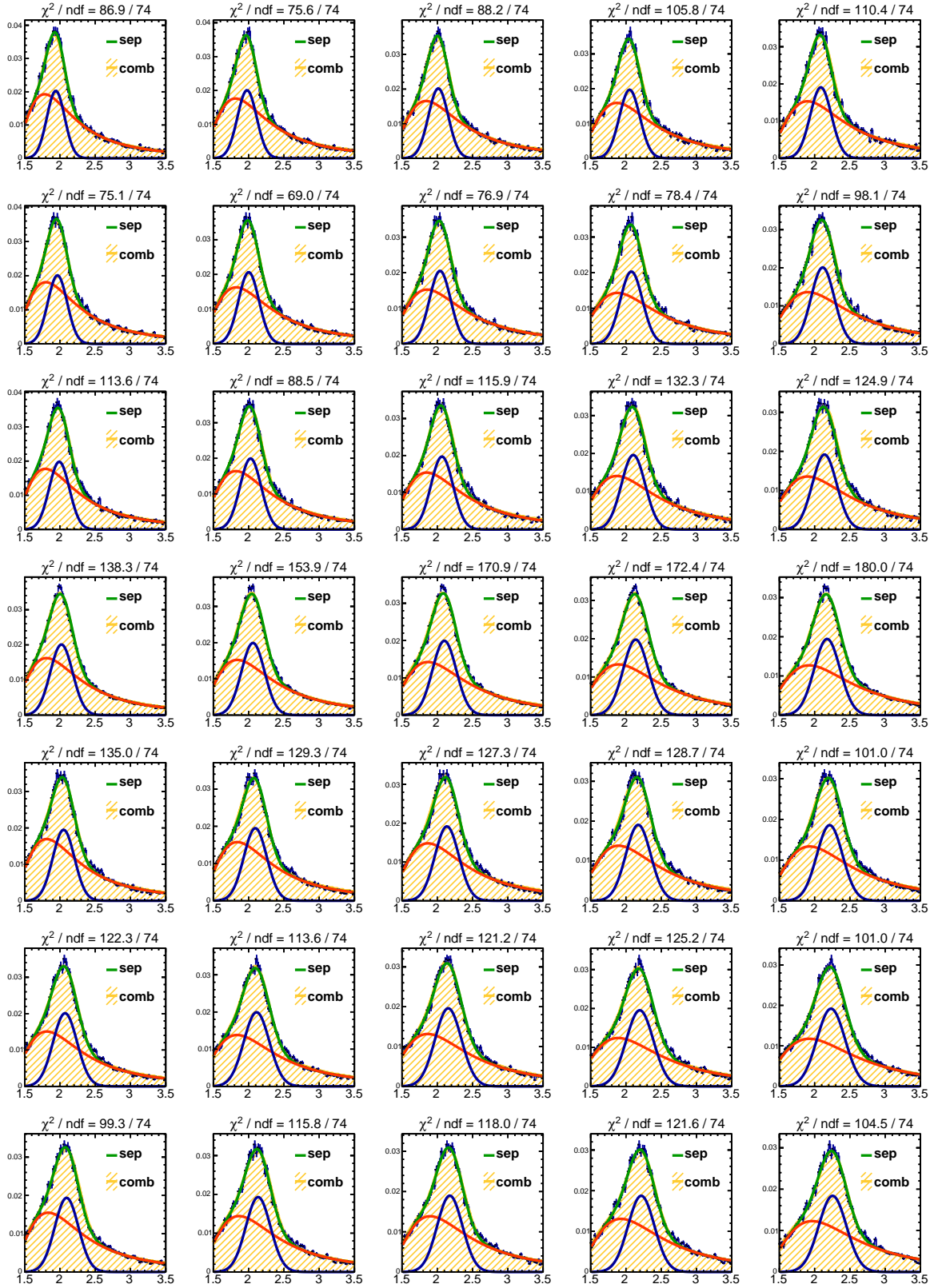
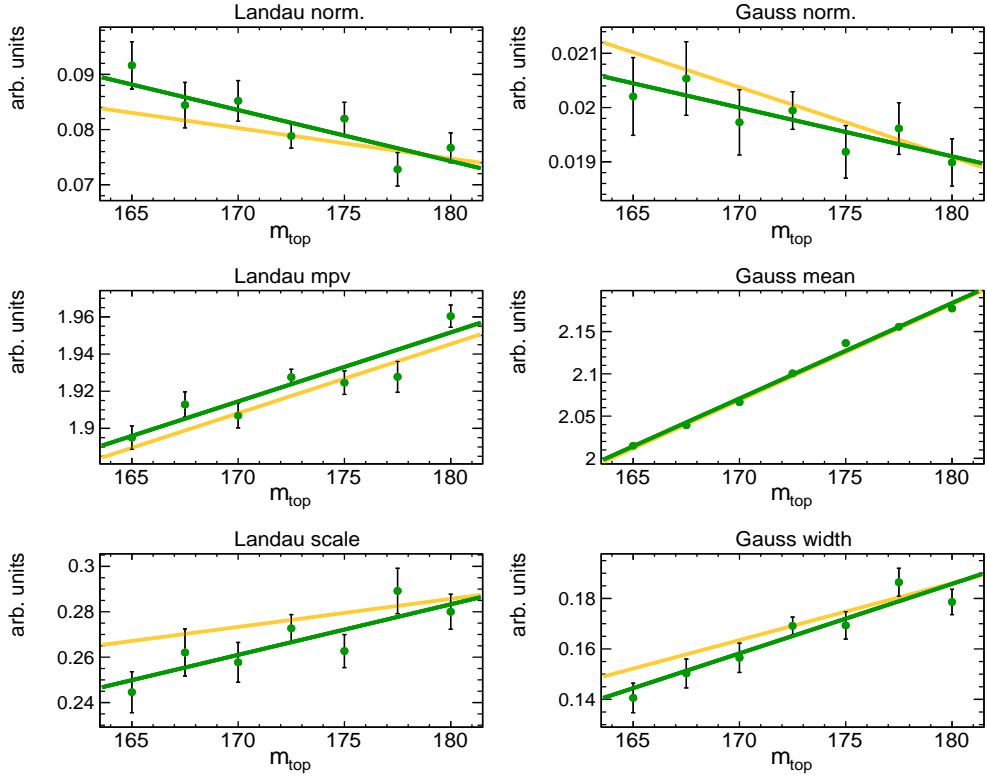
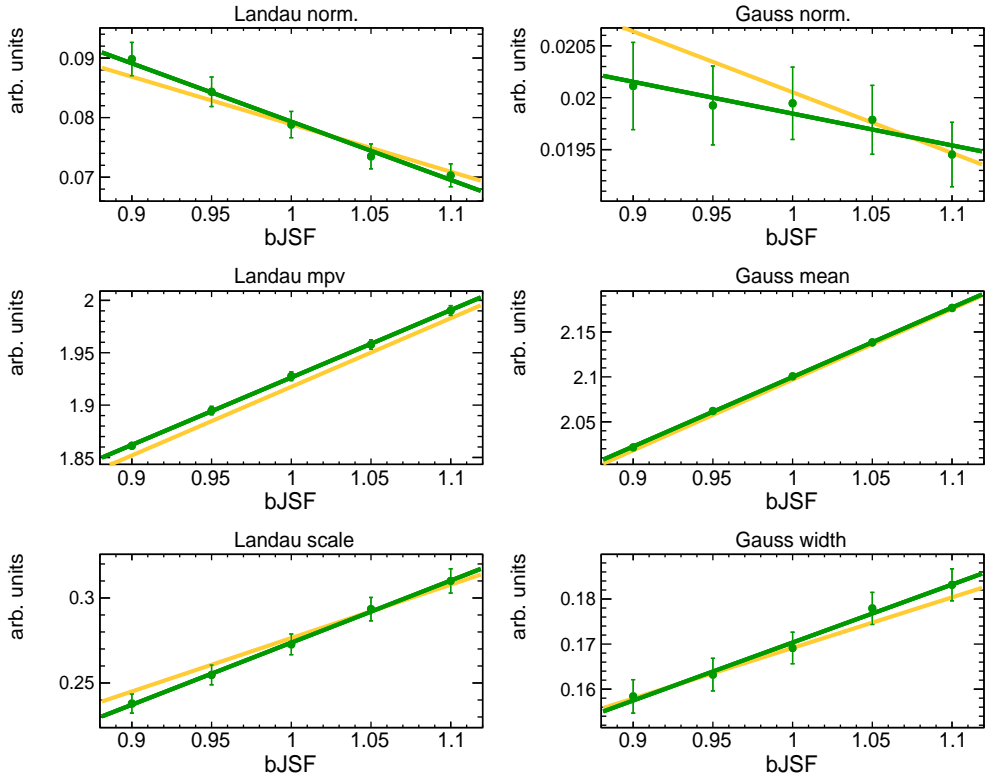


Figure A.5: Distributions of  $R_{32}$  for all seven mass variation samples and five values of bJSF. The individual fit is shown in green while the combined fit is indicated in yellow. The goodness of fit values stated correspond to the individual fits. The distributions arranged in one line correspond to the same masspoint, but differ in their value of bJSF, while distributions assembled in a column belong to the same bJSF but differ in the  $m_{\text{top}}$ .



(a) Dependence on  $m_{\text{top}}$  for  $b\text{JSF} = 1$



(b) Dependence on  $b\text{JSF}$  with  $m_{\text{top}} = 172.5$  GeV

Figure A.6: Dependence of the  $R_{32}$  parameters on  $m_{\text{top}}$  and  $b\text{JSF}$ . The individual parameters together with a linear fit are shown in green. Also indicated are the uncertainties on the particular parameters. The yellow line represents the result of the combined fit.

## B. Mathematical functions

### B.1. Landau

One possible parametrisation of the Landau function is given by

$$f(x) = N \cdot \int_0^\infty \sin(2t) e^{-t \frac{x-\mu}{\sigma} - \frac{2}{\pi} t \ln(t)} dx \quad (\text{B.1})$$

The function used in this analysis is implemented in the ROOT data analysis framework<sup>[72]</sup>. The impact of the three parameters is shown in figure B.1.

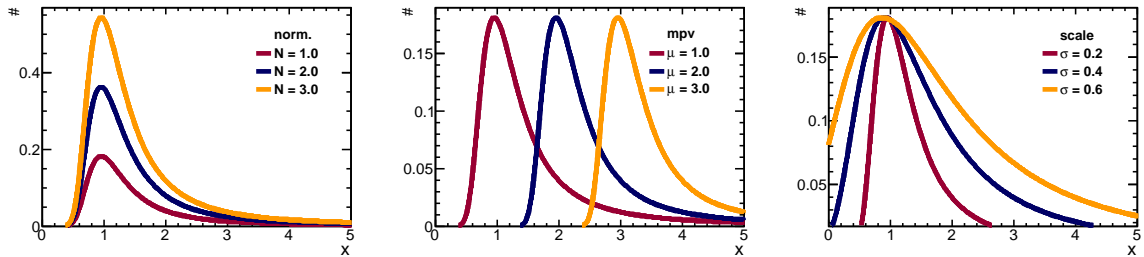


Figure B.1: Impact of parameter variations on the Landau function

### B.2. Breit-Wigner

The Breit-Wigner function is given by

$$f(x) = \frac{N}{2\pi} \frac{\Gamma}{(x - x_0)^2 + \frac{\Gamma^2}{4}} \quad (\text{B.2})$$

Figure B.2 shows the influence of different parameter values on the Breit-Wigner function.

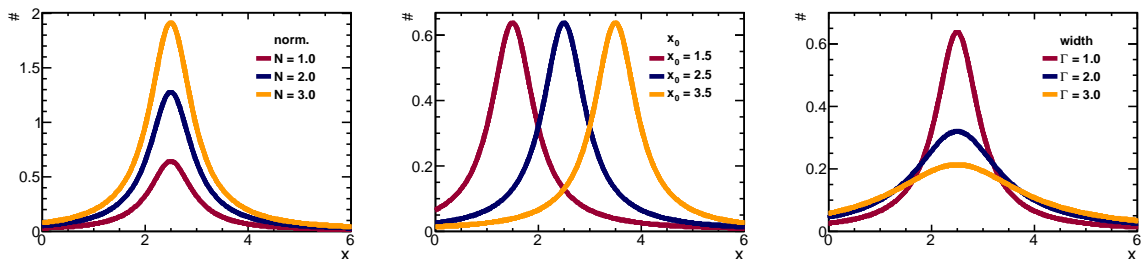


Figure B.2: Impact of parameter variations on the Breit-Wigner function



### B.3. Novosibirsk

The Novosibirsk function<sup>[73]</sup> is defined as

$$f(x) = N \cdot \exp \left( -\frac{1}{2} \cdot \left( \frac{\ln \left( 1 + \tau \cdot (x - x_0) \frac{\sinh(\tau\sqrt{\ln 4})}{\sigma\tau\sqrt{\ln 4}} \right)}{\tau} \right)^2 + \tau^2 \right) \quad (\text{B.3})$$

However, to avoid errors in the fitting procedure, an artificial modulus is introduced, the resulting function is therefore given by

$$f(x) = N \cdot \exp \left( -\frac{1}{2} \cdot \left( \frac{\ln \left( \left| 1 + \tau \cdot (x - x_0) \frac{\sinh(\tau\sqrt{\ln 4})}{\sigma\tau\sqrt{\ln 4}} \right| \right)}{\tau} \right)^2 + \tau^2 \right) \quad (\text{B.4})$$

In figure B.3 the effects of varying the parameters of the Novosibirsk function are shown.

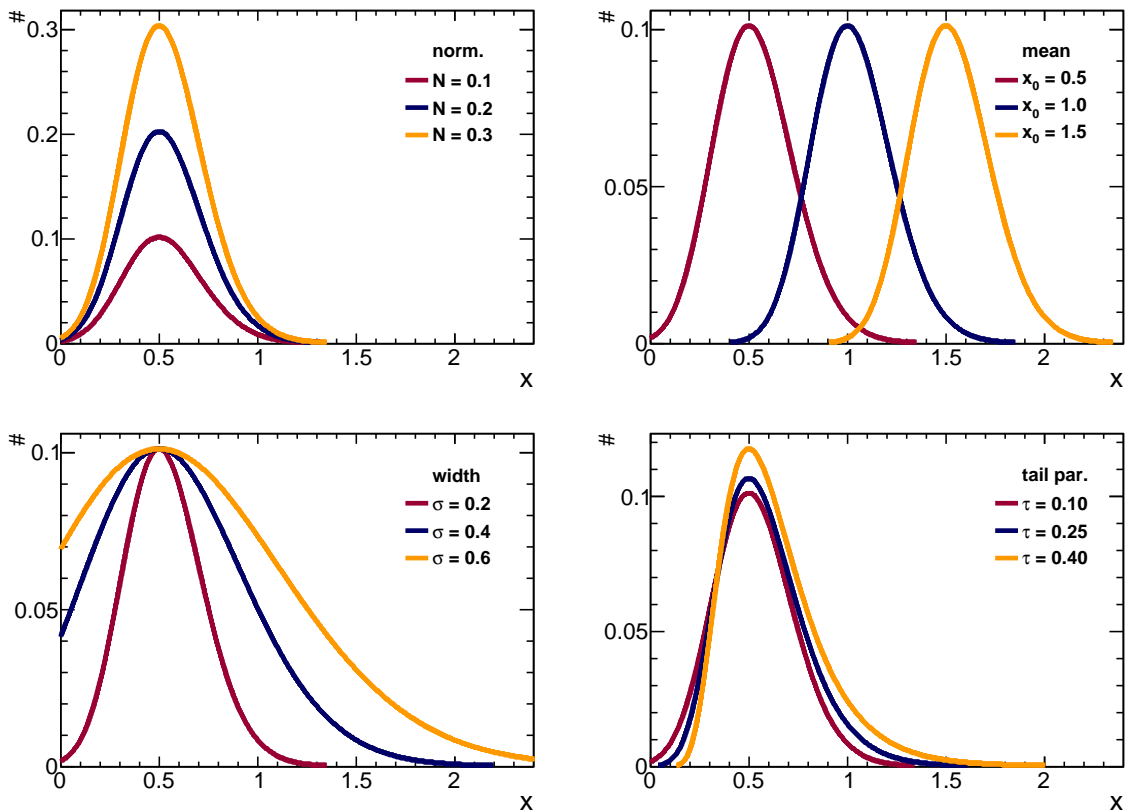


Figure B.3: Impact of parameter variations on the Novosibirsk function

## B.4. Gauss

The Gauss function<sup>[73]</sup> is given by

$$f(x) = N \cdot e^{-\frac{1}{2} \frac{(x-\mu)^2}{\sigma^2}} \quad (\text{B.5})$$

The effect of varying one of the function parameters is indicated in figure B.4

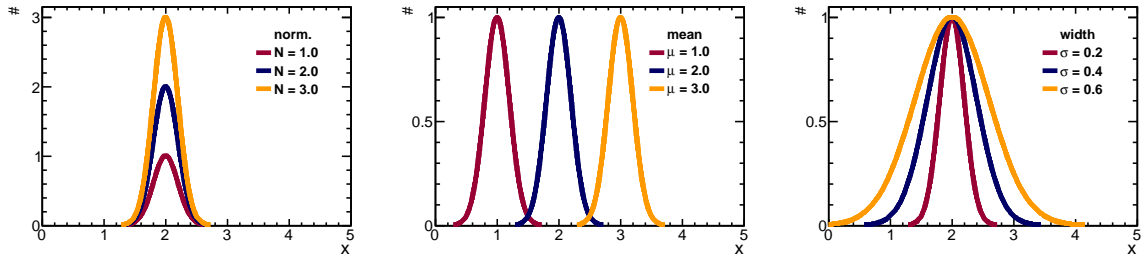


Figure B.4: Impact of parameter variations on the Gauss function

## C. Template method: parameter values and plots

In this chapter the parameters obtained by the individual and combined fit of the template distributions are listed (cf. tabs C.3 and C.2). In addition, the subsequent figures present the remaining parameter plots for the  $R_{23}$  template method. However, in table C.1 the correlation values between the individual fit parameters of the Landau and Breit-Wigner function are stated.

for constant bJSF = 1			
$\rho$	Breit-Wigner norm.	Breit-Wigner mean	Breit-Wigner width
Landau norm.	-0.951	0.948	-0.924
Landau mpv	0.478	-0.712	0.525
Landau scale	0.468	-0.782	0.491
for constant $m_{\text{top}} = 172.5$ GeV			
$\rho$	Breit-Wigner norm.	Breit-Wigner mean	Breit-Wigner width
Landau norm.	-0.982	-0.919	-0.973
Landau mpv	0.849	1.000	0.964
Landau scale	0.866	0.999	0.968

Table C.1.: Correlations of the individual Landau and Breit-Wigner parameters

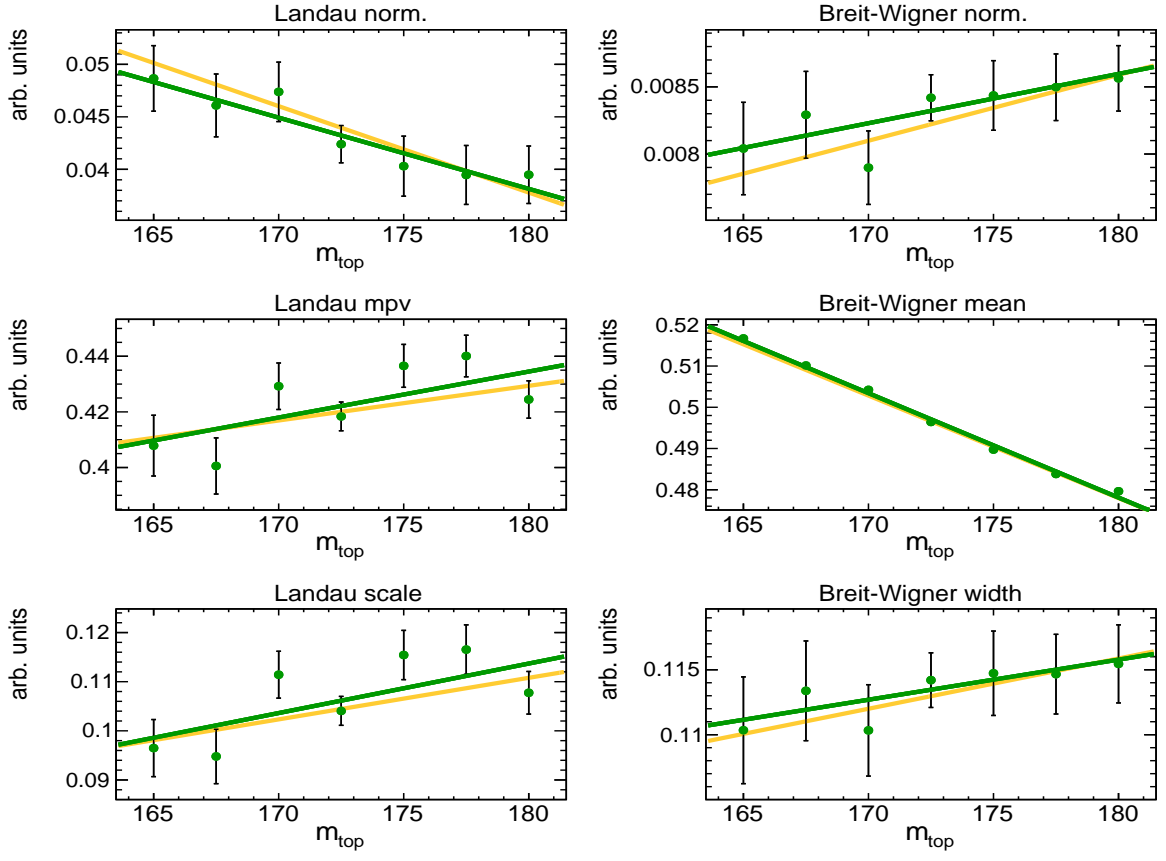
combined fit parameters			
	$a$	$b$	$c$
Landau norm.	$0.181099 \pm 0.013069$	$-0.000823 \pm 0.000071$	$0.005366 \pm 0.005514$
Landau mpv	$0.424569 \pm 0.018032$	$0.001247 \pm 0.000099$	$-0.244060 \pm 0.011426$
Landau scale	$0.016961 \pm 0.010013$	$0.000846 \pm 0.000056$	$-0.064949 \pm 0.006501$
Breit-Wigner norm.	$-0.000178 \pm 0.001121$	$0.000049 \pm 0.000006$	$-0.000059 \pm 0.000494$
Breit-Wigner mean	$1.092002 \pm 0.004028$	$-0.002487 \pm 0.000022$	$-0.184864 \pm 0.001445$
Breit-Wigner width	$0.060853 \pm 0.013674$	$0.000387 \pm 0.000075$	$-0.016272 \pm 0.006200$
Novosibirsk norm.	$0.082868 \pm 0.003358$	$-0.000089 \pm 0.000018$	$-0.031718 \pm 0.001001$
Novosibirsk mean	$-0.167534 \pm 0.030560$	$0.001029 \pm 0.000165$	$0.480375 \pm 0.007981$
Novosibirsk width	$-0.104837 \pm 0.015687$	$0.000714 \pm 0.000085$	$0.209644 \pm 0.004610$
Novosibirsk tail	$0.501527 \pm 0.107370$	$-0.000383 \pm 0.000577$	$-0.028197 \pm 0.025306$

Table C.2.: Parameter values obtained by the combined fit

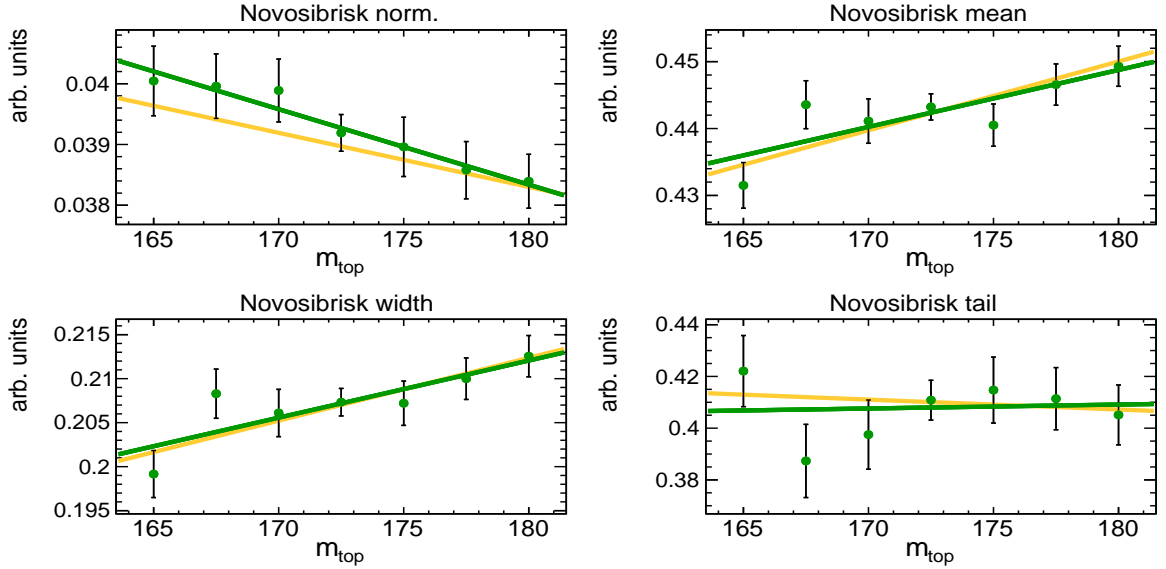
individual fit parameters for bJSF = 1		
	$a^{m_{\text{top}}}$	$b^{m_{\text{top}}}$
Landau norm.	$0.195444 \pm 0.0370144$	$-0.000875334 \pm 0.000214506$
Landau mpv	$0.221881 \pm 0.0901365$	$0.00100397 \pm 0.000519813$
Landau scale.	$-0.0483785 \pm 0.0574079$	$0.000853496 \pm 0.000332449$
Breit-Wigner norm.	$-0.00101561 \pm 0.00344466$	$5.3594 \cdot 10^{-5} \pm 1.98985 \cdot 10^{-5}$
Breit-Wigner mean	$0.907422 \pm 0.00916908$	$-0.00249259 \pm 5.30104 \cdot 10^{-5}$
Breit-Wigner width	$0.0344817 \pm 0.0425139$	$0.000440666 \pm -0.000245481$
Novosibirsk norm.	$0.0487941 \pm 0.00610828$	$-7.62939 \cdot 10^{-5} \pm 3.5268 \cdot 10^{-5}$
Novosibirsk mean	$0.293488 \pm 0.0480386$	$0.00114301 \pm 0.000277691$
Novosibirsk width	$0.103918 \pm 0.0322596$	$0.000724702 \pm 0.000186474$
Novosibirsk tail	$0.548801 \pm 0.163351$	$-0.000837459 \pm 0.000943689$
individual fit parameters for $m_{\text{top}} = 172.5$ GeV		
	$c^{\text{bJSF}}$	$d^{\text{bJSF}}$
Landau norm.	$0.0334753 \pm 0.0111012$	$0.0104677 \pm 0.0110647$
Landau mpv	$0.621612 \pm 0.027481$	$-0.226862 \pm 0.0269548$
Landau scale.	$0.148246 \pm 0.016757$	$-0.049547 \pm 0.0165529$
Breit-Wigner norm.	$0.00904698 \pm 0.0010156$	$-0.000763521 \pm 0.00100636$
Breit-Wigner mean	$0.662959 \pm 0.00275957$	$-0.185692 \pm 0.0027452$
Breit-Wigner width	$0.136776 \pm 0.0125998$	$-0.0259753 \pm 0.0124951$
Novosibirsk norm.	$0.0680524 \pm 0.00181256$	$-0.0322907 \pm 0.00179699$
Novosibirsk mean	$0.00368906 \pm 0.0138504$	$0.488437 \pm 0.0139797$
Novosibirsk width	$0.0102626 \pm 0.0096525$	$0.218866 \pm 0.00960835$
Novosibirsk tail	$0.454266 \pm 0.0478686$	$-0.0480775 \pm 0.0476686$

Table C.3.: Parameter values obtained by the individual fits

### C.1. Plots for varied $m_{\text{top}}$ and constant bJSF values

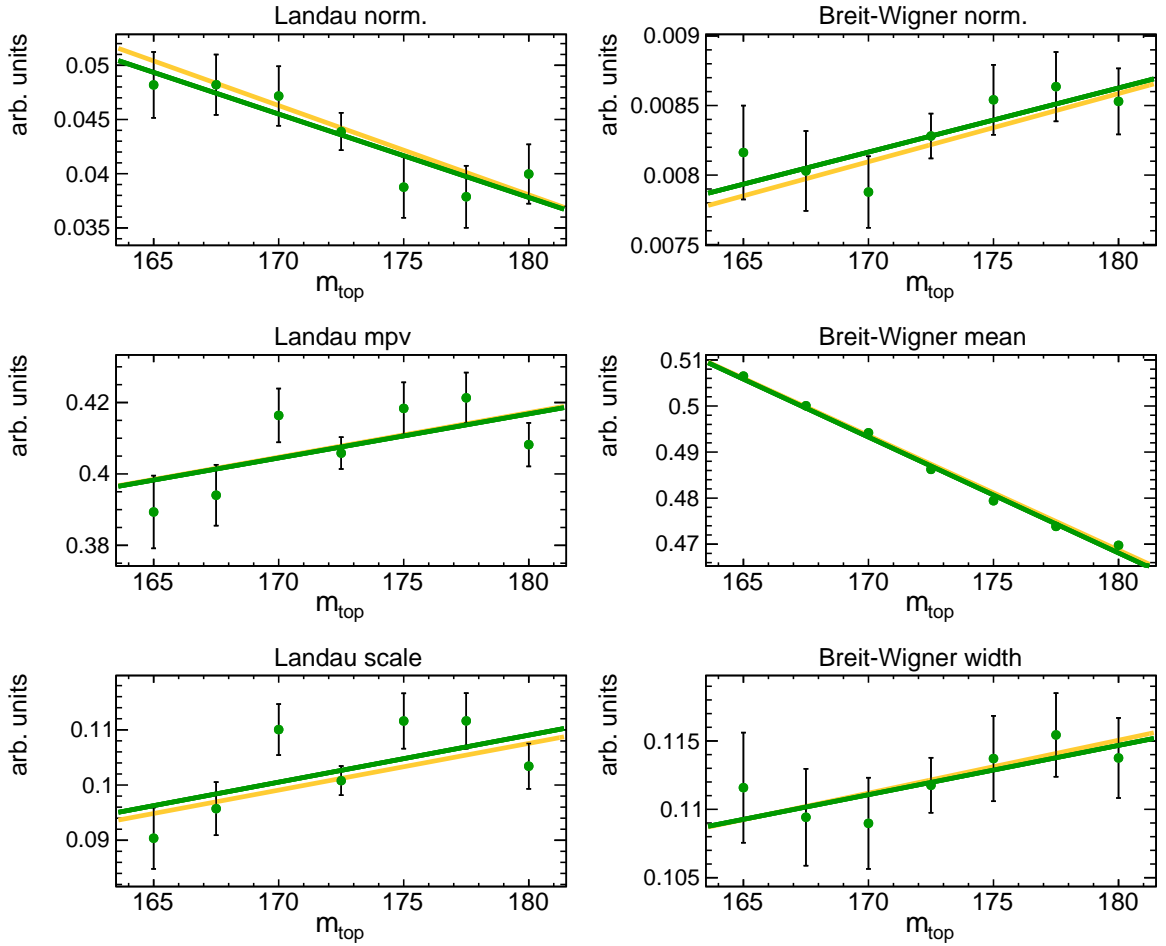


(a) Parameter distributions for  $R_{23}$

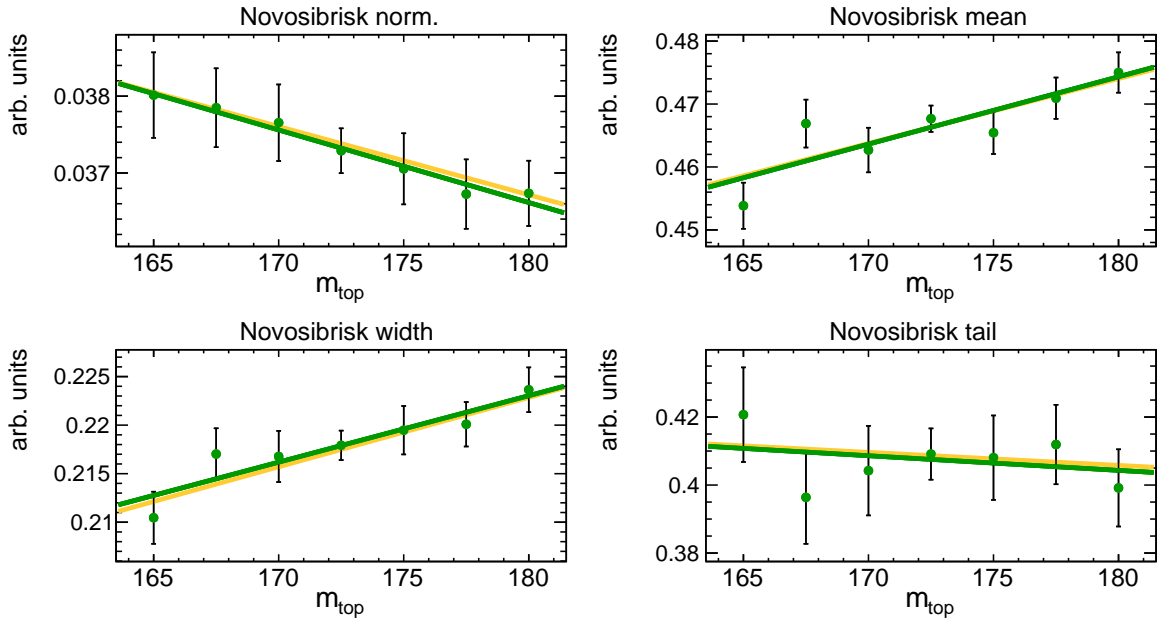


(b) Parameter distributions for  $R_{b1}$

Figure C.1: Dependence of the parameters  $p_i$  on  $m_{\text{top}}$  for bJSF = 0.90. The linear fit of the individual parameters is shown in green. The yellow line represents the result of the combined fit.

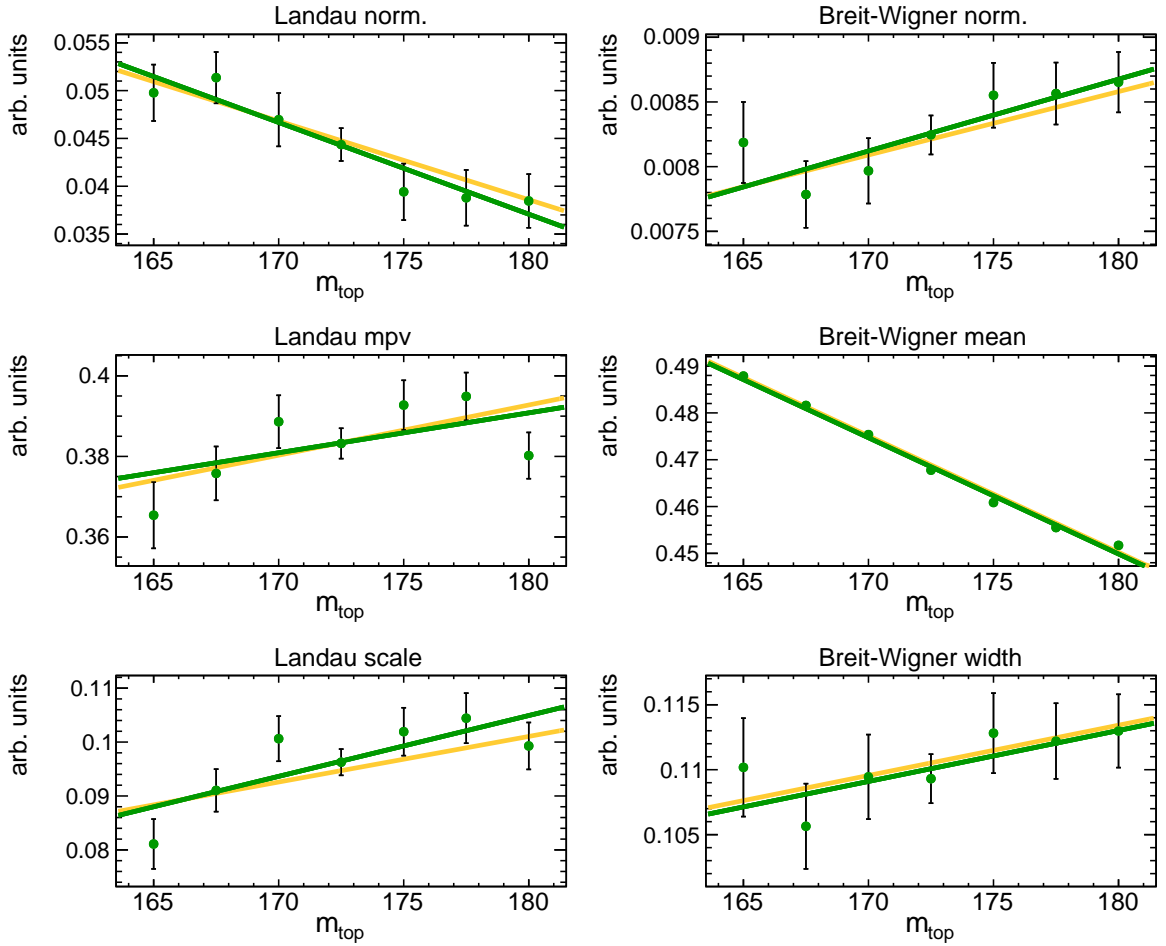


(a) Parameter distributions for  $R_{23}$

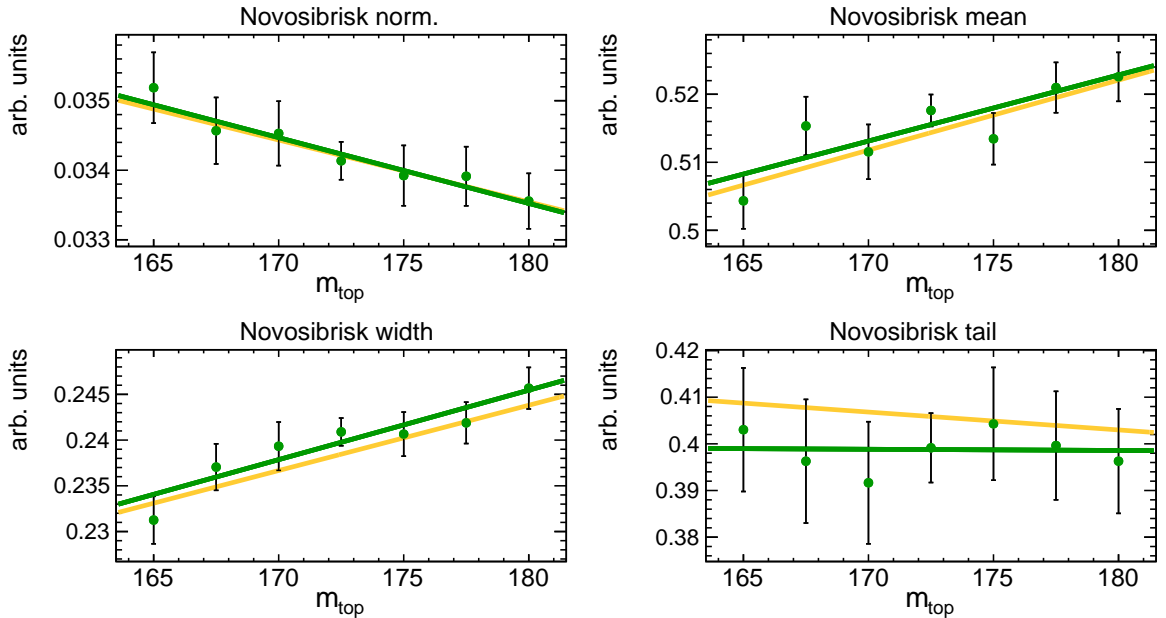


(b) Parameter distributions for  $R_{b1}$

Figure C.2: Dependence of the parameters  $p_i$  on  $m_{\text{top}}$  for  $\text{bJSF} = 0.95$ . The linear fit of the individual parameters is shown in green. The yellow line represents the result of the combined fit.

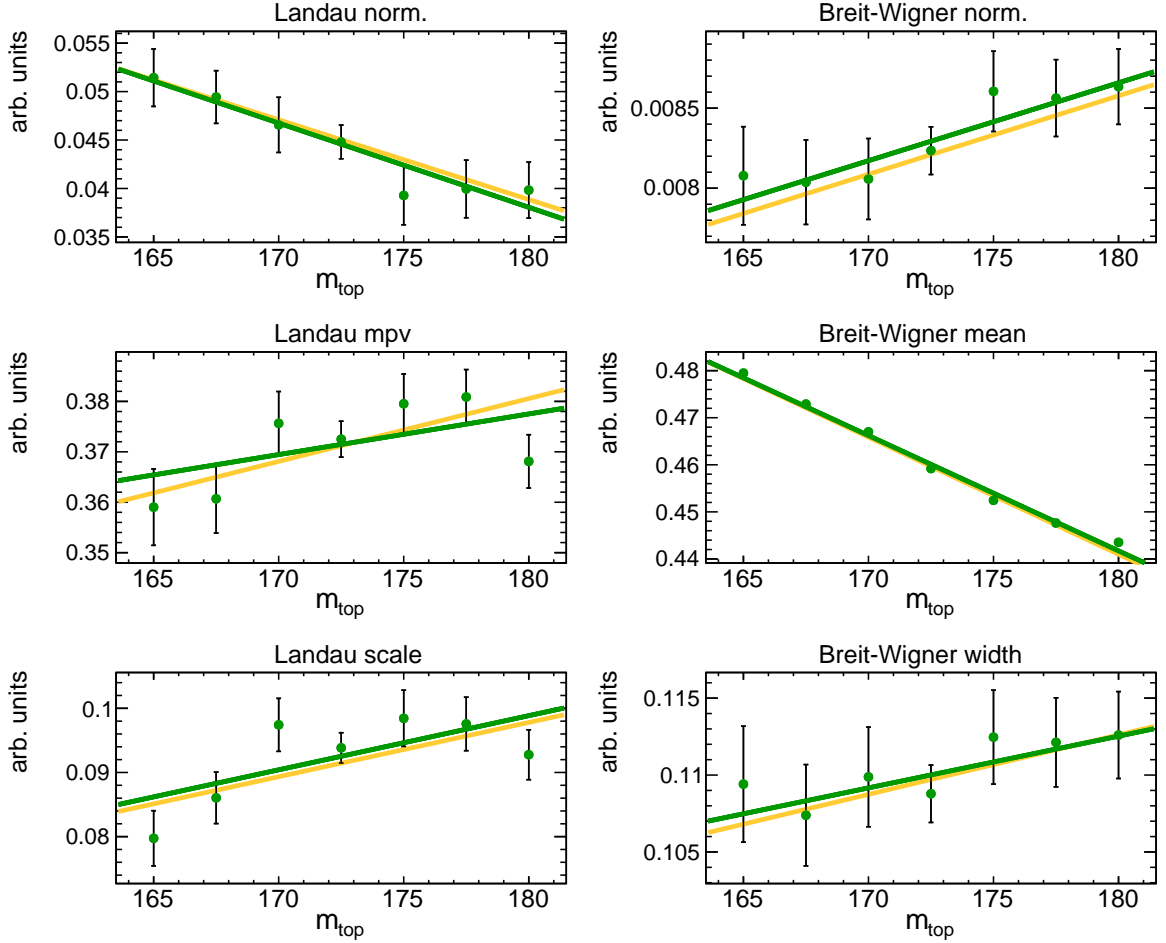


(a) Parameter distributions for  $R_{23}$

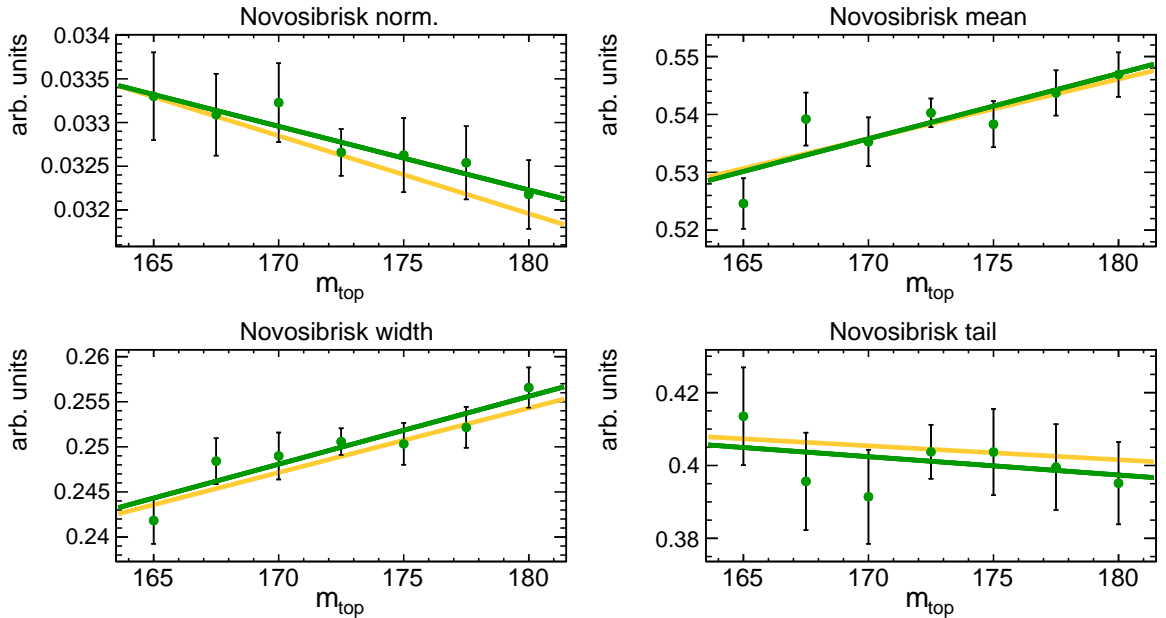


(b) Parameter distributions for  $R_{b1}$

Figure C.3: Dependence of the parameters  $p_i$  on  $m_{\text{top}}$  for  $\text{bJSF} = 1.05$ . The linear fit of the individual parameters is shown in green. The yellow line represents the result of the combined fit.



(a) Parameter distributions for  $R_{23}$

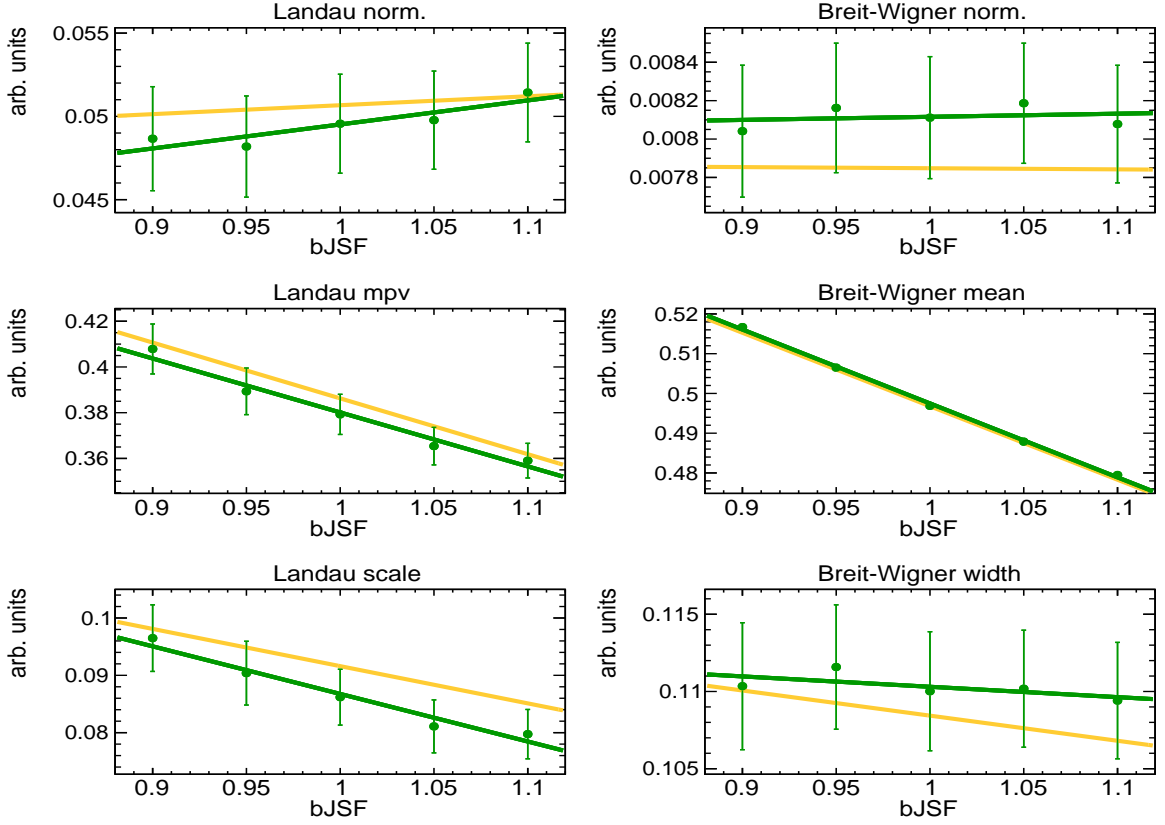


(b) Parameter distributions for  $R_{bl}$

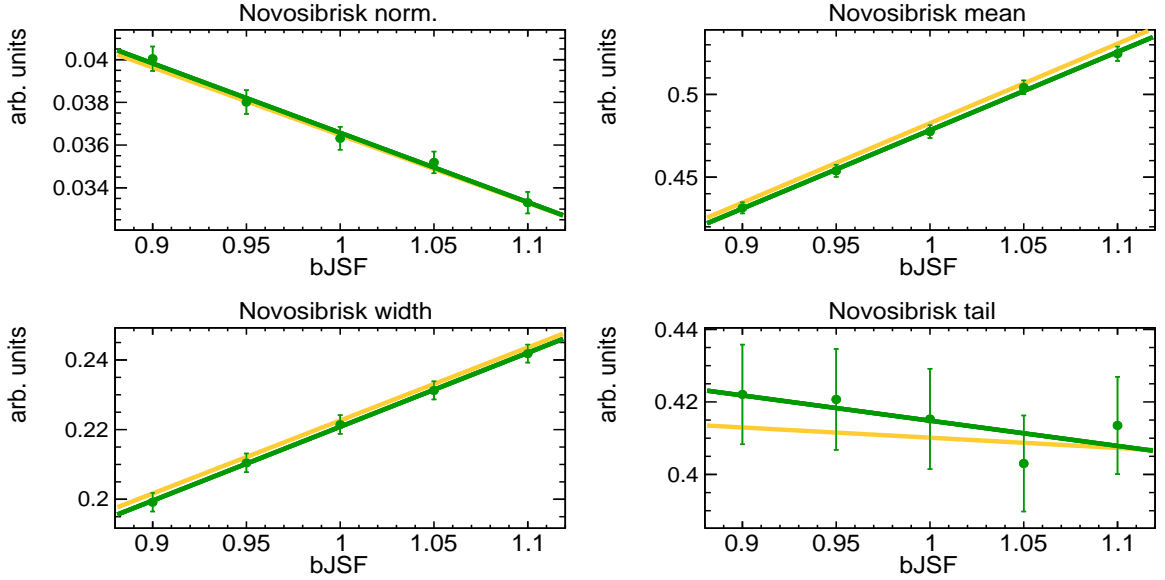
Figure C.4: Dependence of the parameters  $p_i$  on  $m_{top}$  for  $bJSF = 1.10$ . The linear fit of the individual parameters is shown in green. The yellow line represents the result of the combined fit.



## C.2. Plots for varied bJSF and constant $m_{\text{top}}$ values

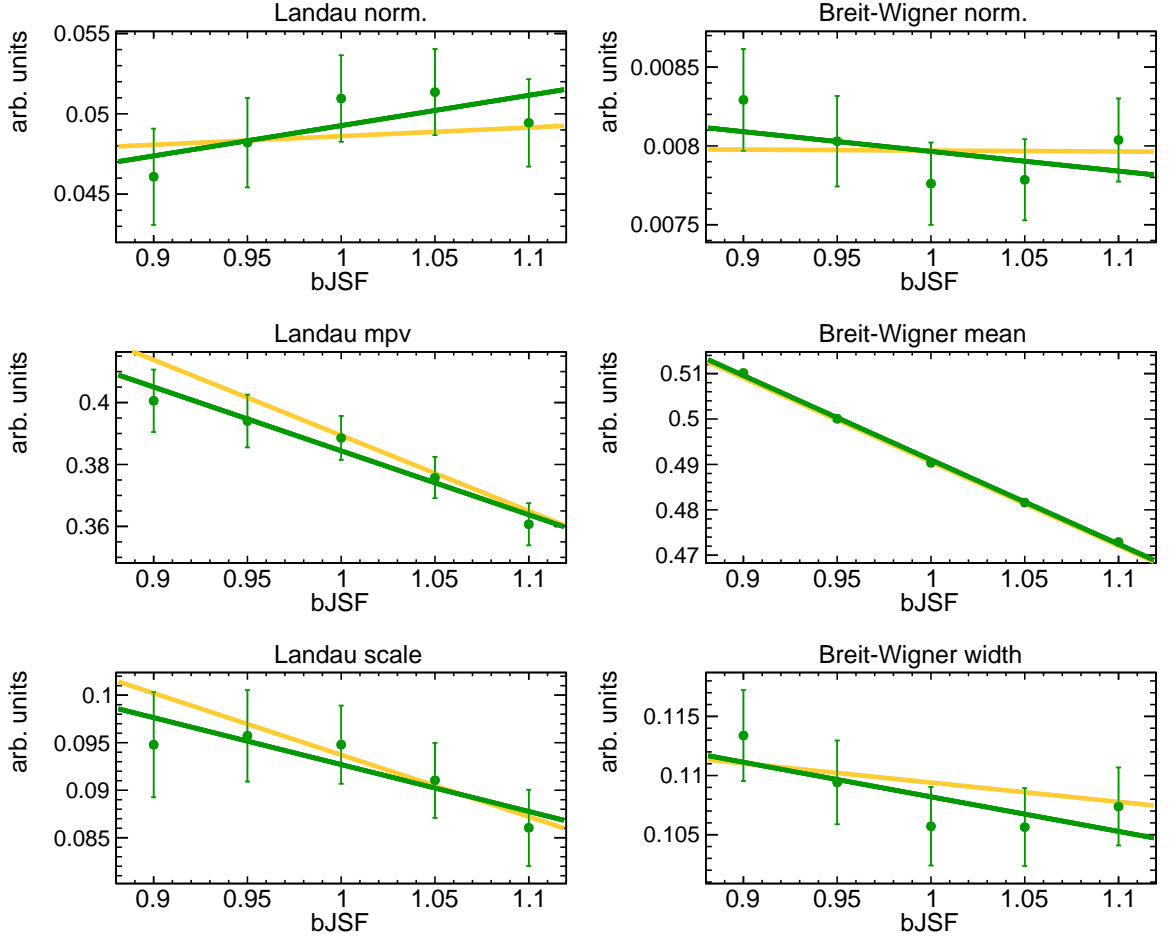


(a) Parameter distributions for  $R_{23}$

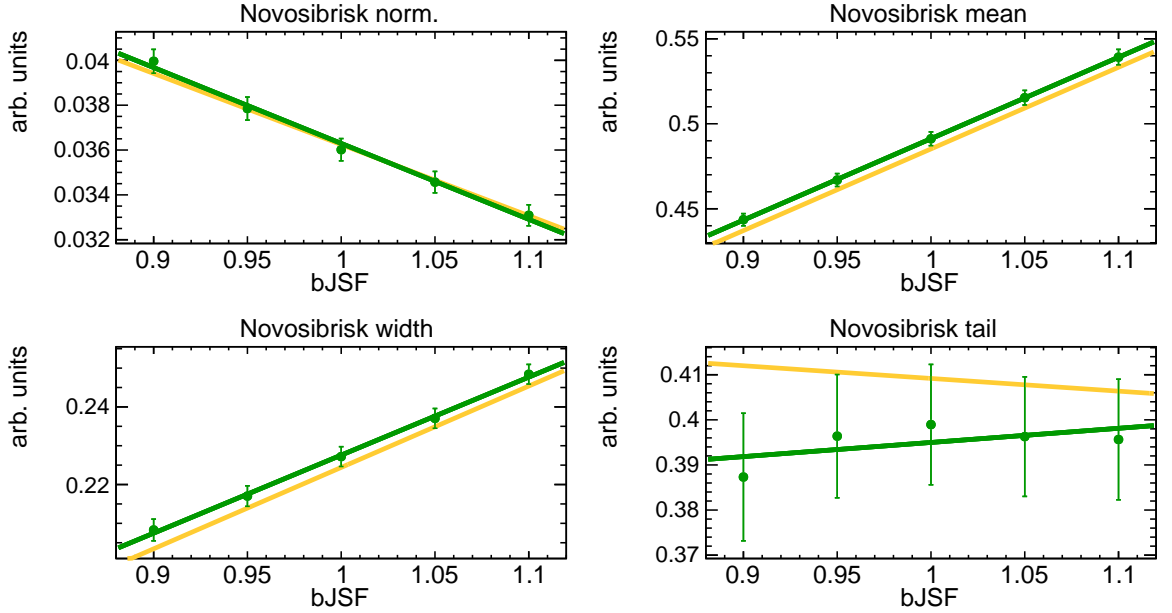


(b) Parameter distributions for  $R_{bl}$

Figure C.5: Dependence of the parameters  $p_i$  on bJSF for  $m_{\text{top}} = 165.0$  GeV. The linear fit of the individual parameters is shown in green. The yellow line represents the result of the combined fit.

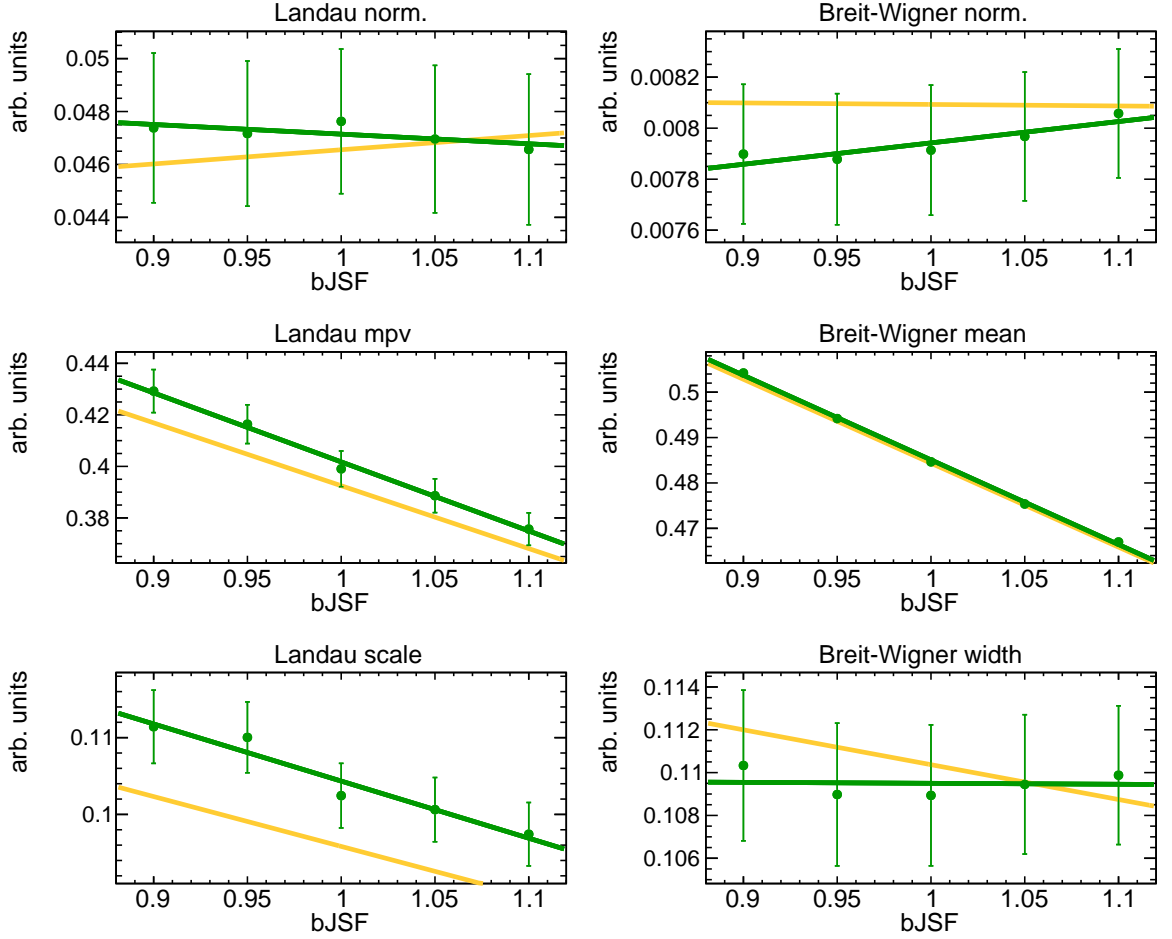


(a) Parameter distributions for  $R_{23}$

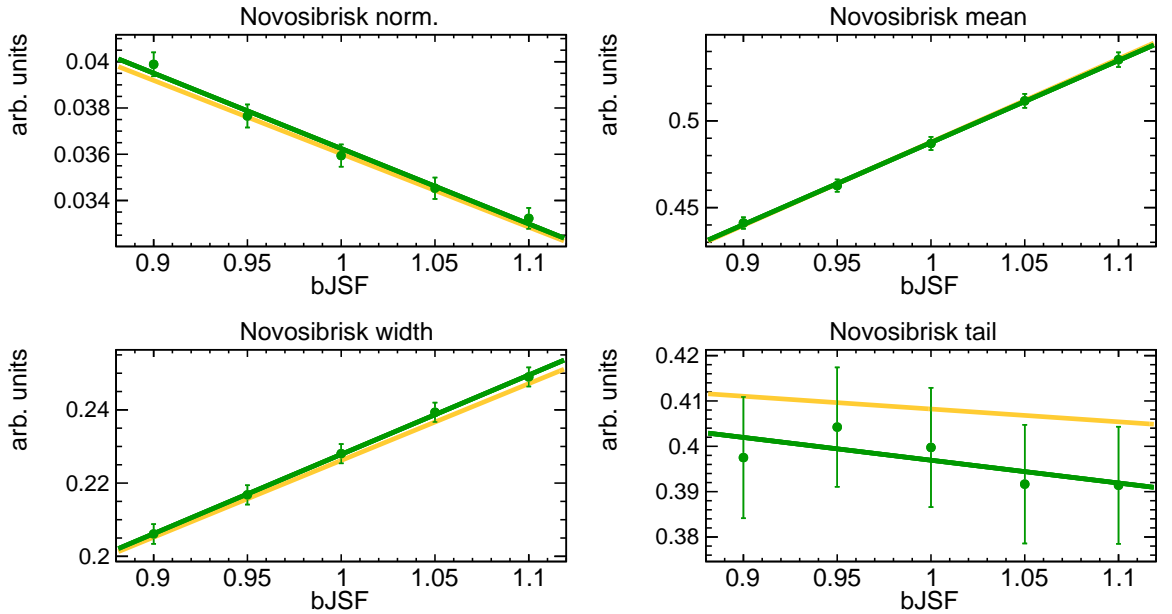


(b) Parameter distributions for  $R_{b1}$

Figure C.6: Dependence of the parameters  $p_i$  on bJSF for  $m_{\text{top}} = 167.5$  GeV. The linear fit of the individual parameters is shown in green. The yellow line represents the result of the combined fit.

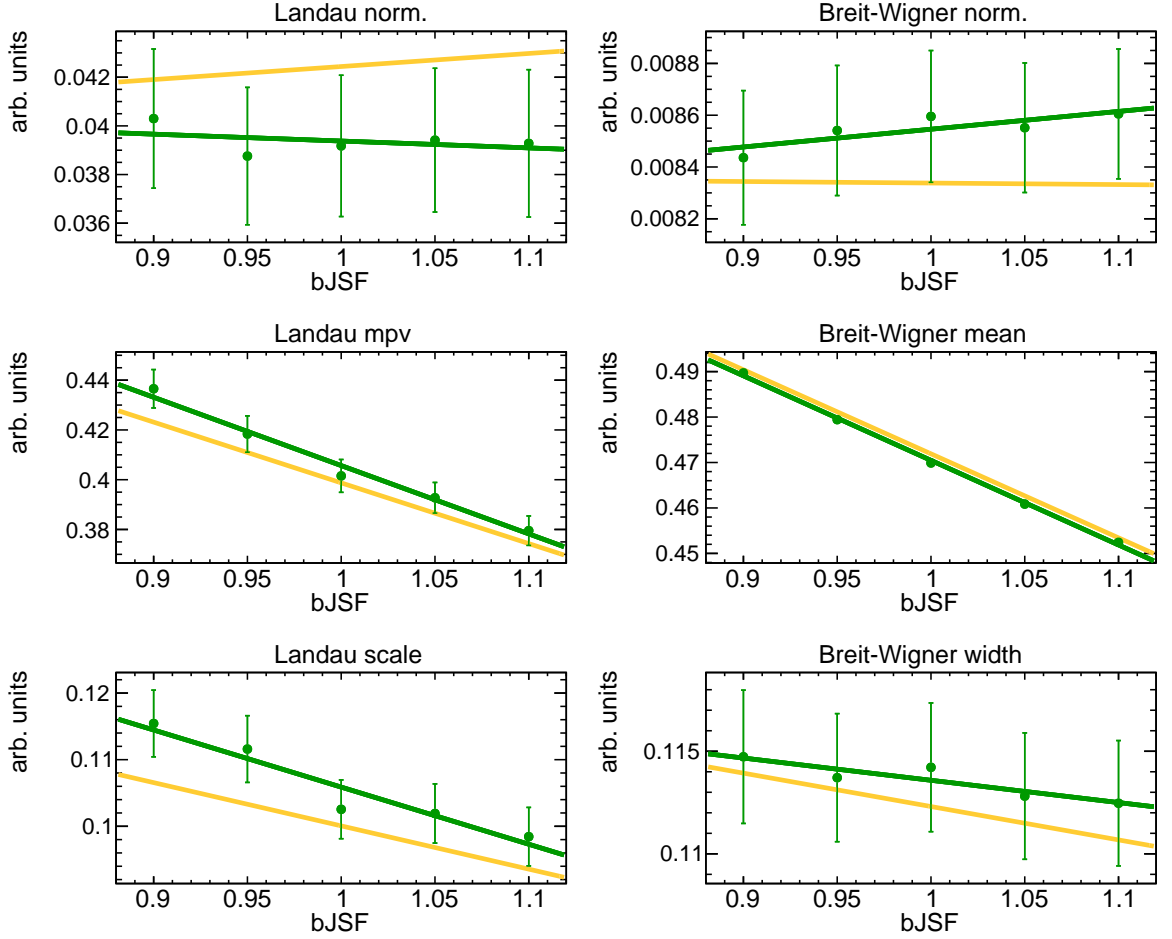


(a) Parameter distributions for  $R_{23}$

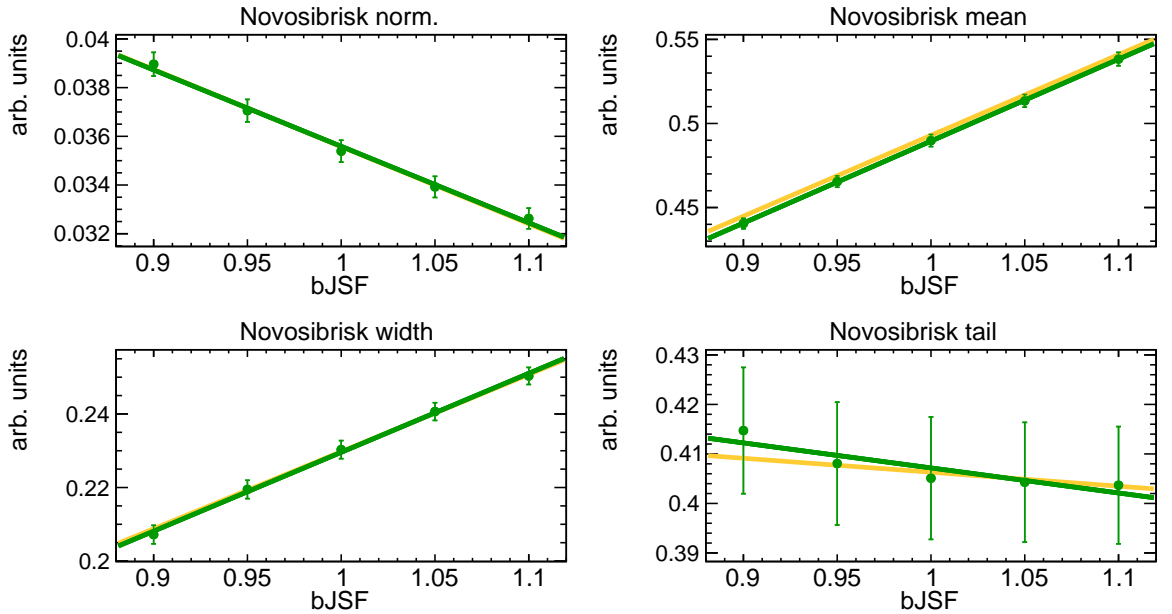


(b) Parameter distributions for  $R_{b1}$

Figure C.7: Dependence of the parameters  $p_i$  on bJSF for  $m_{\text{top}} = 170.0$  GeV. The linear fit of the individual parameters is shown in green. The yellow line represents the result of the combined fit.

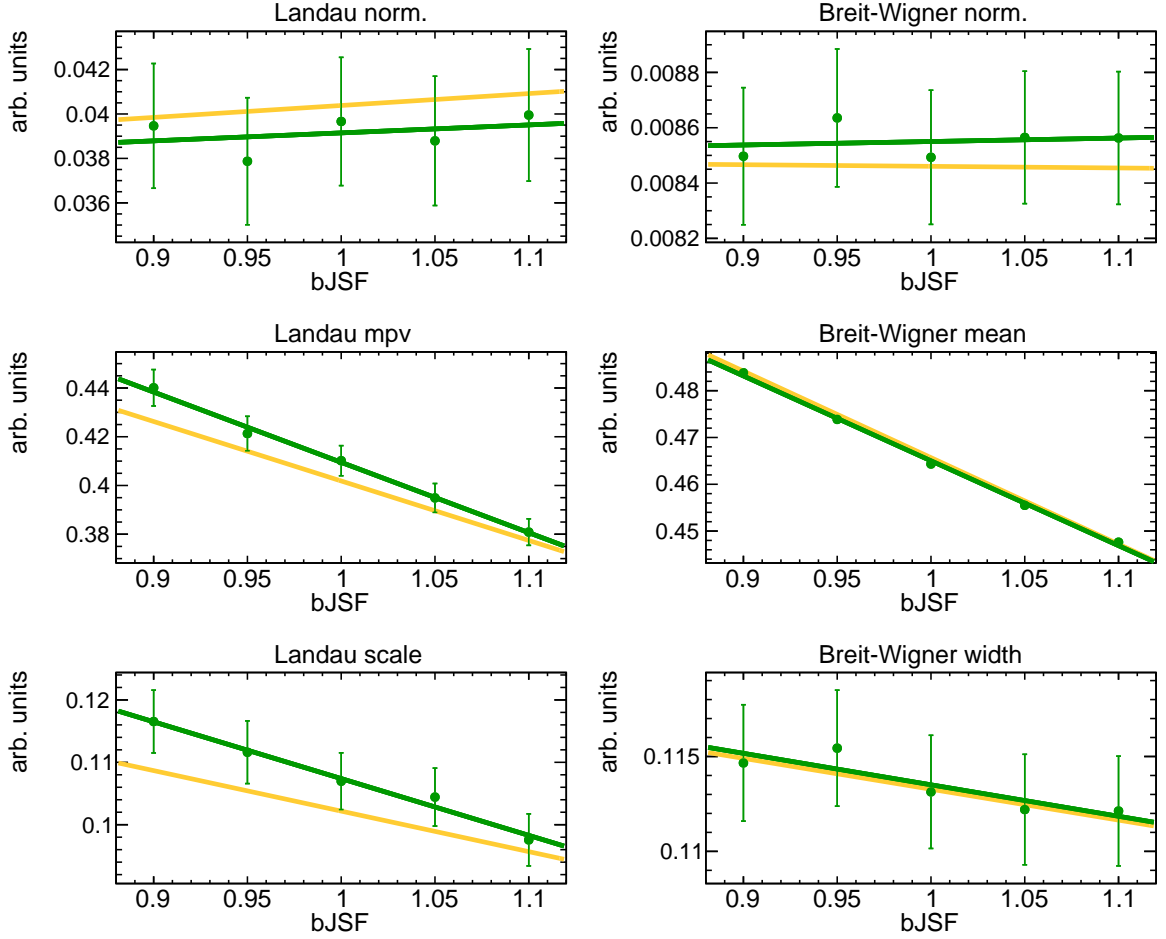


(a) Parameter distributions for  $R_{23}$

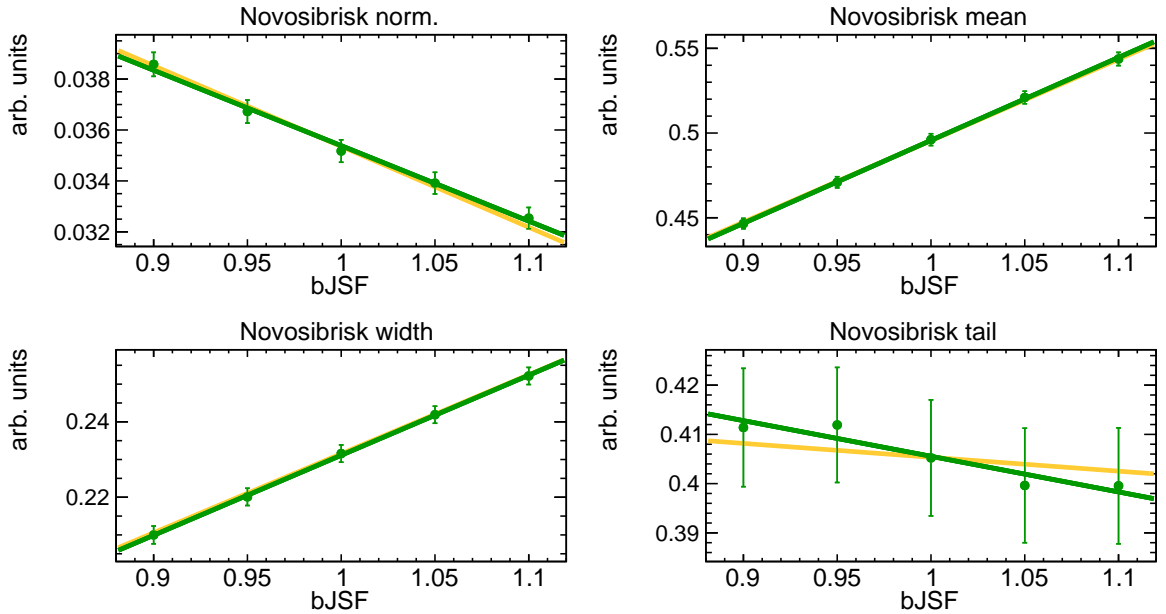


(b) Parameter distributions for  $R_{b1}$

Figure C.8: Dependence of the parameters  $p_i$  on bJSF for  $m_{\text{top}} = 175.0$  GeV. The linear fit of the individual parameters is shown in green. The yellow line represents the result of the combined fit.

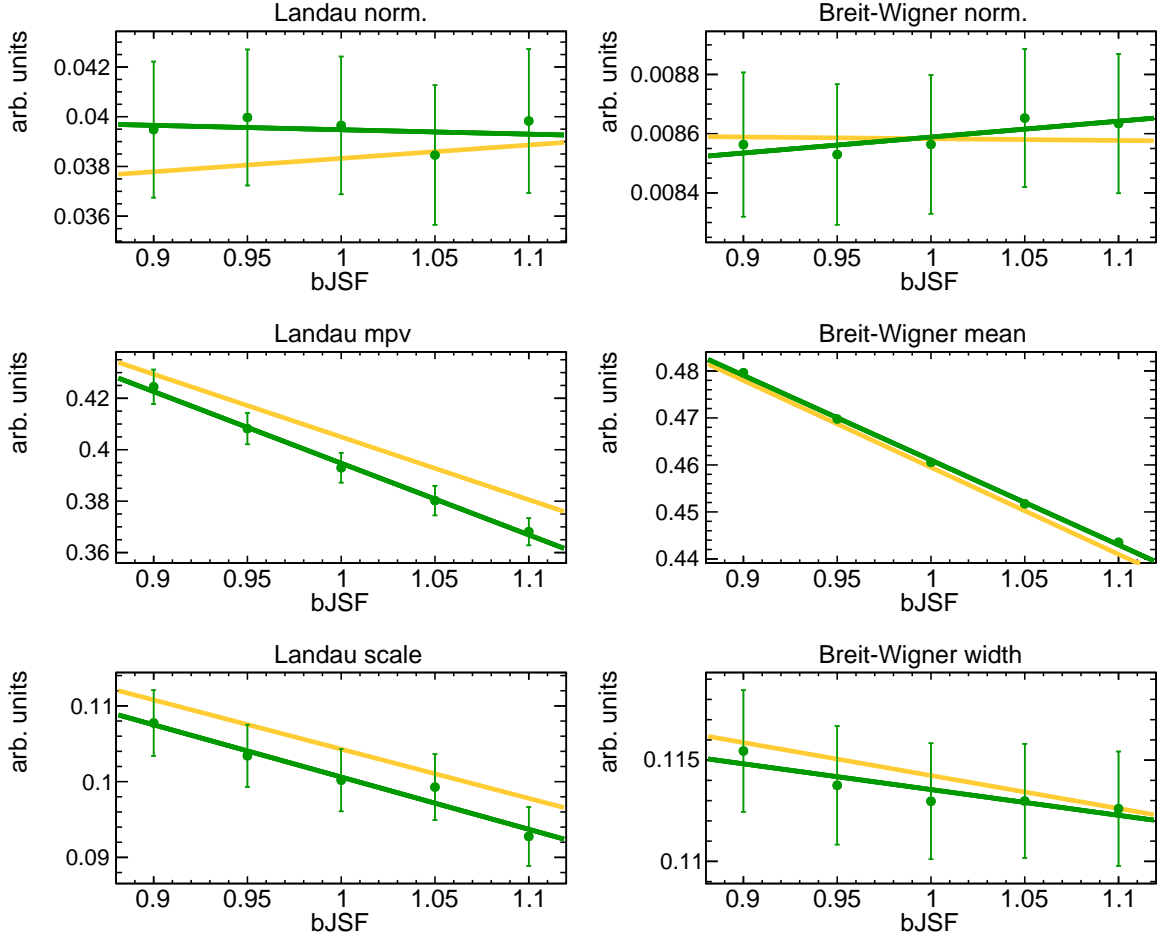


(a) Parameter distributions for  $R_{23}$

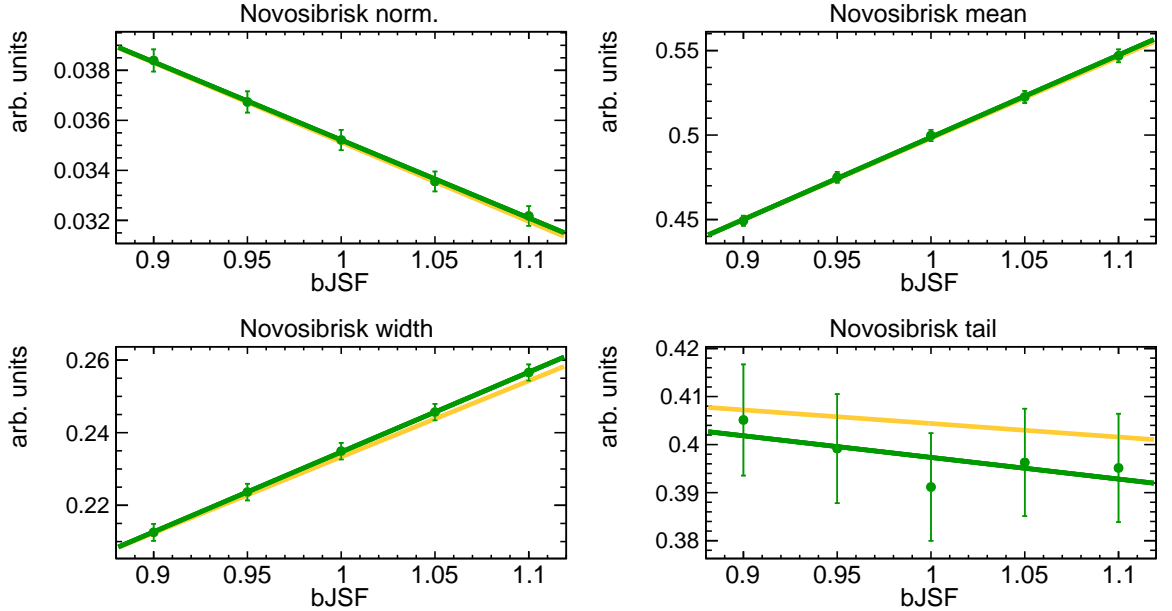


(b) Parameter distributions for  $R_{b1}$

Figure C.9: Dependence of the parameters  $p_i$  on bJSF for  $m_{\text{top}} = 177.5$  GeV. The linear fit of the individual parameters is shown in green. The yellow line represents the result of the combined fit.



(a) Parameter distributions for  $R_{23}$



(b) Parameter distributions for  $R_{b1}$

Figure C.10: Dependence of the parameters  $p_i$  on bJSF for  $m_{\text{top}} = 180.0$  GeV. The linear fit of the individual parameters is shown in green. The yellow line represents the result of the combined fit.

## D. Momenta of light and b-tagged jets

The momenta of the jets in the MC events are shown. The steep flanks at 20 GeV, 30 GeV and 55 GeV are due to the cuts on the momentum of the jets used in the analysis.

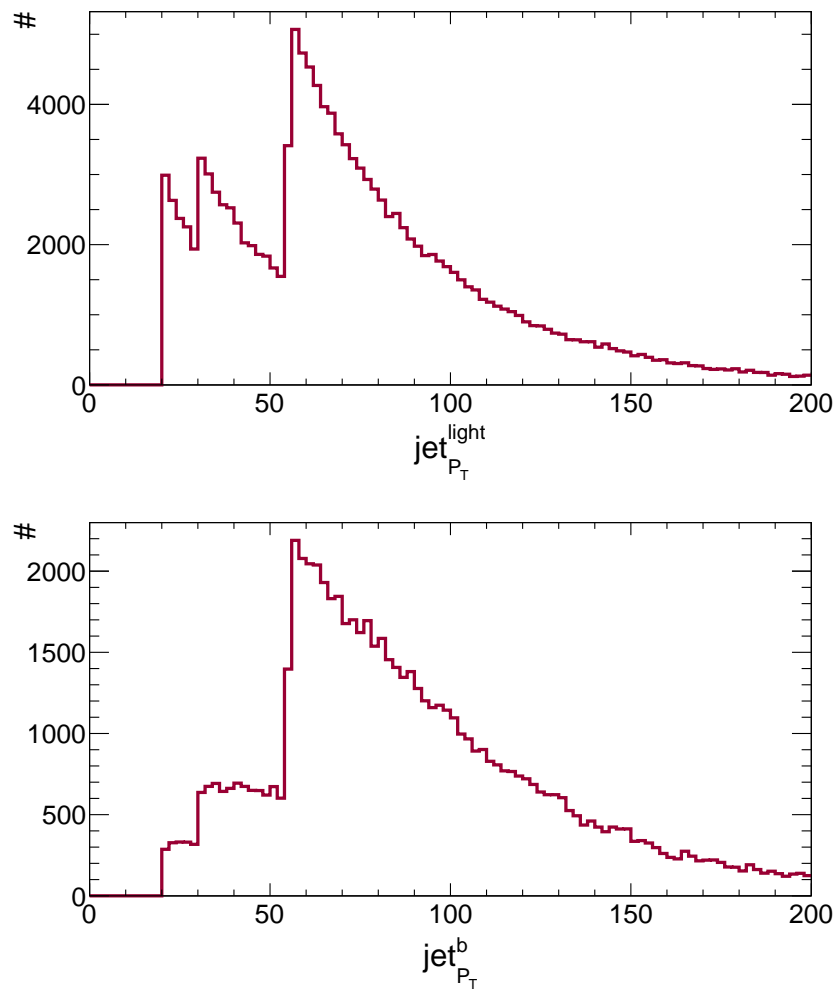


Figure D.1: Momenta of light and b-tagged jets used in the analysis

## Bibliography

- [1] The ATLAS Collaboration. Determination of the top quark mass with a template method in the all hadronic decay channel using 2.04/fb of atlas data. Technical Report ATLAS-CONF-2012-030, CERN, Geneva, Mar 2012.
- [2] The ATLAS collaboration. Observation of a new particle in the search for the standard model higgs boson with the {ATLAS} detector at the {LHC}. *Physics Letters B*, 716(1):1 – 29, 2012.
- [3] Serguei Chatrchyan et al. Observation of a new boson at a mass of 125 GeV with the CMS experiment at the LHC. *Phys.Lett.*, B716:30–61, 2012.
- [4] Perl, M. L. et al. Evidence for anomalous lepton production in  $e^+ - e^-$  annihilation. *Phys. Rev. Lett.*, 35:1489–1492, 1975.
- [5] Fermilab. Discoveries at Fermilab - Discovery of the Bottom Quark. Press release, Fermilab, Aug 1977.
- [6] F. Abe et al. Observation of top quark production in  $\bar{p}p$  collisions. *Phys.Rev.Lett.*, 74:2626–2631, 1995.
- [7] S. Abachi et al. Search for high mass top quark production in  $p\bar{p}$  collisions at  $\sqrt{s} = 1.8$  TeV. *Phys.Rev.Lett.*, 74:2422–2426, 1995.
- [8] J. Beringer et al. (Particle Data Group). Review of particle physics. Technical report, Jul 2012.
- [9] G. Dissertori, I. Knowles, and M. Schmelling. *Quantum Chromodynamics*. Oxford University Press, 1 edition, 2003.
- [10] L. Hoddeson, L. Brown, M. Riordan, and M. Dresden. *The Rise of the Standard Model*. Cambridge University Press, 1 edition, 1997.
- [11] F. Halzen and A. D. Martin. *Quarks and Leptons*. John Wiley and Sons, 1 edition, 1984.
- [12] D. H. Perkins. *Introduction to High Energy Physics*. Cambridge University Press, 4 edition, 2000.
- [13] Griffiths D. *Introduction to Elementary Particles*. Wiley-VCH Verlag GmbH und Co. KGaA, 2 edition, 2008.
- [14] R. E. Marshak. *Conceptual Foundation of Modern Particle Physic*. World Scientific, 1 edition, 1993.
- [15] K. Bethge and U.E. Schroeder. *Elementarteilchen und ihre Wechselwirkungen*. Wiley-VCH Verlag GmbH und Co. KGaA, 3 edition, 2006.



- [16] P. Achard et al. Measurement of the running of the electromagnetic coupling at large momentum-transfer at LEP. *Phys.Lett.*, B623:26–36, 2005.
- [17] H. Georgi. *Weak Interactions and Modern Particle Theory*. The Benjamin/Cummings Publishing Company, Inc., 1 edition, 1984.
- [18] Giuseppe Degrandi, Stefano Di Vita, Joan Elias-Miro, Jose R. Espinosa, Gian F. Giudice, et al. Higgs mass and vacuum stability in the Standard Model at NNLO. *JHEP*, 1208:098, 2012.
- [19] Ling-Lie Chau. Quark Mixing in Weak Interactions. *Phys.Rept.*, 95:1–94, 1983.
- [20] Nikolaos Kidonakis. Next-to-next-to-leading-order collinear and soft gluon corrections for t-channel single top quark production. *Phys.Rev.*, D83:091503, 2011.
- [21] Nikolaos Kidonakis. NNLL resummation for s-channel single top quark production. *Phys.Rev.*, D81:054028, 2010.
- [22] Nikolaos Kidonakis. Two-loop soft anomalous dimensions for single top quark associated production with a W- or H-. *Phys.Rev.*, D82:054018, 2010.
- [23] J. K. Behr. Measurement of the top-quark mass in the semileptonic decay channel at the atlas experiment. Master’s thesis, Ludwig-Maximilians-Universität München, 2012.
- [24] Matteo Cacciari, Michal Czakon, Michelangelo Mangano, Alexander Mitov, and Paolo Nason. Top-pair production at hadron colliders with next-to-next-to-leading logarithmic soft-gluon resummation. *Phys.Lett.*, B710:612–622, 2012.
- [25] Peter Baernreuther, Michal Czakon, and Alexander Mitov. Percent Level Precision Physics at the Tevatron: First Genuine NNLO QCD Corrections to  $q\bar{q} \rightarrow t\bar{t} + X$ . *Phys.Rev.Lett.*, 109:132001, 2012.
- [26] Michal Czakon, Paul Fiedler, and Alexander Mitov. The total top quark pair production cross-section at hadron colliders through  $O(\alpha_S^4)$ . 2013.
- [27] Michal Czakon and Alexander Mitov. NNLO corrections to top pair production at hadron colliders: the quark-gluon reaction. *JHEP*, 1301:080, 2013.
- [28] Michal Czakon and Alexander Mitov. NNLO corrections to top-pair production at hadron colliders: the all-fermionic scattering channels. *JHEP*, 1212:054, 2012.
- [29] Michal Czakon and Alexander Mitov. Top++: A Program for the Calculation of the Top-Pair Cross-Section at Hadron Colliders. 2011.
- [30] Michiel Botje, Jon Butterworth, Amanda Cooper-Sarkar, Albert de Roeck, Joel Feltesse, et al. The PDF4LHC Working Group Interim Recommendations. 2011.
- [31] A.D. Martin, W.J. Stirling, R.S. Thorne, and G. Watt. Parton distributions for the LHC. *Eur.Phys.J.*, C63:189–285, 2009.
- [32] A.D. Martin, W.J. Stirling, R.S. Thorne, and G. Watt. Uncertainties on  $\alpha(S)$  in global PDF analyses and implications for predicted hadronic cross sections. *Eur.Phys.J.*, C64:653–680, 2009.

- 
- [33] Hung-Liang Lai, Marco Guzzi, Joey Huston, Zhao Li, Pavel M. Nadolsky, et al. New parton distributions for collider physics. *Phys.Rev.*, D82:074024, 2010.
- [34] Jun Gao, Marco Guzzi, Joey Huston, Hung-Liang Lai, Zhao Li, et al. The CT10 NNLO Global Analysis of QCD. 2013.
- [35] Richard D. Ball, Valerio Bertone, Stefano Carrazza, Christopher S. Deans, Luigi Del Debbio, et al. Parton distributions with LHC data. *Nucl.Phys.*, B867:244–289, 2013.
- [36] Christiane Lefèvre. The cern accelerator complex. complexe des accélérateurs du cern. Dec 2008.
- [37] M Ferro-Luzzi. Review of 2011 lhc run from the experiments perspective. In *Chamonix 2012 Workshop on LHC Performance*, page 16 p, Geneva, 2012. CERN, CERN.
- [38] Lyndon Evans and Philip Bryant. Lhc machine. *Journal of Instrumentation*, 3(08):S08001, 2008.
- [39] The ATLAS Collaboration. The atlas experiment at the cern large hadron collider. *Journal of Instrumentation*, 3(08):S08003, 2008.
- [40] Joao Pequeno. Computer generated image of the whole atlas detector. Mar 2008.
- [41] The ATLAS Collaboration. *ATLAS magnet system: Technical Design Report, 1*. Technical Design Report ATLAS. CERN, Geneva, 1997.
- [42] The ATLAS Collaboration. Readiness of the atlas liquid argon calorimeter for lhc collisions. *The European Physical Journal C*, 70(3):723–753, 2010.
- [43] D.M. Gingrich, G. Lachat, J. Pinfold, J. Soukoup, D. Axen, et al. Construction, assembly and testing of the ATLAS hadronic end-cap calorimeter. *JINST*, 2:P05005, 2007.
- [44] The ATLAS Collaboration. *ATLAS calorimeter performance Technical Design Report*. 1996.
- [45] Daniel Fournier. Performance of the LHC, ATLAS and CMS in 2011. *EPJ Web Conf.*, 28:01003, 2012.
- [46] The ATLAS Collaboration. ATLAS Overview and Main Results. 2013.
- [47] A.D. Martin, W.J. Stirling, R.S. Thorne, and G. Watt. Parton distributions for the LHC key plots. 2009.
- [48] The ATLAS Collaboration. Measurement of the top quark mass from  $\sqrt{s} = 7$  tev atlas data using a 3-dimensional template fit. Technical Report ATLAS-CONF-2013-046, CERN, Geneva, May 2013.
- [49] Paolo Nason. A New method for combining NLO QCD with shower Monte Carlo algorithms. *JHEP*, 0411:040, 2004.
- [50] Stefano Frixione, Paolo Nason, and Carlo Oleari. Matching NLO QCD computations with Parton Shower simulations: the POWHEG method. *JHEP*, 0711:070, 2007.
- [51] Simone Alioli, Paolo Nason, Carlo Oleari, and Emanuele Re. A general framework for implementing NLO calculations in shower Monte Carlo programs: the POWHEG BOX. *JHEP*, 1006:043, 2010.

- [52] Torbjorn Sjostrand, Stephen Mrenna, and Peter Z. Skands. PYTHIA 6.4 Physics and Manual. *JHEP*, 0605:026, 2006.
- [53] Peter Zeiler Skands. Tuning Monte Carlo Generators: The Perugia Tunes. *Phys.Rev.*, D82:074018, 2010.
- [54] Paolo Nason and Bryan Webber. Next-to-Leading-Order Event Generators. *Ann.Rev.Nucl.Part.Sci.*, 62:187–213, 2012.
- [55] M.A. Dobbs, S. Frixione, Eric Laenen, K. Tollefson, H. Baer, et al. Les Houches guidebook to Monte Carlo generators for hadron collider physics. pages 411–459, 2004.
- [56] S. Agostinelli et al. Geant4—a simulation toolkit. *Nuclear Instruments and Methods in Physics Research Section A: Accelerators, Spectrometers, Detectors and Associated Equipment*, 506(3):250 – 303, 2003.
- [57] The ATLAS Collaboration. The atlas simulation infrastructure. *Eur. Phys. J. C*, 70(arXiv:1005.4568. CERN-PH-EP-2010-044):823–874. 53 p, 2010.
- [58] The ATLAS Collaboration. Twiki: Topcommonobjects2011. <https://twiki.cern.ch/twiki/bin/viewauth/AtlasProtected/TopCommonObjects2011>.
- [59] Georges Aad et al. Electron performance measurements with the ATLAS detector using the 2010 LHC proton-proton collision data. *Eur.Phys.J.*, C72:1909, 2012.
- [60] Expected electron performance in the atlas experiment. Technical Report ATL-PHYS-PUB-2011-006, CERN, Geneva, Apr 2011.
- [61] B Resende. Muon identification algorithms in atlas. Technical Report ATL-PHYS-PROC-2009-113, CERN, Geneva, Sep 2009.
- [62] W Lampl, S Laplace, D Lelas, P Loch, H Ma, S Menke, S Rajagopalan, D Rousseau, S Snyder, and G Unal. Calorimeter clustering algorithms: Description and performance. Technical Report ATL-LARG-PUB-2008-002. ATL-COM-LARG-2008-003, CERN, Geneva, Apr 2008.
- [63] Matteo Cacciari, Gavin P. Salam, and Gregory Soyez. The Anti-k(t) jet clustering algorithm. *JHEP*, 0804:063, 2008.
- [64] Matteo Cacciari, Gavin P. Salam, and Gregory Soyez. FastJet User Manual. *Eur.Phys.J.*, C72:1896, 2012.
- [65] D W Miller, A Schwartzman, and D Su. Jet-vertex association algorithm. Technical Report ATL-COM-PHYS-2008-008, CERN, Geneva, Jan 2008.
- [66] Commissioning of the atlas high-performance b-tagging algorithms in the 7 tev collision data. Technical Report ATLAS-CONF-2011-102, CERN, Geneva, Jul 2011.
- [67] Jet energy scale and its systematic uncertainty in proton-proton collisions at  $\sqrt{s}=7$  tev with atlas 2011 data. Technical Report ATLAS-CONF-2013-004, CERN, Geneva, Jan 2013.
- [68] Georges Aad et al. Jet energy measurement with the ATLAS detector in proton-proton collisions at  $\sqrt{s} = 7$  TeV. *Eur.Phys.J.*, C73:2304, 2013.

- [69] V Boisvert and the Atlas Collaboration. Top quarks objects definition and performance at atlas. *Journal of Physics: Conference Series*, 452(1):012012, 2013.
- [70] J Erdmann, K Kroeninger, O Nackenhorst, and A Quadt. Kinematic fitting of ttbar-events using a likelihood approach: The klfit package. Technical Report ATL-COM-PHYS-2009-551, CERN, Geneva, Sep 2009.
- [71] R Barlow. Application of the bootstrap resampling technique to particle physics experiments. Technical Report MAN/HEP/99/4, Manchester Part. Phys., Apr 2000.
- [72] Brun R. and Rademakers, F. ROOT - An Object Oriented Data Analysis Framework. In *AIHENP'96 Workshop*, pages 81–86, 1996.
- [73] A Bevan and Wilson F. AFit User Guide. Technical report, Dec 2010.

## List of Figures

2.1.	Electron electron scattering via the exchange of a virtual photon . . . . .	6
2.2.	Additional vertices, due to the self coupling of gluons . . . . .	7
2.3.	The running coupling constants $\alpha_s$ . . . . .	7
2.4.	The one-dimensional Higgs potential . . . . .	9
2.5.	Production mechanism of top-quarks via the electroweak interaction . . . . .	12
2.6.	Feynman graphs of the leading order $t\bar{t}$ -pair production mechanisms . . . . .	13
2.7.	Feynman graphs of the next-to-leading order $t\bar{t}$ -pair production . . . . .	13
2.8.	The dileptonic $t\bar{t}$ -decay . . . . .	15
2.9.	The semileptonic $t\bar{t}$ -decay . . . . .	15
2.10.	The all-hadronic $t\bar{t}$ -decay . . . . .	16
2.11.	Decay channels of a $t\bar{t}$ -system . . . . .	16
3.1.	The CERN accelerator complex . . . . .	17
3.2.	The ATLAS detector . . . . .	19
3.3.	The ATLAS magnet system . . . . .	20
3.4.	The ATLAS inner detector . . . . .	20
3.5.	The ATLAS calorimeter system . . . . .	21
3.6.	The ATLAS muon system <sup>[40]</sup> . . . . .	23
3.7.	The MSTW2008NNLO parton density function . . . . .	25
4.1.	The Lund string model shown for a $q\bar{q}$ -system . . . . .	27
4.2.	Identification of particles in the the ATLAS detector <sup>[40]</sup> . . . . .	29
4.3.	Behaviour of a not infrared and collinear safe jet reconstruction algorithm . . . . .	31
4.4.	The average jet energy response for 2011 data taking as function of the jet $\eta$ . . . . .	33
4.5.	Relative errors on the jet energy scale for the 2011 data taking period . . . . .	33
4.6.	Example of QCD multijet production . . . . .	35
4.7.	Number of remaining events for the different selection criteria . . . . .	36
4.8.	The $\ln L$ values of the best permutations obtained from the MC signal sample . . . . .	38
4.9.	Distribution of $m_{jjj}$ for different input top-quark masses . . . . .	38
4.10.	Influence of the jet scale factors lJSF and bJSF on $m_{jj}$ . . . . .	39
4.11.	Influence of the jet scale factors lJSF and bJSF on $m_{jjj}$ . . . . .	40
4.12.	Distribution of $R_{23}$ for different input top-quark masses . . . . .	41
4.13.	Influence of the jet scale factors lJSF and bJSF on $R_{23}$ . . . . .	42
4.14.	Dependence of $R_{bl}$ on bJSF for a fixed lJSF . . . . .	42
4.15.	Influence of the lJSF and $m_{top}$ on $R_{bl}$ . . . . .	43
4.16.	Parametrisation of $R_{23}$ and $R_{bl}$ . . . . .	44
4.17.	Estimator distributions for a binned likelihood fit of the signal MC . . . . .	47
4.18.	Result of the binned likelihood fit, for different input values of bJSF . . . . .	47
4.19.	Distributions of $R_{23}$ for all seven mass variation samples and five values of bJSF . . . . .	48
4.20.	Distributions of $R_{bl}$ for all seven mass variation samples and five values of bJSF . . . . .	49
4.21.	Dependence of the parameters $p_i$ on $m_{top}$ for bJSF = 1 . . . . .	50

4.22. Dependence of the parameters $p_i$ on bJSF for $m_{\text{top}} = 172.5$ GeV . . . . .	51
4.23. Result of 5000 pseudo-experiments . . . . .	52
A.1. Distribution of $R_{32}$ for input top-quark mass . . . . .	54
A.2. Influence of the jet scale factors lJSF and bJSF on $R_{32}$ . . . . .	54
A.3. lJSF dependence for bJSF = 1.0 . . . . .	55
A.4. Result of 5000 pseudo-experiments . . . . .	55
A.5. Distributions of $R_{32}$ for all seven mass variation samples and five values of bJSF	56
A.6. Dependence of the $R_{32}$ parameters on $m_{\text{top}}$ and bJSF . . . . .	57
B.1. Impact of parameter variations on the Landau function . . . . .	58
B.2. Impact of parameter variations on the Breit-Wigner function . . . . .	58
B.3. Impact of parameter variations on the Novosibirsk function . . . . .	59
B.4. Impact of parameter variations on the Gauss function . . . . .	60
C.1. Dependence of the parameters $p_i$ on $m_{\text{top}}$ for bJSF = 0.90 . . . . .	63
C.2. Dependence of the parameters $p_i$ on $m_{\text{top}}$ for bJSF = 0.95 . . . . .	64
C.3. Dependence of the parameters $p_i$ on $m_{\text{top}}$ for bJSF = 1.05 . . . . .	65
C.4. Dependence of the parameters $p_i$ on $m_{\text{top}}$ for bJSF = 1.10 . . . . .	66
C.5. Dependence of the parameters $p_i$ on bJSF for $m_{\text{top}} = 165.0$ GeV . . . . .	67
C.6. Dependence of the parameters $p_i$ on bJSF for $m_{\text{top}} = 167.5$ GeV . . . . .	68
C.7. Dependence of the parameters $p_i$ on bJSF for $m_{\text{top}} = 170.0$ GeV . . . . .	69
C.8. Dependence of the parameters $p_i$ on bJSF for $m_{\text{top}} = 175.0$ GeV . . . . .	70
C.9. Dependence of the parameters $p_i$ on bJSF for $m_{\text{top}} = 177.5$ GeV . . . . .	71
C.10. Dependence of the parameters $p_i$ on bJSF for $m_{\text{top}} = 180.0$ GeV . . . . .	72
D.1. Momenta of light and b-tagged jets used in the analysis . . . . .	73

# Danksagung:

Ich möchte mich bei allen bedanken, die mich auf meinem bisherigen Weg begleitet haben. Im Rahmen des Physik-Studiums gebührt mein besonderer Dank:

- Meiner Familie, die mich immer vorbehaltlos unterstützt hat
- Meinen Betreuern, Dr. Stefanie Adomeit und Prof. Dr. Otmar Biebel, die sich immer die Zeit für meine Fragen und Probleme genommen haben
- Prof. Dr. Dorothee Schaile, für die Möglichkeit diese Arbeit an Ihrem Lehrstuhl zu verfassen
- Den Kolleginnen und Kollegen des Lehrstuhl Schaile, insbesondere Friedrich Hönig, Florian Rättich und Sebastian Lehrack
- Emanuel Wittmann, ohne den ich wahrscheinlich niemals so weit gekommen wäre
- Meinen Mitbewohnern Fiona 'PowPow' Häger und Philipp Herian
- Meinen Freunden, stellvertretend Arndt Fallenstein und Jan Pieper, da sie sich durch diese Arbeit gequält haben
- Der Siemens AG für die Möglichkeit mein Studium zu finanzieren, besonders den Mitarbeitern und Mitarbeiterinnen der Corporate Technology Intellectual Property Support Administration Munich für die schöne Zeit

## **Erklärung:**

Hiermit erkläre ich, die vorliegende Arbeit selbständig verfasst zu haben und keine anderen als die in der Arbeit angegebenen Quellen und Hilfsmittel benutzt zu haben.

München, 30. August 2013

Unterschrift